8-2019

Polarization Properties of Airy and Ince-Gaussian Laser Beams

Sean Michael Nomoto
University of Arkansas, Fayetteville

Polarization Properties of Airy and Ince-Gauss Laser Beams

A dissertation submitted in partial fulfillment
of the requirements for the degree of
Doctor of Philosophy in Physics

by

Sean Michael Nomoto
University of Wisconsin - River Falls
Bachelor of Science in Physics 2011
University of Arkansas
Master of Science in Physics, 2016

August 2019
University of Arkansas

This dissertation is approved for recommendation to the Graduate Council.

Surendra Singh, Ph.D.
Dissertation Director

Reeta Vyas, Ph.D.
Committee Member

Salvador Barraza-Lopez, Ph.D.
Committee Member

Huaxiang Fu, Ph.D.
Committee Member

Mark Arnold, Ph.D.
Committee Member

Abstract

The description of polarization states of laser light as linear, circular polarization within the paraxial scalar wave approximation is adequate for most applications. However, this description falls short when considering laser light as an electromagnetic wave satisfying Maxwell's equations. An electric field with a constant unit vector for direction of the field and a space dependent complex scalar amplitude in the paraxial wave approximation does not satisfy Maxwell equations which, in general, requires all three Cartesian components of electric and magnetic fields associated for a nonzero laser beam to be nonzero.

Physical observation of passing a linearly polarized laser through a pair of polarizers with their transmission axes perpendicular to one another (crossed polarizers) shows that the beam cannot be completely extinguished. Some intensity is always transmitted through the polarizers. In this case, the transmitted intensity exhibits a unique spatial pattern corresponding to a polarization component that is orthogonal (cross component) to the original polarization (dominant component) of the beam incident. These unique spatial patterns of the cross component have been studied for Hermite and Laguerre Gaussian beams (HG and LG beams). In this work, the investigation is extended to Ince Gauss (IG) and Airy beams. Both types of beams were produced by shining a collimated fundamental Gaussian beam onto a spatial light modulator (SLM). IG beams are more general solutions of the paraxial wave equation, which reduce to HG or LG type of solutions in two opposite limits. Using this method, IG beams up to order $p = 5$ with ellipticity variation from 0.01 to 2.0 and Airy beams truncated to have finite transverse extent were produced. These beams were produced to have a dominant linear polarization.

Each beam produced was then passed through a pair of crossed linear polarizers. The irradiance of the resulting cross component after the polarizers was recorded via a CCD. In all cases, the observed cross components follow a general trend such that the positions of inflection in the dominant component become maxima in the cross components and the extrema positions become minima (positions with no irradiance) in the cross component.

Acknowledgements

Special thanks to Dr. Surendra Singh for the unprecedented amount of patience, care, and effort in supporting me for all these years. And, to Dr. Reeta Vyas for her great patience as well as helpful discussion in research and life. Also, to committee members Dr. Huaxiang Fu, Dr. Salvador Barraza-Lopez, and Dr. Mark Arnold including Drs. Singh and Vyas. I would also like to thank the Physics Department for supporting me through education, research, and unique opportunities. Thanks also to my mother, sister, and family for their continued support. Thanks to Anindya Ambuj, Nik Martinneau, Patrick Kells, Luis Felipe, Chris Horns, and special thanks to Silvia Palacios Crocker. There are many more people to thank, but it would be difficult to list them all without forgetting anyone. So, thank you to all who have supported me in any way whether it was academic or personal. This PhD program has been one of the most challenging endeavors in my life. Something I learned the hard way was that although the education continues, so does life with its many complications and joys. Without these people, this would not have been possible. Thank you.

Dedication

This is dedicated to those who have a passion for math and science, my family and friends, and Silvia Palacios Crocker.

Contents

List of Publications

1. Sean Nomoto, A. Aadhi, Shashi Prabhakar, R. P. Singh, Reeta Vyas, and Surendra Singh. Polarization properties of the Airy beam. Opt. Lett., 40(19):4516-4519, Oct 2015.

2. Sean Nomoto, Adam Goldstein, Reeta Vyas, and Surendra Singh. Polarization properties of Ince-Gaussian laser beams. J. Opt. Soc. Am. A, 34(12):2261-2265, Dec 2017.

3. Anindya Ambuj, Emily Walla, Sophia Andaloro, Sean Nomoto, Reeta Vyas, and Surendra Singh. Symmetry in the Diffraction of beams carrying orbital angular momentum. Phys. Rev. A 99, 013846, Jan 2019.

4. Hyrum Richardson, Charlotte Welch, Sean Nomoto, Reeta Vyas, Surendra Singh, A new method for detecting the nonlinearity of the Pancharatnam phase of light, Optics Commun. 451, 62-66 Nov 2019.

Chapter 1

Introduction

A system that would work as a laser was first proposed by Charles H. Townes, Arthur L. Schawlow in 1958 [1], but it wasn't until 1960 that a light-emitting Ruby laser was demonstrated by Theodore H. Maiman [2]. The laser action is based on the concept of stimulated emission of radiation introduced by Einstein in 1917 [3]. Since the first operation of the Ruby laser, laser action has been achieved in numerous systems to the point that lasers are now a part of household devices. Applications and manipulation of laser light for newer devices will continue to be an active field of research for many years to come.

The laser is an important physical system that is commonly used in many devices vital to technology and its advances. Applications of lasers range from large interferometers used in the Laser Interferometer Gravitational-wave Observatory (LIGO) (in Livingston, LA and Hanford, WA) and soon the Laser Interferometer Space Antenna (LISA) for detecting gravitational waves, to laser particle accelerators on the nanometer scale [4, 5].

Lasers are also used in more conventional applications such as airplane gyroscopes, computers, and any practical situations in which minute to very large distances must be measured and compared. They are vital for applications and technologies of telecommunications via internet and satellite. Thus, the laser has become one of the most important and practical scientific tools of our time. The types of available laser systems have expanded from plasma to gas to liquid to solid, thus spanning all conventional phases of matter.

Besides fabrication and operation of lasers, an area of important research concerns modeling and describing laser beams; specifically, polarization of laser beams. In majority of applications, it is the wave aspect of the laser exemplified by interference or diffraction of waves that is involved. A very important aspect of wave interaction is its dependence on the property of wave polarization.

It is known that polarization of light is defined by the direction of oscillation of the electric field. Equally valid descriptions of polarization are in terms of the magnetic field and its oscillation. However, since the orientations of the electric and magnetic field are coupled via Maxwell's equations. It is sufficient to specify either the directions of the electric field or the magnetic field. We will describe polarization in terms of the electric field.

Furthermore, since optical interactions are dominated by electric dipole interactions [6], it is the electric field that is principally used in describing electromagnetic radiation and its interaction with matter.

Most day-to-day applications involve descriptions of the laser light as a linearly polarized or circularly polarized plane wave. Its transverse spatial structure in terms of finite size Gaussian, expanding or converging beam is usually not considered.

In this approximation, laser beams are modeled in terms of a scalar function that depends on transverse field coordinates multiplied by a constant vector to describe the laser beam polarization. As mentioned in the abstract, this model comes with some contradiction to what is observed experimentally as well as the Maxwell's equations. The finiteness of the beam is certainly accurately captured by this description, but the polarization being constant cannot be satisfied due to that finiteness. Maxwell's equations

do not allow a finite size laser beam to have a homogeneous polarization profile. This finite size forces an inhomogeneous polarization profile and will be shown to follow from Maxwell's equations.

The contradiction between the scalar model's homogeneous polarization and what is observed is easily revealed by passing a linearly polarized beam through a pair of orthogonally orientated linear polarizers which fail to extinguish the beam. Instead some light leaks through that has a specific spatial profile. This observation requires a more satisfying description for the laser beam polarization.

An approach that is discussed in this work, reverts to a description of laser light using Maxwell's equations and utilizes an approximation method that expands electric and magnetic field components in powers of the ratio of wavelength to the transverse size of the beam. An approximation involving this infinite expansion reconciles the laser beam description with Maxwell's equations. Such a laser beam model may be called Maxwell-Gauss laser beams.

Such beams are predicted to have a longitudinal polarization along the direction of travel of the beam and two polarizations in the plane transverse to the direction of propagation, which are mutually orthogonal. Though for many applications, the laser beam may be modeled as simply linearly or circularly polarized. All three of the polarization components become significant and must be considered when focusing laser beams tightly.

Another aspect of the laser beams that has been researched extensively is their transverse spatial structure. Many types of spatial patterns have been realized and observed experimentally in laser beams. Here, we will discuss several types of patterns that arise and also the polarization structure of these patterns for the Maxwell-Gauss laser

beam model.

The Gaussian beam polarization has been studied for “classical" beams such as Hermite and Laguerre Gauss beams [7–9]. In this work, such polarization descriptions for the Ince-Gauss and Airy beams are discussed and experimental results confirming these descriptions are presented [10, 11]. We also discuss how Ince-Gauss beams contain Hermite-Gauss and Laguerre-Gauss beam as special cases and provide experimental demonstration of these relations. With advances in technology and communication, the need for better descriptions of laser beams is needed. This includes many areas of photonics and related fields.

1.1 Polarization in CW laser beam modes

Most often, polarization in experiments concerning interference, diffraction, or scattering, of laser light is described as either linearly, circularly, or elliptically polarized states of a plane wave. In this case, laser light with linear polarization is represented by a scalar amplitude of the field times a real unit vector. Similarly, circular and elliptical states are also adequately described in this way. (In view of the opening comments it should be kept in mind that this particular characteristic to the polarization states of laser beams only accounts for the dominant transverse electromagnetic field oscillations).

Plane wave polarization allows linear and circular states of polarization. In terms of electric field amplitudes, general polarization for a plane wave can be expressed as

$$\vec{E}(\vec{r},t) = (E_x\hat{e}_1 + E_y e^{i\delta}\hat{e}_2)e^{i(kz-\omega t)}, \tag{1.1}$$

where δ is the relative phase between the two constant components, E_x and E_y, $\vec{r}$ is the

position vector, t is time, and it is assumed that the wave is traveling strictly in the $\hat{e}_3$ direction and orthogonal basis vectors $\hat{e}_1$ and $\hat{e}_2$ lie in the plane transverse to $\hat{e}_3$. Figure

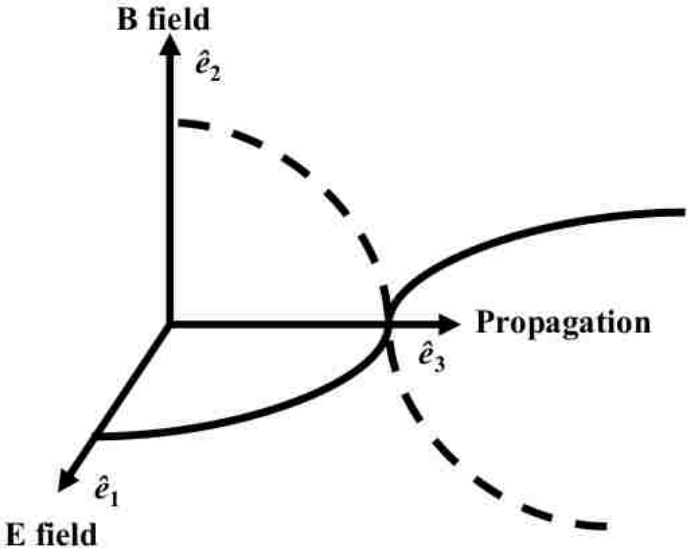

Figure 1.1: The general basis of $\hat{e}_1$, $\hat{e}_2$, and $\hat{e}_3$ is shown with $\vec{E}$ (solid) and $\vec{B}$ (dashed) curves as oscillating amplitudes in directions $\hat{e}_1$ and $\hat{e}_2$, respectively. The propagation direction, $\hat{e}_3$, is shown and will be defined as $\hat{e}_3 = \hat{z}$.

(1.1) shows an example of the coordinate system in the general $\hat{e}_1$, $\hat{e}_2$, and $\hat{e}_3$ basis.

The general $\hat{e}_1$, $\hat{e}_2$, and $\hat{e}_3$ basis is typically defined so that $\hat{e}_3 = \hat{z}$ is the plane wave propagation direction parallel to momentum vector $\vec{k}$. We will adhere to that convention. For plane wave polarization, there are two cases such that $E_x = E_y$ and $E_x \neq E_y$.

First, for $E_x = E_y$, we may vary δ from 0 to 2π. Here, we will define the bases $\hat{e}_1$ and $\hat{e}_2$ to be $\hat{x}$ and $\hat{y}$, respectively, for a "linear" polarization basis. When $\delta = 0$, the simplest type of polarization occurs where Equation (1.1) takes the form

$$\vec{E}(\vec{r}, t) = (E_x \hat{e}_1 + E_y \hat{e}_2) e^{i(kz - \omega t)}, \tag{1.2}$$

and a $+45°$ diagonal, linear polarization results. Figure (1.2) shows the corresponding

linear polarization at +45°.

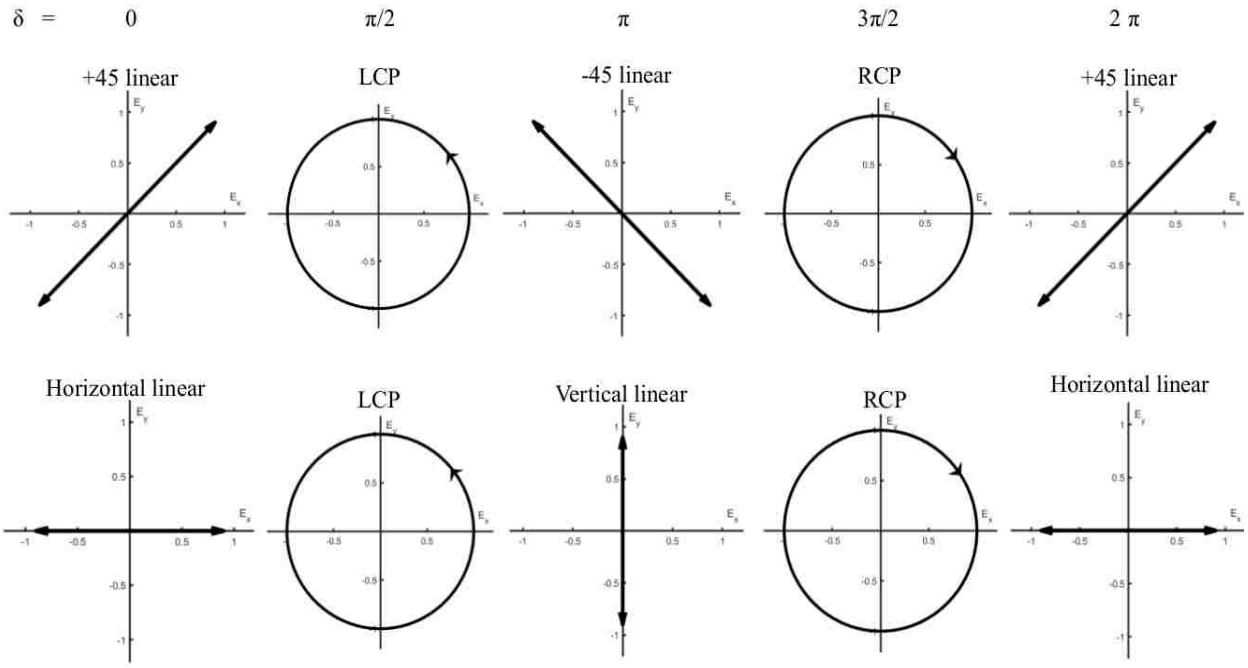

Figure 1.2: Types of plane wave polarization shown for $\delta = 0, \pi/2, \pi, 3\pi/2$, and 2π. The top shows the special δ cases for the basis $\hat{e}_1 = \hat{x}$, $\hat{e}_2 = \hat{y}$, and $\hat{e}_3 = \hat{z}$ for Equations (1.1)-(1.5). The bottom row shows the same evolution but with $\hat{e}_1 = \hat{x}'$, $\hat{e}_2 = \hat{y}'$, and $\hat{e}_3 = \hat{z}'$ given in Equation (1.6).

As δ increases from 0 to $\pi/2$, the polarization changes from the +45° linear state through continuous states of elliptical polarization until $\delta = \pi/2$ where Equation (1.1) becomes

$$\vec{E}(\vec{r}, t) = (E_x \hat{e}_1 + iE_y \hat{e}_2) e^{i(kz - \omega t)}, \tag{1.3}$$

and the components E_x and E_y oscillate out of phase by a constant 90°.

This produces a circular polarization state and the factor of i for the E_y component indicates that is the leading component. That is, as time passes and the plane wave travels along the $\hat{z}$ direction, the E_y component is always ahead of the E_x component by $\pi/2$ radians or 90°. This type of circular polarization is called Left-circular Polarization (LCP).

It is also important to note the LCP state is defined from the perspective that the plane wave is approaching the observer. If the perspective is from the source of the plane wave, then our LCP becomes "right-handed". The equations for the plane wave description are still valid for either perspective. We will follow the observer's perspective unless noted otherwise. The LCP is shown in Figure (1.2).

As δ increases further from $\pi/2$ to π, the LCP state transforms through continuous elliptical polarization states from $\delta = \pi/2$ until $\delta = \pi$. At $\delta = \pi$, Equation (1.1) becomes

$$\vec{E}(\vec{r},t) = (E_x\hat{e}_1 - E_y\hat{e}_2)e^{i(kz-\omega t)}. \tag{1.4}$$

This state of linear polarization is identical to that in Equation (1.2) except that for a negative sign on the component E_y. This state is a $-45°$ linear polarization and is shown in Figure (1.2). Continuing on with δ increasing from π to $5\pi/2$, the $-45°$ linear polarization continues transforming through elliptical states again until the "Right-handed" circular polarization, or RCP, is reached at $\delta = 3\pi/2$. At this point, Equation (1.1) is now

$$\vec{E}(\vec{r},t) = (E_x\hat{e}_1 - iE_y\hat{e}_2)e^{i(kz-\omega t)}, \tag{1.5}$$

where the factor for the E_y component is now $-i$ and the leading component is no longer E_y. The leading component is now E_x and the rotation of the electric field $\vec{E}(\vec{r},t)$ is in the opposite direction. From our observer perspective, this is RCP.

As δ further increases from $3\pi/2$ to 2π for one complete cycle, the RCP state transforms through elliptical states again and finally becomes the $+45°$ linear polarization that we started with at $\delta = 0$.

The states repeat for every δ cycle of 0 to 2π. Figure (1.2) also shows this evolution of

polarization for the case $E_x = E_y$.

For the second case, $E_x \neq E_y$ and for the whole range of δ, the resulting polarization state will always be elliptical, in general. The exceptions to this are when $E_x = 0, E_y \neq 0$ and $E_x \neq 0, E_y = 0$; the states of polarization for these exceptions are vertical and horizontal linear polarizations, respectively. These exceptions are also shown in Figure (1.2) in the bottom row with $\delta = 0$ and $\delta = \pi$ as horizontal and vertical polarizations, respectively.

The elliptical states existing for the case $E_x = E_y$ for $\delta \neq 0, \pi, \pi/2, 3\pi/2$, and 2π, and the $E_x \neq E_y$ case for $E_x \neq 0$ and $E_y \neq 0$, are many, but the "handed-ness", just as with the RCP and LCP states, is defined by $0 < \delta < \pi$ for "Left-handed" and $\pi < \delta < 2\pi$ for "Right-handed" elliptical states. Figure (1.3) shows an example of an ellipse with its major axis at $+45°$ and an elliptical state at $-45°$ as both right-handed and left-handed for each state totaling in four different states altogether.

Earlier, the basis of $\hat{e}_1$ and $\hat{e}_2$ were defined above as $\hat{x}$ and $\hat{y}$, respectively. However, Equation (1.1) may be written with a different choice of $\hat{e}_1$ and $\hat{e}_2$ basis. The crucial requirement is that the basis is linearly independent and orthonormal.

For example, the vertical and horizontal polarizations in Figure (1.2) may constitute a basis. This was the basis we chose as $\hat{x}$ and $\hat{y}$ and our Equations (1.1)-(1.5) hold. Alternatively, the $+45°$ and $-45°$ linear states could have been chosen. The only difference in this case would be that our current $\hat{x}$ and $\hat{y}$ basis would have to be rotated by $+45°$. This second choice is represented by the bottom row in Figure (1.2) with the rotated basis,

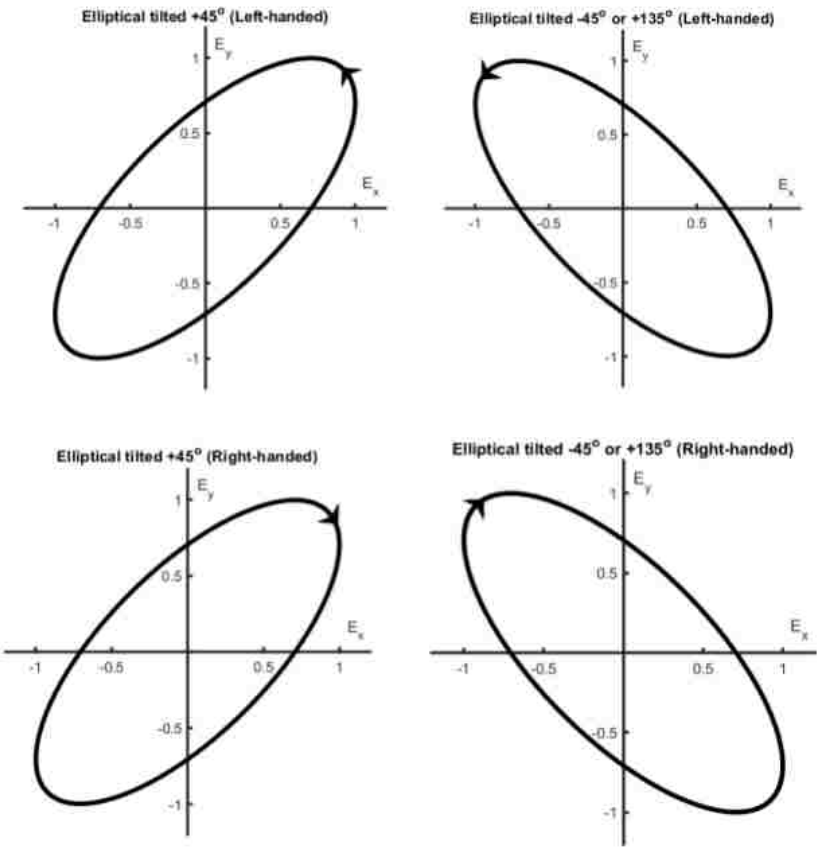

Figure 1.3: Example states of elliptical polarization for a plane wave. Each individual row and each individual column containing two elliptical states can each be used as a general basis for describing plane wave polarization.

$\hat{e}_1 = \hat{x}'$, $\hat{e}_2 = \hat{y}'$, and $\hat{e}_3 = \hat{z}'$ which are related to the un-primed basis by

$$\hat{x}' = \frac{1}{\sqrt{2}}(\hat{x} + \hat{y})$$
$$\hat{y}' = \frac{1}{\sqrt{2}}(\hat{x} - \hat{y})$$
$$\hat{z}' = \hat{z}. \tag{1.6}$$

In addition to using a linear basis, the RCP and LCP states themselves also form an orthonormal basis. This basis may be considered as a “circular" basis while the former is a “linear" basis. Standard plane wave descriptions follow one of these two bases in the Jones

Matrix formulation of polarization [6].

Thus, Equation (1.1) may be written in terms of a linear combination of orthogonal linear states or LCP and RCP states. Generalizing a bit further, for any given $\vec{E}(\vec{r},t)$, the electric field polarization may be expressed in any orthogonal combination of polarization states whether the states are linear, circular, or even elliptical.

An example of an elliptical basis would be that of the $+45°$ right-handed state in Figure (1.3) paired with the $-45°$ right-handed state in the same figure. This flexibility of the choice of basis allows for Equation (1.1) to be written as

$$\vec{E}(\vec{r},t) = (\vec{E}_1(t) + e^{i\delta}\vec{E}_2(t))e^{i(kz-\omega t)} \tag{1.7}$$

where $\vec{E}_1(t)$ and $\vec{E}_2(t)$ are any pair of orthogonal vectors. This completes the plane wave description of polarization.

It is important to recognize that the plane wave solution (1.1) is a valid solution for Maxwell's equations. However, once the finite transverse size of laser beam is introduced, plane wave polarization is no longer adequate to be a correct description of the polarization of finite size beams. Maxwell's equations cannot be satisfied in this way [7] and a more correct description of finite beam polarization is required.

1.2 Solutions of Maxwell Field Equations

A correct description for finite beam polarization begins by presuming a solution of the following form

$$\vec{E}(\vec{r},t) = \vec{E}(\vec{r})e^{i(kz-\omega t)}. \tag{1.8}$$

In Equation (1.8), $\vec{E}(\vec{r})$ is the amplitude as a function of position, $\vec{r}$, and it is also presumed that this field is a wave traveling predominantly in the positive z–direction with frequency ω and wave number $k = \omega/c$. The magnetic field will have an expression similar to that of Equation (1.8) with $\vec{E}$ replaced by $\vec{B}$. We begin with Maxwell's equations in free space

$$\nabla \cdot \vec{E} = 0, \tag{1.9}$$

$$\nabla \cdot \vec{B} = 0, \tag{1.10}$$

$$\nabla \times \vec{E} = -\frac{\partial \vec{B}}{\partial t}, \tag{1.11}$$

$$\nabla \times \vec{B} = \mu_0 \epsilon_0 \frac{\partial \vec{E}}{\partial t}, \tag{1.12}$$

where μ_0, ϵ_0 are the permeability and permittivity of free space and $1/\mu_0\epsilon_0 = c^2$, with c being the speed of light in free space. Substituting Equation (1.8) for the electric field and a similar expression for B in these equations we get,

$$ikE_z(\vec{r}) + \nabla \cdot \vec{E}(\vec{r}) = 0, \tag{1.13}$$

$$ikB_z(\vec{r}) + \nabla \cdot \vec{B}(\vec{r}) = 0, \tag{1.14}$$

$$ik\hat{z} \times \vec{E}(\vec{r}) + \nabla \times \vec{E}(\vec{r}) = ikc\vec{B}(\vec{r}), \tag{1.15}$$

$$ik\hat{z} \times \vec{B}(\vec{r}) + \nabla \times \vec{B}(\vec{r}) = -i\frac{k}{c}\vec{E}(\vec{r}). \tag{1.16}$$

Solving Equation (1.13) we get an expression for the longitudinal component.

$$E_z(\vec{r}) = \frac{i}{k}\left[\frac{\partial E_x}{\partial x} + \frac{\partial E_y}{\partial y} + \frac{\partial E_z}{\partial z}\right] \tag{1.17}$$

And, with the paraxial approximation, which is discussed in the beginning of the next chapter, where

$$\left|\frac{\partial E_z}{\partial z}\right| << \left|\frac{\partial E_x}{\partial x} + \frac{\partial E_y}{\partial y}\right| \tag{1.18}$$

we may drop the third term on the right hand side of Equation (1.17) giving us

$$E_z(\vec{r}) = \frac{i}{k}\left[\frac{\partial E_x}{\partial x} + \frac{\partial E_y}{\partial y}\right]. \tag{1.19}$$

A similar form is found for $\vec{B}$,

$$B_z(\vec{r}) = \frac{i}{k}\left[\frac{\partial B_x}{\partial x} + \frac{\partial B_y}{\partial y}\right]. \tag{1.20}$$

Now, the individual components of either $\vec{B}$ or $\vec{E}$ need to be determined in order to find our full vector field solution. It is possible, using both Faraday's law Equation (1.11) and Ampere's law Equation (1.12) to find the solutions to the components of $\vec{B}$ each in terms of E_x, E_y, E_z and the components of $\vec{E}$ in terms of B_x, B_y, B_z, respectively. Then, from Faraday's law, we get

$$B_x = \frac{i}{ck}\frac{\partial E_y}{\partial z} - \frac{1}{c}E_y + \frac{1}{ck^2}\left(\frac{\partial^2 E_x}{\partial x \partial y} + \frac{\partial^2 E_y}{\partial^2 y}\right), \tag{1.21}$$

and when Equation (1.19) is used together with the paraxial wave equation, we find

$$2ik\frac{\partial E_y}{\partial z} = \left(\frac{\partial^2}{\partial x^2} + \frac{\partial^2}{\partial y^2}\right)E_y, \tag{1.22}$$

$$B_x = -\frac{1}{c}E_y + \frac{1}{2ck^2}\left(\frac{\partial^2 E_y}{\partial y^2} - \frac{\partial^2 E_y}{\partial x^2}\right) + \frac{1}{ck^2}\left(\frac{\partial^2 E_x}{\partial y \partial x}\right). \tag{1.23}$$

Repeating the calculation for the remaining components of $\vec{B}$ and $\vec{E}$ using Ampere's law (1.12), and putting all the resulting formulas together, we have for the components of the

magnetic field [7]

$$B_x = -\frac{1}{c}E_y + \frac{1}{2ck^2}\left(\frac{\partial^2 E_y}{\partial y^2} - \frac{\partial^2 E_y}{\partial x^2}\right) + \frac{1}{ck^2}\left(\frac{\partial^2 E_x}{\partial y \partial x}\right), \tag{1.24}$$

$$B_y = \frac{1}{c}E_x + \frac{1}{2ck^2}\left(\frac{\partial^2 E_x}{\partial y^2} - \frac{\partial^2 E_x}{\partial x^2}\right) - \frac{1}{ck^2}\left(\frac{\partial^2 E_y}{\partial y \partial x}\right), \tag{1.25}$$

$$B_z = -\frac{i}{ck}\left(\frac{\partial E_y}{\partial x} - \frac{\partial E_x}{\partial y}\right), \tag{1.26}$$

and for the components of the electric field,

$$E_x = c\left[B_y + \frac{1}{2k^2}\left(\frac{\partial^2 B_y}{\partial x^2} - \frac{\partial^2 B_y}{\partial y^2}\right) - \frac{1}{k^2}\left(\frac{\partial^2 B_x}{\partial y \partial x}\right)\right], \tag{1.27}$$

$$E_y = c\left[-B_x + \frac{1}{2k^2}\left(\frac{\partial^2 B_x}{\partial x^2} - \frac{\partial^2 B_x}{\partial y^2}\right) + \frac{1}{k^2}\left(\frac{\partial^2 B_y}{\partial y \partial x}\right)\right], \tag{1.28}$$

$$E_z = \frac{ic}{k}\left(\frac{\partial B_y}{\partial x} - \frac{\partial B_x}{\partial y}\right). \tag{1.29}$$

These six equations allow a complete field description equation in the paraxial approximation. They describe polarization properties consistent and in agreement with Maxwell equations. Note that the plane wave solution is retained, $E = cB$ as a special case, when all field amplitudes are constant with respect to position. Therefore, Equations (1.24)-(1.29) describe paraxial solutions to Maxwell's equations. They are correct to order $1/(kw)^2$, where $k = 2\pi/\lambda$ is the wavenumber and w is the beam spot size of the field transverse to the direction of propagation [7]. For Equations (1.24)-(1.29), the expansion is carried out to first leading order beyond the scalar wave approximation.

We also introduce the idea of dominant polarization. In the limit of large transverse size, paraxial beams approach a plane wave with a particular polarization component. This component will be referred to as the dominant component. For example, if a fundamental Gaussian beam solution reduces to a plane wave linearly polarized in the $\hat{x}$ direction, we

say that the Maxwell beam has a dominant x-polarization. Equations (1.27)-(1.29) for such a beam reduce to

$$E_x = A\psi(\vec{r}), \tag{1.30}$$

$$E_y = \left(\frac{A}{2k^2}\right)\frac{\partial^2\psi(\vec{r})}{\partial x \partial y}, \tag{1.31}$$

$$E_z = \left(\frac{iA}{k}\right)\frac{\partial\psi(\vec{r})}{\partial x}, \tag{1.32}$$

where A is a constant and $\psi(\vec{r})$ is the scalar amplitude of the dominant polarization, which would be the Gaussian solution for this example [7]. Equations (1.30)-(1.32) apply to any amplitude, $\psi(\vec{r})$, of a linearly polarized beam be it an HG, LG, or IG mode or any other beam modes.

From Equations (1.30)-(1.32), the relative amplitudes of the field components relative to the dominant component are smaller by factors of $1/kw \approx E_z/E_x$ and $1/(kw)^2 \approx E_y/E_x$. Then, the approximation of E_y, $E_z \to 0$ is adequate for experiments where polarization is not of interest. For example, if we are only interested in total power transported by the beam, then a paraxial description with $E_y \approx 0$ and $E_y < E_z$ may be adequate. However, E_y cannot be ignored if polarization properties or focusing of a beam [7] are involved. In a simple experiment, where an x-polarized beam is passed through a pair of crossed polarizers we don't observe zero transmitted intensity. At the same time, E_z certainly is present and is in fact $E_z > E_y$, but this longitudinal component is not measured and does not affect the outcome of these investigations. Researchers have attempted measurements of the longitudinal component for electromagnetic waves using quantum dots [12–14].

Polarization of interacting fields in non-linear materials is even more important where

interaction has explicit dependence on polarization. This emphasizes the importance of a correct description of polarizations in electrodynamic systems.

In Chapter 2, the paraxial approximation is introduced and the paraxial wave equation (PWE) is derived from the free space Maxwell equations. A variety of solutions to the PWE are discussed. And, the Hermite-Gauss (HG) and Laguerre-Gauss (LG) modes are introduced as a prelude to the introduction of the Ince-Gauss modes in Chapter 4.

Chapter 3 introduces the Airy beam as another solution to the PWE. This displays some unusual propagation behavior which is discussed. We discuss the basic properties of this beam regarding propagation and polarization. This chapter also explains the experiment performed and methods used to analyze and compare experiments with the theoretical prediction.

Chapter 4 introduces the Ince-Gauss (IG) modes as solutions to the PWE. Their relation to the HG and LG family of modes is also discussed. The polarization properties of these beams are discussed along with their propagation properties. The experiment and methods are also discussed with results compared to theoretical prediction.

Chapter 5 summarizes principal results and conclusions of the thesis and offers some possible projects for future investigations.

Chapter 2

Paraxial Waves in free space: Hermite-Gauss (HG) and Laguerre-Gauss (LG) Beams

It is well known that one may obtain the second order partial differential (wave equation) equation for either the electric or magnetic field components from Maxwell's equations in free space. Many solutions of this wave equation under the approximation that the transverse spatial extent of these electric field components changes slowly with the change in longitudinal displacement are known [6]. This approximation is known as the paraxial approximation. As mentioned previously, although Maxwell's equations do require any such finite transverse field to have all three field components, the paraxial approximation of the wave equation allows us to focus on a single dominant scalar function as its solution. As a further note, solutions for Maxwell's equations will satisfy the wave equation, but not all solutions of the wave equation will work for Maxwell's equations unless constraints have been made to those wave equation solutions. Also, solutions of the wave equation under the paraxial approximation can be used to construct paraxial solutions for Maxwell's equations as shown in Section 1.2 of the previous Chapter.

In the present chapter, we will begin with Maxwell's equations in free space and derive the paraxial wave equation (PWE) and discuss solutions to that equation. Since the paraxial wave equation is itself another second order PDE, it affords us the opportunity to have several families of solutions depending on the symmetry or the coordinate system used for solving the equation. We will derive the fundamental solution and present the higher order solutions with some discussion only for the Hermite-Gauss and

Laguerre-Gauss family of paraxial solutions. This work is primarily concerned with the Airy beam and Ince-Gauss beam. We will derive and discuss those solutions in Chapters 3 and 4, respectively.

2.1 Maxwell's equations in free space and the Paraxial wave equation

Maxwell's equations in free space, in SI units, are given by

$$\nabla \cdot \vec{E} = 0, \tag{2.1}$$

$$\nabla \cdot \vec{B} = 0, \tag{2.2}$$

$$\nabla \times \vec{E} = -\frac{\partial \vec{B}}{\partial t}, \tag{2.3}$$

$$\nabla \times \vec{B} = \mu_0 \epsilon_0 \frac{\partial \vec{E}}{\partial t}. \tag{2.4}$$

We first obtain the wave equation by taking the curl of Equation (2.3), and then using the vector identity,

$$\nabla \times \nabla \times \vec{V} = \nabla(\nabla \cdot \vec{V}) - \nabla^2 \vec{V}, \tag{2.5}$$

to write the result as

$$\nabla(\nabla \cdot \vec{E}) - \nabla^2 \vec{E} = -\frac{\partial}{\partial t}(\nabla \times \vec{B}). \tag{2.6}$$

By Gauss' law, Equation (2.1), the first term is zero. Also, for curl $\vec{B}$, we may use Ampere's law Equation (2.4) which yields the wave equation in terms of the electric field only.

$$\nabla^2 \vec{E} = \frac{1}{c^2} \frac{\partial^2}{\partial t^2} \vec{E} \tag{2.7}$$

One obtains an identical equation in terms of $\vec{B}$ only. From here, we can use the paraxial approximation to obtain the paraxial wave equation (PWE).

The paraxial approximation is needed to describe beam-like soutions, where beam-like characteristics are that the wave travels predominantly in $\hat{z}$ direction like a plane wave, has finite size representing the finite energy of the wave (unlike a plane which is infinite), and the wave diffracts slowly, i.e. changes shape slowly, in the x-y plane while traveling in the $\hat{z}$ direction.

To begin, we will rewrite Equation (2.7) as

$$\left(\nabla_{\perp}^2 + \frac{\partial^2}{\partial z^2} - \frac{1}{c^2}\frac{\partial^2}{\partial t^2}\right)\vec{E} = 0, \tag{2.8}$$

where $\nabla_{\perp}^2$ indicates the Laplacian in the $x-y$ plane only and we assume that the wave is traveling predominantly in the $+\hat{z}$ direction. We can expand the LHS out, term by term, assuming that the solution for $\vec{E}$ has the following form

$$\vec{E} = \vec{E_0}(x, y, z)e^{i(kz-\omega t)}, \tag{2.9}$$

where $\omega = 2\pi\nu$, $k = 2\pi/\lambda$ where λ is the wavelength, and ν is the frequency. The argument of E_0 will be suppressed with the understanding that it is, for now, dependent on variables x, y, and z. It should also be understood that $\vec{E_0}$ may also be complex. The expanded version of Equation (2.8) has the form

$$\nabla_{\perp}^2\vec{E_0} + \left[\frac{\partial^2\vec{E_0}}{\partial z^2} + 2ik\frac{\partial\vec{E_0}}{\partial z} + k^2\vec{E_0}\right]e^{i(kz-\omega t)} - \frac{\omega^2}{c^2}\vec{E_0}e^{i(kz-\omega t)} = 0. \tag{2.10}$$

The approximation that E_0 changes slowly as the displacement z changes is defined by the

inequality

$$\left|\frac{\partial^2 \vec{E}_0}{\partial z^2}\right| << \left|2k\frac{\partial \vec{E}_0}{\partial z}\right|, \tag{2.11}$$

which allows us to drop the second order term. With this approximation, the PWE [6] takes the form

$$\nabla_\perp^2 \vec{E}_0 + \left[2ik\frac{\partial \vec{E}_0}{\partial z} + k^2 \vec{E}_0\right] e^{i(kz-\omega t)} - \frac{\omega^2}{c^2}\vec{E}_0 e^{i(kz-\omega t)} = 0. \tag{2.12}$$

Lastly, the zeroth order terms cancel assuming that the dispersion relation is simply $c = \omega/k$. Then, we may write the paraxial wave equation as

$$\nabla_\perp^2 \vec{E}_0 + 2ik\frac{\partial \vec{E}_0}{\partial z} = 0. \tag{2.13}$$

Equation (2.13) is the vector PWE. If $\vec{E}_0$ is written in terms of its Cartesian components, we find that both components satisfy a scalar PWE,

$$\nabla^2 \psi + 2ik\frac{\partial \psi}{\partial z} = 0, \tag{2.14}$$

where ψ in Equation (2.14) represents a Cartesian component of the field. This is the equation we will be dealing with in this chapter. From Equation (2.14), the fundamental Gaussian and higher order scalar solutions are derived.

2.2 Solutions of the Paraxial wave equation

The PWE (2.14), can be solved in a variety of ways in several different coordinate systems. A solution common to both cartesian and circular cylindrical coordinate systems is the so-called fundamental Gaussian solution. The method of separation of variables allows us

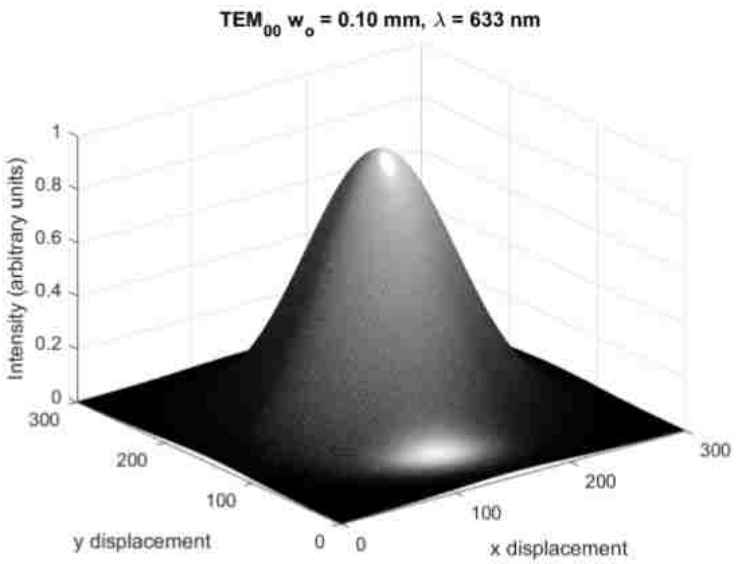

Figure 2.1: Fundamental Gaussian mode with $w_0 = 0.1$ mm at $\lambda = 633$ nm at the focal plane, $z = 0$ cm.

to write the solution as a product of functions one for each coordinate. That is, ψ can be factored as a product of three independent functions. Moving forward, we will now derive the fundamental mode and discuss some key properties that will help with the discussion of the Airy beam as will in Chapter 3.

2.2.1 Gaussian Beam Solution and Properties

The fundamental solution to Equation (2.14) is the Gaussian beam solution which is [6]

$$\psi(\vec{r}) = \left(\frac{2}{\pi}\right)^{1/2} \frac{\exp(ikz - i\phi_0(z))}{w(z)} \exp\left(-\frac{x^2+y^2}{w^2(z)} + ik\frac{x^2+y^2}{2R(z)}\right). \tag{2.15}$$

In Equation (2.15), we assume a beam traveling predominantly in the $\hat{z}$ direction, $w(z)$ is the beam radius at z, $R(z)$ is the beam's radius of curvature at z, and $\phi_0(z)$ is the Guoy phase of the beam at z. It can be checked that Equation (2.15) satifies the PWE (2.14).

Figure (2.1) shows an example of the intensity of the Gaussian mode $\propto |\psi|^2$, the normalized square modulus of Equation (2.15).

Beam Radius $w(z)$

The beam radius at z is

$$w(z) = w_0\sqrt{1 + (z/z_R)^2}, \tag{2.16}$$

where $z_R = \pi w_0^2/\lambda$ is the Rayleigh range and w_0 is the beam radius at the focus, $z = 0$, also referred to as the beam waist [6]. Figure (2.2) shows a plot of the general behavior of $w(z)$ around the beam waist and up to $z = \pm z_R$. Near the waist, $w(z)$ is non-linear, but at $z = \pm z_R$, $w(z)$ becomes linear with z. The distance between $-z_R$ to $+z_R$ is called the confocal parameter.

Radius of Curvature $R(z)$

The radius of curvature, $R(z)$, is a function of z as [6]

$$R(z) = z\left(1 + (z_R/z)^2\right). \tag{2.17}$$

The radius of curvature refers to the of curvature of the phase front, K, of the beam where $R(z) \propto 1/K$. At $z = 0$, R is infinite corresponding to no curvature at all or planar phase front. For $z > 0$, R is positive and decreases to a minimum R value at z_R. After this minimum radius of curvature, R increases linearly with z to infinity. Similar asymptotic behavior occurs for $z < 0$, but R is negative. Figure (2.3) shows the behavior of $R(z)$ as z a reaches the limits of the confocal parameter range.

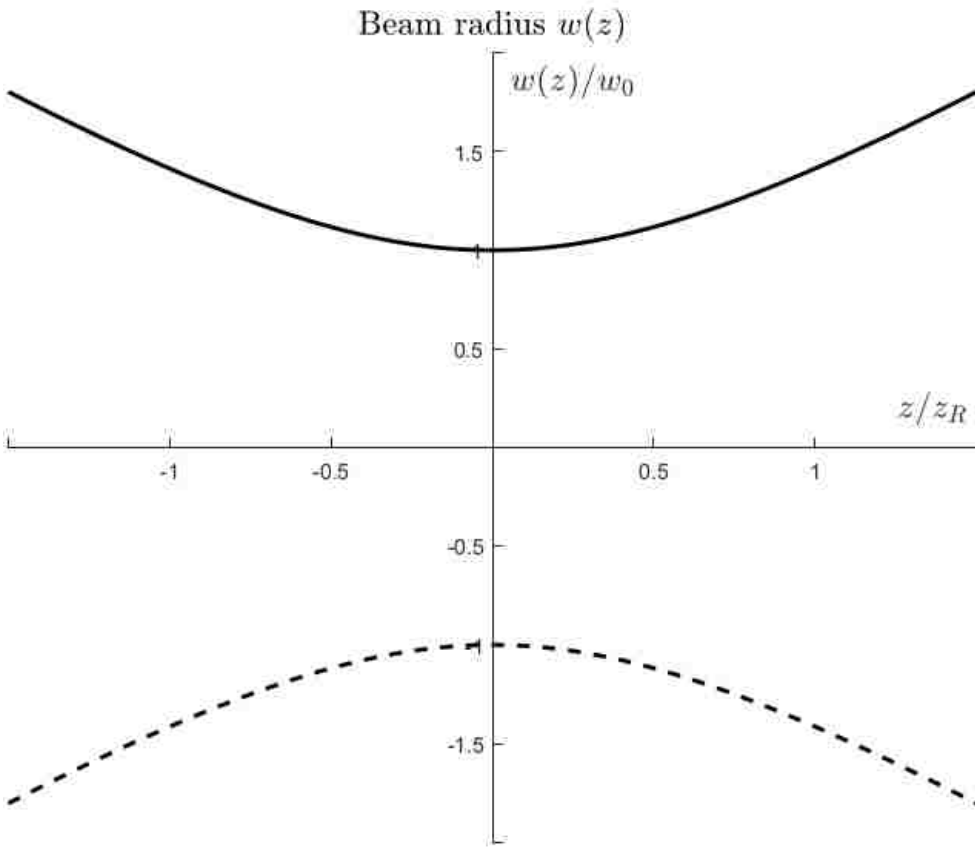

Figure 2.2: Behavior of the beam radius, w_0, of curvature for $z_R = 155$ m for $\lambda = 633$ nm.

Guoy Phase

The Guoy phase is for the fundamental Gaussian is

$$\phi_{Guoy}(z) = \tan^{-1}(z/z_R), \tag{2.18}$$

and Figure (2.4) shows a plot of its behavior. If the beam begins at $z = -z_R$ and passes through the beam waist up to $z = +z_R$, a Guoy phase shift of π is attained since the direction of the curvature flips as shown in Figure (2.4) (there is also kz, which is also part of the full phase).

The beam properties mentioned, $R(z)$, $w(z)$, and $\phi_{Guoy}(z)$, apply to the fundamental Gaussian Equation (2.15) as well as for higher order solutions. These properties may also

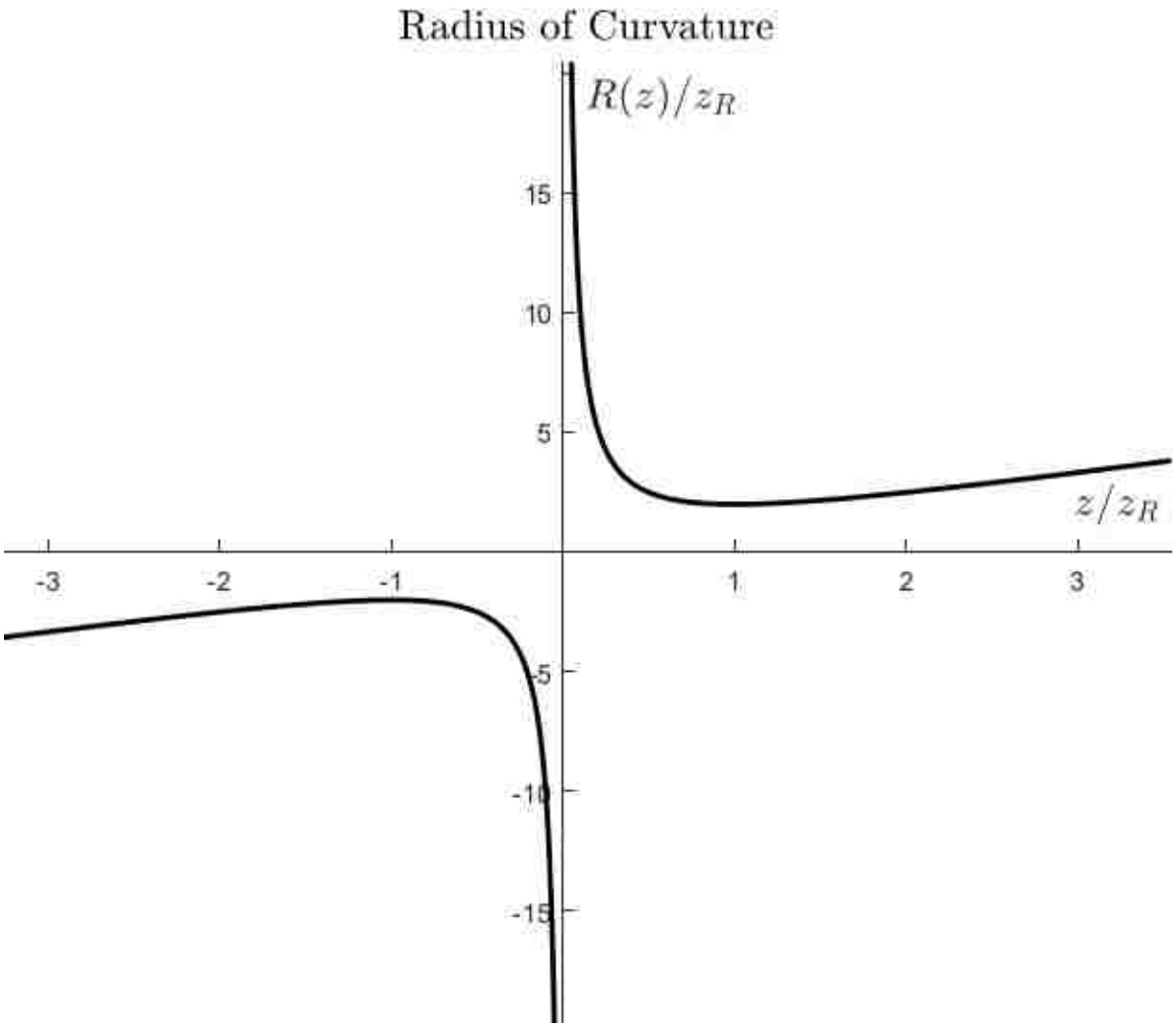

Figure 2.3: Behavior of the radius of curvature for $z_R = 155$ m for $\lambda = 633$ nm.

be described by a complex beam parameter, $q(z)$, discussed next.

Complex Beam Parameter$q(z)$

In geometrical optics, ray transfer ABCD matrices (2×2 dimensions) are used to determine trajectories of optical rays through optical elements such as lenses, waveplates, and polarizers where each element corresponds to an optical element. For a Gaussian beam in the paraxial approximation, the same ABCD matrices may be used in complex

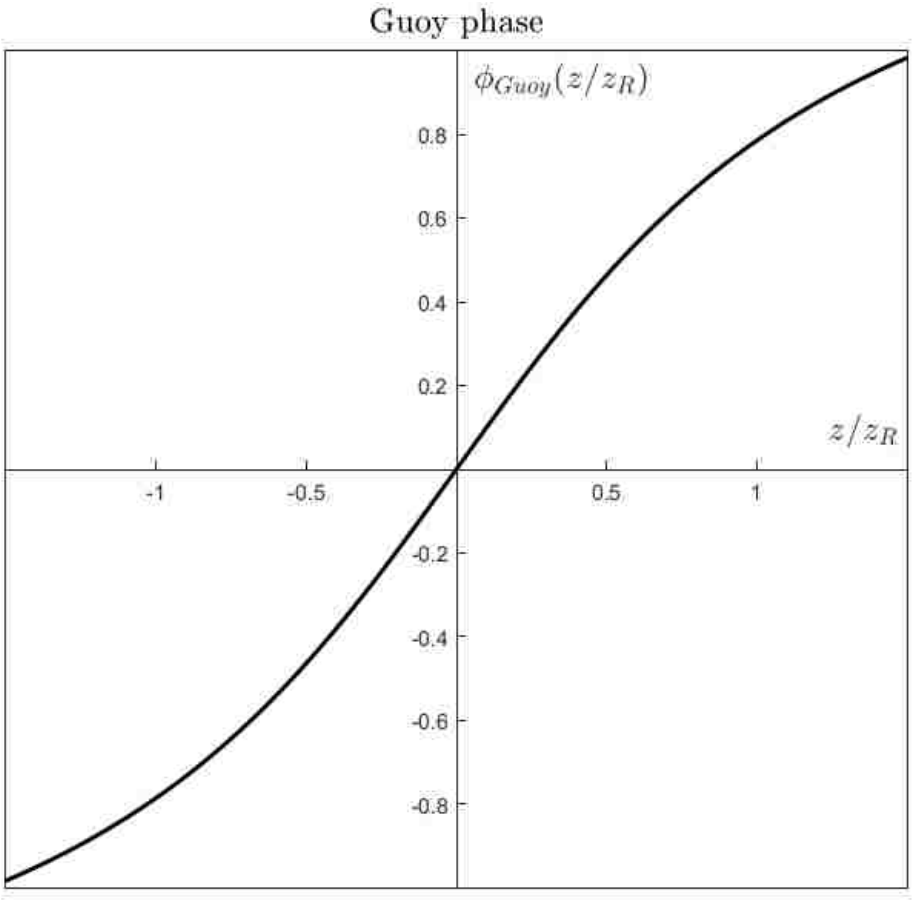

Figure 2.4: Behavior of Gaussian Guoy phase, $\phi_{Guoy}(z)$, for $z_R = 155$ m for $\lambda = 633$ nm.

transformation as [6]

$$q_f = \frac{Aq_i + B}{Cq_i + D}, \tag{2.19}$$

where A, B, C, and D are the elements of the ABCD matrices, q_i is the initial beam parameter, and q_f is the final beam parameter. The beam parameter $q(z)$ is defined by

$$\frac{1}{q(z)} = \frac{1}{R(z)} - i\frac{\lambda}{\pi w^2(z)} \tag{2.20}$$

or

$$q(z) = z + iz_R. \tag{2.21}$$

By using Equations (2.19) and (2.20) with Equation (2.18), the evolution of the Gaussian beam can be determined for propagation, refraction, reflection, etc.

The expression for the Gaussian beam may be written in a slightly different form using $q(z)$ as [6]

$$\left(\frac{2}{\pi}\right)^{1/2} \frac{q_i}{w_0 q_f} \exp\left[ikz + ik\frac{x^2+y^2}{2q_f(z)}\right]. \tag{2.22}$$

Next, we introduce higher order solutions that have the same Gaussian properties but have the extra characteristic of symmetry depending on the coordinate system used to solve the PWE (2.14).

2.2.2 Higher order solutions: Hermite-Gauss and Laguerre-Gauss modes

From the fundamental Gaussian solution, higher order modes are possible and are the result of the symmetry of the coordinate system used to solve Equation (2.14). These higher order solutions may be labeled as ψ_{mn} where m and n are indices that describe the order of the beam. The two coordinate systems of interest are the Cartesian and circular cylindrical coordinates which give rise to the Hermite-Gauss and Laguerre-Gauss modes, respectively. Derivations for these higher order modes can be found in Lasers by Siegman [6].

Hermite-Gauss modes

The HG modes solutions to Equation (2.14) are given by [6]

$$\begin{aligned} HG_{mn}(\vec{r}) = & \sqrt{\frac{2}{\pi m!n!2^{m+n}}}\frac{1}{w(z)} \\ & \times \exp\left(\frac{-(x^2+y^2)}{w^2(z)} + ik\frac{(x^2+y^2)}{2R(z)} - i(m+n+1)\phi_0\right) \\ & \times H_m(\sqrt{2}x/w(z))H_n(\sqrt{2}y/w(z)), \end{aligned} \tag{2.23}$$

where m and n integers indicate the order of the Hermite polynomials, $H_m(\sqrt{2}x/w)$ and $H_n(\sqrt{2}y/w)$, respectively. In this notation, the fundamental Gaussian will be denoted by HG_{00}. The beam spot size is $w(z)$, the Gouy phase, $(m+n+1)\tan^{-1}(z/z_R)$, and radius of curvature, $R(z)$, have the same definition as before with the fundamental Gaussian solution. As can be seen from the phases present in the amplitude, much of the characteristics regarding propagation and relative size follow the same trends as the fundamental mode, but the main difference is, of course, the Hermite polynomials which are also solutions to the harmonic oscillator with a quadratic potential function. The first five of an infinite, complete set of the Hermite polynomials, $H_n(x)$, are listed below [15].

$$\begin{aligned} H_0(x) &= 1 & H_4(x) &= 16x^4 - 48x^2 + 12 \\ H_1(x) &= 2x & &\vdots \\ H_2(x) &= 4x^2 - 2 & H_n(x) &= (-1)^n e^{-x^2}\frac{d^n}{dx^n}e^{-x^2} \\ H_3(x) &= 8x^3 - 12x & & \end{aligned} \tag{2.24}$$

From just the first few modes, the pattern of the amplitudes of HG_{mn} is evident. For $N = 1 = n + m$, we have either n or $m = 1$ while the other is 0. According to the

polynomials, order of 1 results in a nodal line along the x or y axis for $m = 1$ or $n = 1$, respectively. Order increased to $N = 2$ allows for HG_{11}, HG_{20}, or HG_{02}. Shown below are the intensities for orders $N = 1 - 2$ and 6 in Figure (2.5).

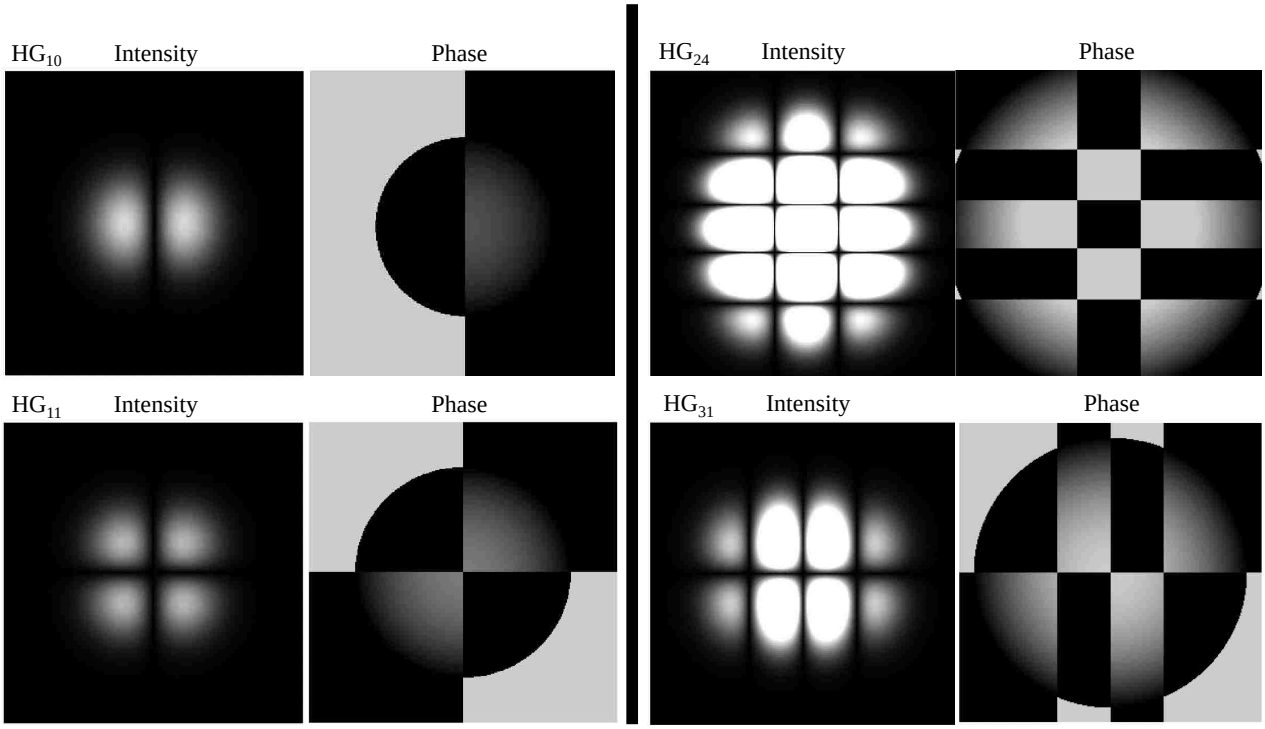

Figure 2.5: HG_{10} and HG_{11} intensity profiles and phases shown on the left right. HG_{24} and HG_{31}

This pattern is a predictable one that allows one to immediately determine the order of the beam by counting the number of nodal lines in vertical and horizontal directions. From the figure, an important feature emerges, viz, the relative phases between adjacent peaks are seen to be alternating in phase by π. For HG_{11}, there is bilateral symmetry present. Two "diagonal" peaks will be in phase while the two "off diagonal" peaks are out of phase by 180°.

Laguerre-Gauss modes

Solutions of the scalar PWE (2.14) in the circular cylindrical coordinate system, reflecting the symmetry of the local coordinate system are the LG modes given by [6]

$$LG_{lp}(\rho,\phi,z) = \left(\frac{\sqrt{2}\rho}{w(z)}\right)^{l} L_p^l\left(\frac{2\rho^2}{w(z)^2}\right)\exp\left(\frac{ik\rho^2}{2q(z)} + il\phi - i(|l|+2p)\phi_0(z)\right) \tag{2.25}$$

In this solution, $q(z)$ is the complex beam parameter and the cylindrical coordinates are radial distance ρ from the beam axis, polar angle ϕ (or azimuthal) from the $+x$-axis, and longitudinal distance z. The fundamental Gaussian mode is LG_{00}. The indices for the associated Laguerre polynomials are l and p where l may be negative or positive. These polynomials also form an orthogonal, complete set of functions.

And, the polynomials are generated from the series [15]

$$L_p^l(x) = \sum_{i=0}^{n}(-1)^i\binom{n+l}{n-i}\frac{x^i}{i!}. \tag{2.26}$$

When p is chosen as some integer value with l some integer as well, the solutions for the amplitude reveal radially symmetric patterns. The simplest case of $p=0$ and $l=1$ corresponds to a mode that exhibits a single ring, the smallest ring, with a dark center. The first few polynomials are listed below. [15]

$$\begin{aligned} L^0(x) &= 1 & L^3(x) &= \frac{1}{6}(-x^3+9x^2-18x+6) \\ L^1(x) &= -x+1 & &\vdots \\ L^2(x) &= \frac{1}{2}(x^2-4x+2) & L^n(x) &= \frac{e^x}{n!}\frac{d^n}{dx^n}(e^{-x}x^n) \end{aligned} \tag{2.27}$$

The p subscript was dropped since $p=0$ in Equation (2.27) above and $L_0^l \equiv L^l$.

The LG modes have many similar behaviors and properties as LG_{00}, but when the

order is higher than 0 there are distinguishing characteristics that sets the LG modes apart from the fundamental mode and HG modes.

Due to the circular symmetry, the LG modes have the general intensity profile as a ring with some width and a dark center. As mentioned, $p = 0$ and $l \neq 0$ have intensities with a single ring and a dark center. For $p \neq 0$ and $l \neq 0$, we have intensities with multiple, concentric rings with a dark center except when $l = 0$, there is a bright center with concentric rings. Figure (2.6) shows examples of LG beams with $p = 0$ and Figure (2.7) with $p \neq 0$.

Due to the fact that LG beams with $l \neq 0$ have orbital angular momentum (OAM), the phase is another unique characteristic in that the phase fronts are helical. The phase of LG beams is helical with the helical axis along the direction of propagation. The term, $\exp(il\phi)$, in Equation (2.25) is responsible for the helical part of the phase of the beam. The order of the beam l determines the rate at which the helix turns. For example, for $l = 1$, the term becomes $\exp(i\phi)$ and one cycle of ϕ from 0 to 2π corresponds to one rotation of the phase. However, for $l = 2$, we have $\exp(i2\phi)$ and for the same cycle of ϕ, the full rotation of the phase amounts to a full 4π as opposed to 2π for $l = 1$. When $l = 0$, there is no rotation in the phase and no OAM which accounts for the bright centers for LG beams with $p \neq 0$ and $l = 0$. No singularity in the phase is present. Also, since l can be a negative integer, the term now becomes $\exp(-il\phi)$. This change in sign changes the direction of the helicity, and therefore, changes the handed-ness of the OAM of the LG beam.

The stationary solutions for the IG modes can be expressed in terms of HG and LG modes [16]. All three modes, HG, LG, and IG, are described with complete sets of

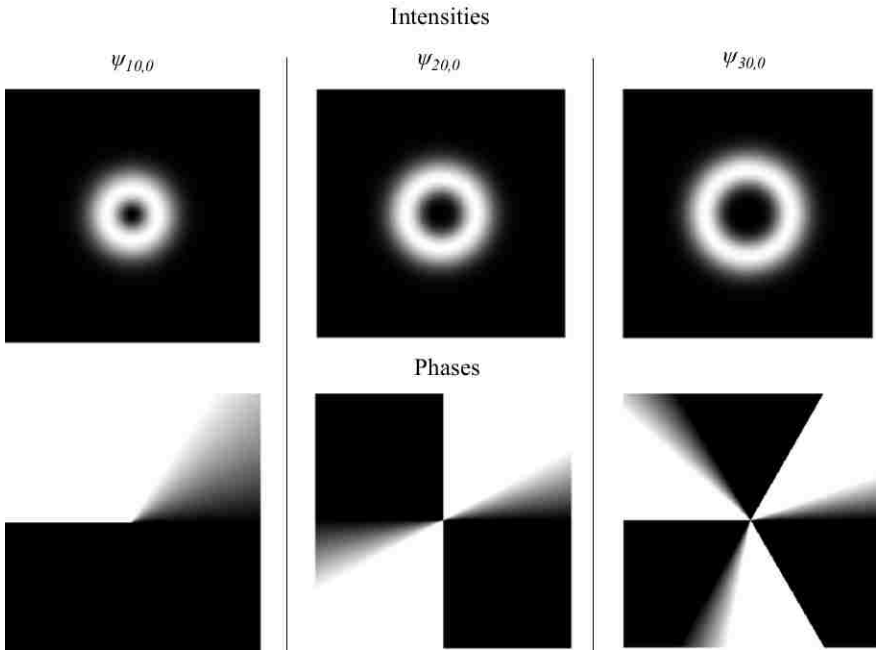

Figure 2.6: LG intensity and phase profiles for $l = 10$, 20, and 30 for $p = 0$ showing single ring structures. The same x-y range was used for all plots. In the intensity plots, note that the radius of the ring increases as the order, l, increases.

Hermite, Laguerre, and Ince polynomials, respectively. The expansions from HG to LG, LG to HG, IG to HG or LG and vice versa and their coefficients have been determined and the interested reader may refer to Boyer et al [17].

2.2.3 Other solutions Airy, Bessel, etc.

Besides the HG and LG solutions, there are many other solutions that are separable in other coordinate systems and thus reflect other symmetries in the transverse plane. Examples of such solutions include Bessel [16, 18], Helmholtz [19], Mathieu [20], Ince-Gauss (IG) [21], Airy [22, 23], parabolic [24], etc. Again, in this work, Airy and IG beams are of primary interest. In the next chapter, the Airy beam solution, its generation, and propagation properties are discussed including the experiment and analysis. The chapter after that discusses IG beams in much the same manner.

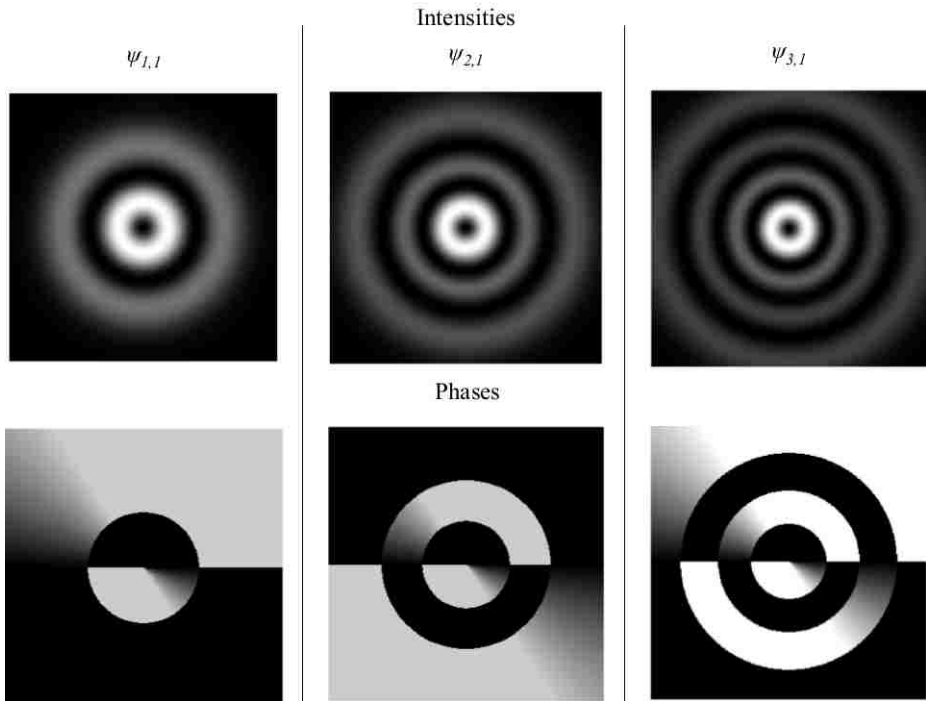

Figure 2.7: LG intensity and phase profiles for $l = 11$, 12, and 12 for $p \neq 0$ showing increases number of concentric ring structures.

Chapter 3

Polarization Properties of the Airy Beam

In this chapter, we introduce the Airy beam as another solution to the PWE (2.15). We derive an expression for the amplitude of the Airy beam and then discuss some of its properties related to propagation and polarization. Then, the experimental procedure for measuring these properties, as well as intensity profiles of the dominant and cross polarization components for the Airy beam and their evolution in propagation is discussed.

3.1 Airy beam solution of the Paraxial wave equation

Another solution to the PWE, the so-called Airy beam, was first proposed by Michael Berry in 1978 [25]. Twenty years later, the Airy beam was realized experimentally as a solution to the PWE [23].

To begin, we may assume a solution for the PWE as

$$\psi(x,y,z) = \psi_x(x,z)\psi_y(y,z) \tag{3.1}$$

where $\psi(x,y,z)$ may be complex, in general. For convenience, we will scale the coordinates x, y, and z relative to a characteristic length x_0 such that

$$\tilde{x} = \frac{x}{x_0}, \quad \tilde{y} = \frac{y}{y_0}, \quad \tilde{z} = \frac{z}{kx_0^2} \tag{3.2}$$

where we assume $x_0 = y_0$, k is still the wavenumber, and now the coordinates are dimensionless.

The value of x_0 is the location of the greatest peak for the unscaled Airy function. We shall see that the parameter x_0 characterizes the width of the largest peak in the intensity

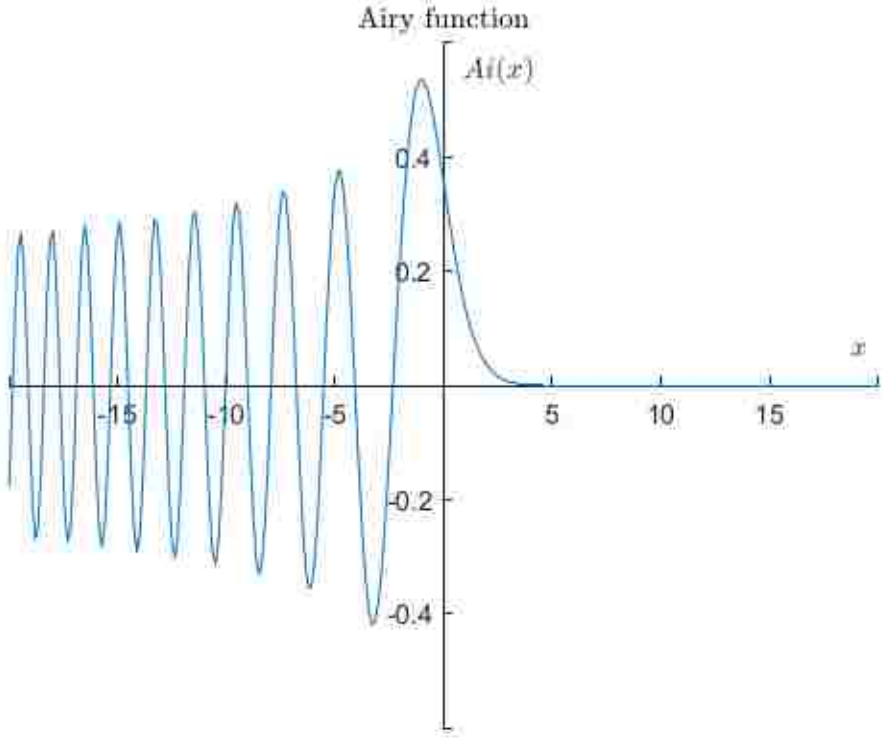

Figure 3.1: Un-scaled Airy function extends infinitely as $x \to -\infty$. Absolute maximum is plotted as a dot at $x_0 = 1.5$, and the distance from the origin to x_0 is the scaling parameter for the coordinates in (3.2).

pattern of the Airy beam solution. Figure (3.1) below shows a one dimensional plot of the Airy function. After scaling the variables and substituting Equation (3.1) into the PWE (2.14), we get,

$$\frac{\partial^2\psi(\tilde{x},\tilde{y},\tilde{z})}{\partial\tilde{x}^2} + \frac{\partial^2\psi(\tilde{x},\tilde{y},\tilde{z})}{\partial\tilde{y}^2} + 2i\frac{\partial\psi(\tilde{x},\tilde{y},\tilde{z})}{\partial\tilde{z}} = 0. \tag{3.3}$$

On carrying out the differentiation and dividing each side by $\psi_{\tilde{x}}\psi_{\tilde{y}}$, we obtain

$$\left[\frac{1}{\psi_{\tilde{x}}}\frac{\partial^2}{\partial\tilde{x}^2}\psi_{\tilde{x}} + \frac{2i}{\psi_{\tilde{x}}}\frac{\partial}{\partial\tilde{z}}\psi_{\tilde{x}}\right] + \left[\frac{1}{\psi_{\tilde{y}}}\frac{\partial^2}{\partial\tilde{y}^2}\psi_{\tilde{y}} + \frac{2i}{\psi_{\tilde{y}}}\frac{\partial}{\partial\tilde{z}}\psi_{\tilde{y}}\right] = 0, \tag{3.4}$$

where each bracketed term must each separately vanish. Thus we look to solve for a single

variable solution. The equation to be solved is

$$\left[\frac{\partial^2}{\partial\tilde{x}^2}\psi_{\tilde{x}} + 2i\frac{\partial}{\partial\tilde{z}}\psi_{\tilde{x}}\right] = 0 \tag{3.5}$$

where $\psi_{\tilde{x}}(\tilde{x},\tilde{z})$ is the solution we seek. For a simple solution, we use $\mathrm{Ai}(\tilde{x},\tilde{z}=0)$ to obtain an expression with this initial condition, and then apply an integral transform to obtain a more general solution $\mathrm{Ai}(\tilde{x},\tilde{z})$ with the propagation dependence on z known explicitly.

The Airy function is defined as

$$\mathrm{Ai}(x) = \frac{1}{2\pi}\int_{-\infty}^{+\infty} e^{ix\zeta+\frac{i\zeta^3}{3}}\,d\zeta, \tag{3.6}$$

where ζ is a complex variable [22]. Equation (3.6) can be shown to satisfy the PWE, and a full solution can be constructed such that

$$\psi(x,y,z) = \mathrm{Ai}(\tilde{x},\tilde{z})\mathrm{Ai}(\tilde{y},\tilde{z}). \tag{3.7}$$

However, Equation (3.6) cannot correctly describe a real Airy beam because the Airy function extends to $\pm\infty$ as shown in Figure (3.1). This would imply an infinite amount of energy for the Airy beam much like the plane wave solution. To keep the Airy function bounded and of finite extent and energy, we introduce a dimensionless truncation factor in the form of an exponential [23].

This exponential factor has the effect of having the Airy function approach zero rather than oscillate for an infinite distance along the x or y axis. This finite version of the Airy function is a realistic characterization since the energy of a real Airy beam must be finite. Figure (3.2) shows the intensity of such a beam for $a = 0.4$ near the beam waist. Note that the sign of the argument of the exponential in Equation (3.8) is positive indicating the

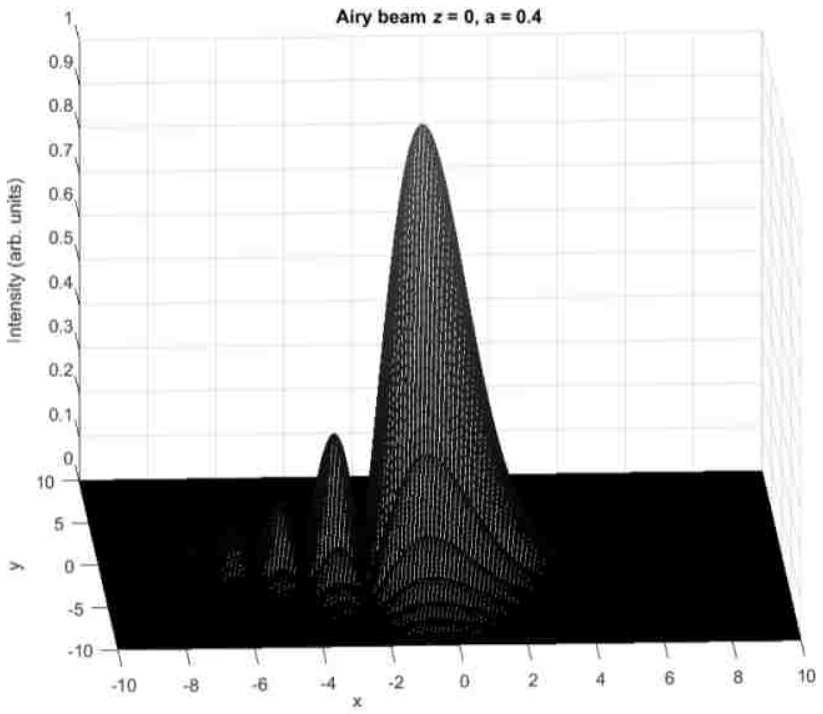

Figure 3.2: Airy beam intensity for $a = 0.4$ near its beam waist.

truncation of the Airy beam for $x < 0$. Then, the form of the initial field in the plane at $z = 0$, is

$$\psi(\tilde{x}, 0) = \mathrm{Ai}(\tilde{x}) \exp(a\tilde{x}), \tag{3.8}$$

with truncation term $\exp(a\tilde{x})$ where $0 \leq a < 1$ and constant. Though a is not mathematically bounded by 1, the truncation factor beyond this least upper bound affects the shape of the function to a negligible degree. That is, only a single peak is obtained at $a \approx 1$. Note that if we let $a = 0$, we retain the infinite energy Airy beam.

The Fourier transform of the Airy beam at $z = 0$ (at the beam waist) is given by,

$$\tilde{\psi}(k) = \int_{-\infty}^{\infty} \psi(\tilde{x}, 0) \exp(ik\tilde{x})\, d\tilde{x} \tag{3.9}$$

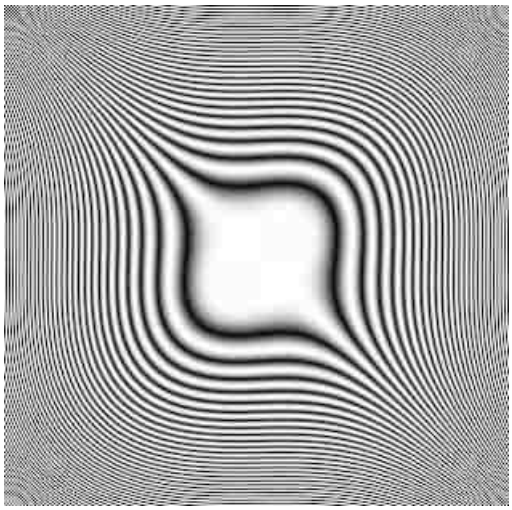

Figure 3.3: Fourier transform of a truncated, or finite, Airy beam with $a = 0.4$ near its beam waist.

where $k = k_x x_0$. Using to (3.9) in (3.10) we get.

$$\begin{aligned}\tilde{\psi}(k) &= \int_{-\infty}^{\infty} \mathrm{Ai}(\tilde{x}) \exp(a\tilde{x}) \exp(ik\tilde{x}\,) d\tilde{x} \\ &= C \exp[\frac{1}{3}(a+ik)^3] \\ &= C \exp\left[-ak^2\right] \exp\left[\left(\frac{a^3}{3} + ia^2k - ak^2 - i\frac{k^3}{3}\right)\right] \end{aligned} \tag{3.10}$$

where the constant $C = 1/2\sqrt{2\pi}$. Equation (3.11) shows the Fourier transform of the Airy beam in two dimensions. From this two dimensional Fourier transform, we see that cubic phase is present. Then, a cubic phase profile can be calculated and uploaded onto a spatial light modulator (SLM to be discussed later in the Experiment section of this Chapter) in an array structure and used for phase modulation. The accompanying phase is presented in Figure (3.3) showing an example of the Fourier transform for a nonzero a, $a = 0.4$.

Now that the initial Airy beam, Equation (3.9), has been specified, its propagation from the $\tilde{z} = 0$ plane to arbitrary z must be determined. This is done by using Equation

(3.9) and integrating via a Fresnel transform from the $(\tilde{x}, \tilde{y}, \tilde{z} = 0)$ plane to the $(\tilde{x}', \tilde{y}', \tilde{z})$ plane. The integral transform is known as the Hyugen-Fresnel intergral for paraxial waves. And, it takes the following form in one dimension [26, 27]

$$\begin{aligned}\psi(\tilde{x}', \tilde{z}) &= \sqrt{\frac{i}{2\pi\tilde{z}}} \int_{-\infty}^{\infty} d\tilde{x}\ \psi(\tilde{x}, 0) \exp\left[\frac{i}{2\tilde{z}}(\tilde{x} - \tilde{x}')^2\right] \\ &= \sqrt{\frac{i}{2\pi\tilde{z}}} \int_{-\infty}^{\infty} d\tilde{x}\, (\mathrm{Ai}(\tilde{x}) e^{a\tilde{x}}) \exp\left[\frac{i}{2\tilde{z}}(\tilde{x} - \tilde{x}')^2\right] \end{aligned} \tag{3.11}$$

Expanding the quadratic term in the exponential in Equation (3.12) and by completing the square we get

$$\begin{aligned}&\psi(\tilde{x}', \tilde{z}) = \sqrt{\frac{i}{2\pi\tilde{z}}} \int_{-\infty}^{\infty} d\tilde{x}\ \mathrm{Ai}(\tilde{x}) \exp\left[\frac{i}{2\tilde{z}}\left(\tilde{x}^2 + \tilde{x}'^2 - 2\tilde{x}\tilde{x}' - i2\tilde{z}a\tilde{x}\right)\right] \\ &= \sqrt{\frac{i}{2\pi\tilde{z}}} \int_{-\infty}^{\infty} d\tilde{x}\ \mathrm{Ai}(\tilde{x}) \exp\left[\frac{i}{2\tilde{z}}\left(\tilde{x}^2 - 2\tilde{x}(\tilde{x}' + ia\tilde{z}) + (\tilde{x} + ia\tilde{z})^2 - (\tilde{x} + ia\tilde{z})^2 + \tilde{x}'^2\right)\right] \\ &= \sqrt{\frac{i}{2\pi\tilde{z}}} \exp\left[\frac{i}{2\tilde{z}}((a\tilde{z})^2 - i2\tilde{x}'a\tilde{z}))\right] \left[\int_{-\infty}^{\infty} d\tilde{x}\ \mathrm{Ai}(\tilde{x}) \exp\left[\frac{i}{2\tilde{z}}\left(\tilde{x} - (\tilde{x}' + ia\tilde{z})\right)^2\right]\right] \end{aligned} \tag{3.12}$$

To make evaluation of Equation (3.13) more convenient, let

$$\int_{-\infty}^{\infty} dx\, \mathrm{Ai}(\tilde{x}) e^{\frac{i}{2\tilde{z}}(\tilde{x} - (\tilde{x}' + ia\tilde{z}))^2} = \int_{-\infty}^{\infty} ds\, \mathrm{Ai}(s) e^{iA(s-p)^2} \tag{3.13}$$

We carry out the evaluation of Equation (3.13)

$$\int_{-\infty}^{\infty} \mathrm{Ai}(s) e^{iA(s-p)^2}\, ds = \int_{-\infty}^{\infty} ds \left\{ \frac{1}{2\pi} \int_{-\infty}^{\infty} e^{(i(st+t^3/3))}\, dt \right\} e^{(iA(s-p)^2)}$$

$$= \frac{1}{2\pi} \int_{-\infty}^{\infty} dt\, e^{it^3/3} \left[e^{iA(-p^2-t^2/4A^2+2pt/2A+p^2)} \right] \int_{-\infty}^{\infty} ds\, e^{iA(s-(p-t/2A))^2}$$

$$= \frac{1}{2\sqrt{i\pi A}} \int_{-\infty}^{\infty} dt\, e^{i/3(t^3-3t^2/4A+3t(1/4A)^2-(1/4A)^3-3t(1/4A)^2+(1/4A)^3+3pt)}$$

$$= \frac{1}{2\sqrt{i\pi A}} \int_{-\infty}^{\infty} dt\, e^{i/3(t-1/4A)^2+i(t-1/4A)(p-(1/4A)^2)} e^{i(p/4A)-i(1/4A)^3+i/3(1/4A)^3}$$

$$= \frac{1}{2\sqrt{i\pi A}} (2\pi) \mathrm{Ai}(p-(1/4A)^2) e^{i(p/4A)-i2/3(1/4A)^3}$$

$$= \sqrt{\frac{\pi}{iA}} \mathrm{Ai}(p-(1/4A)^2) e^{i(p/4A)-i2/3(1/4A)^3} \tag{3.14}$$

In Equation (3.14), the Gaussian integral was evaluated in standard form, and the definition of the Airy Equation (3.6) was used. Replacing p, s and $A = 1/2\tilde{z}$, Equation (3.14) results in the more familiar form [26]

$$\psi(\tilde{x}', \tilde{z}) = \sqrt{\frac{2\pi\tilde{z}}{i}} \mathrm{Ai}(\tilde{x}' \pm ia\tilde{z} - (\tilde{z}/2)^2) e^{i\tilde{x}'z/2 \pm a\tilde{z}^2/2 - i\tilde{z}^3/12}. \tag{3.15}$$

From Equation (3.15), our solution is now

$$\psi(\tilde{x}', \tilde{z}) = \sqrt{\frac{i}{2\pi\tilde{z}}} \sqrt{\frac{2\pi\tilde{z}}{i}} \mathrm{Ai}(\tilde{x}' + ia\tilde{z} - (\tilde{z}/2)^2) \exp\left[i\frac{\tilde{x}'\tilde{z}}{2} - a\frac{\tilde{z}^2}{2} - i\frac{\tilde{z}^3}{12} + i\frac{a^2\tilde{z}}{2} + \tilde{x}a \right]$$

$$= \mathrm{Ai}\left(\tilde{x}' + ia\tilde{z} - \left(\frac{\tilde{z}}{2}\right)^2 \right) \exp\left[a\left(\tilde{x}' - \frac{\tilde{z}^2}{2} \right) + i\left(\frac{\tilde{x}'\tilde{z}}{2} + \frac{a^2\tilde{z}}{2} - \frac{\tilde{z}^3}{12} \right) \right]. \tag{3.16}$$

Equation (3.16) is the expression for the scalar amplitude of the Airy beam for propagation along the z direction with only the $\tilde{x}$ dependence. An identical expression can be written with $\tilde{y}$ in place of $\tilde{x}$ and multiplied by the $\tilde{x}$-expression to obtain the complete scalar

transverse amplitude. We may write the final expression for the Airy beam amplitude as

$$\psi(\tilde{x}', \tilde{y}', \tilde{z}) = \mathrm{Ai}\left(\tilde{x}' + ia\tilde{z} - \left(\frac{\tilde{z}}{2}\right)^2\right) \exp\left(a\left(\tilde{x}' - \frac{\tilde{z}^2}{2}\right) + i\left(\frac{\tilde{x}'\tilde{z}}{2} + \frac{a^2\tilde{z}}{2} - \frac{\tilde{z}^3}{12}\right)\right)$$
$$\times \mathrm{Ai}\left(\tilde{y}' + ia\tilde{z} - \left(\frac{\tilde{z}}{2}\right)^2\right) \exp\left(a\left(\tilde{y}' - \frac{\tilde{z}^2}{2}\right) + i\left(\frac{\tilde{y}'\tilde{z}}{2} + \frac{a^2\tilde{z}}{2} - \frac{\tilde{z}^3}{12}\right)\right). \quad (3.17)$$

For an expression for the intensity, the square modulus must be taken of Equation (3.17). Also, with this two dimensional Airy scalar amplitude, Maxwell field solutions for the three orthogonal polarization components may be determined using Equations (1.30)-(1.32).

3.2 Airy beam properties

Properties of the dominant component are observed in the cross component, too. Some of the striking features, or properties, of the beam are self-healing, tight focusing, and peculiarly, the non linear trajectory along the beam propagation direction $\hat{z}$. In this context, it is of interest to observe that most non-diffracting beams, such as Bessel, Helmholtz, Hermite-Gauss, etc., are self-healing [16].

This self-healing is defined in terms of the behavior of the beam when the beam is physically obstructed in a plane at some z and observed at a later z' plane. At z, the obstructed portion of the light is, of course blocked completely. After the plane at z, the beam continues to propagate in the original direction, but new, z dependent wave vector components in the transverse direction are added to the remaining part of the wave leaving that obstruction. These additional, transverse vector components redirect the energy in the beam to the lost portion of the beam rebuilding the beam, or healing the beam.

Many of the non-diffracting beams exhibit this property and the Airy beam is no exception and neither is the cross component of the Airy beam [28]. In order to see how the traffic of the energy in the beam is redirected, an analysis of the Poynting vector for the field is needed. Then, in removing a portion of the beam at z, one can predict, using the Poynting vector, where the energy will be moving in the transverse plane.

Another distinguishing property of Airy beams is a non linear, parabolic trajectory. Starting at the beginning, $z = 0$, the beam immediately begins to shift in the transverse direction. And, as a function of z, the shift is parabolic. Though the trajectory is non linear, the beam is not actually accelerating. There is no net change in momentum of the field since the average position in the transverse direction of the field shifts at a constant rate [24].

Many studies, experimental, numerical, and analytical, have been done on the peculiar directionality the Airy beam exhibits during its propagation. Experimentally, Siviloglou et al, the first group to report the beam's observation, showed evidence of the parabolic trajectory of the Airy beam as a function of propagation. This propagation is attributed to the quadratic term in the scalar field expression of the Airy beam [29].

$$x_d \approx \frac{\lambda^2 z^2}{16\pi^2 x_0^3} \tag{3.18}$$

Here, x_d is defined as the deflection distance as a function of z propagation distance from some origin $z = 0$, λ is the wavelength of the beam, and x_0 is the x-direction scaling parameter. The deflection distance is derived from the single transverse dimensional case. This property of the Airy is a rather fundamental one and the same group, among others who have described the Airy beam dynamics to varying degrees, discussed the Airy beam

dynamics in more analytic detail. Since the trajectory is parabolic, it is possible to have various transformations of resulting in another parabolic path. That is, by some simple translation or rotation or affine transformation, the basic shape of the parabola remains from the similarity transformation mentioned.

In the discussion, it is assumed that the Airy beam is truncated one where the original field for the beam has a factor of $\exp(as)$, where $0 < a < 1$ is the so-called truncation factor and s is a dimension in the transverse field for the beam. Also included is an additional factor, $exp(ivs)$, where v is the constant "velocity" of the Airy beam. Since the Airy beam trajectory is parabolic, the dynamics can then be related, or compared, to two dimensional, classical projectile motion. Then, the "velocity" can be thought of as the initial vertical component of the initial velocity. The scalar field for the Airy beam has the following expression.

$$\phi(s,\xi) = Ai[s - (\xi/2)^2 - v\xi + ia\xi] \exp[as - (a\xi^2/2) - av\xi]$$
$$\exp[i(-(\xi^3/12) + ((a^2 - v^2 + s)\xi/2) + vs - (v\xi^2/2))] \tag{3.19}$$

In Equation (3.19), the term describing the trajectory of interest is $s = (\xi/2)^2 + v\xi$. In comparison with Equation (3.18) and s from Equation (3.19), we have an expression that includes a term that takes into account an initial "launch" angle for the Airy beam [29],

$$x_d = \theta z + \left(\frac{z^2}{(4k^2x_0^3)}\right) \tag{3.20}$$

The angle, θ, is the initial angle due to the initial, constant "velocity", v. The kinematics

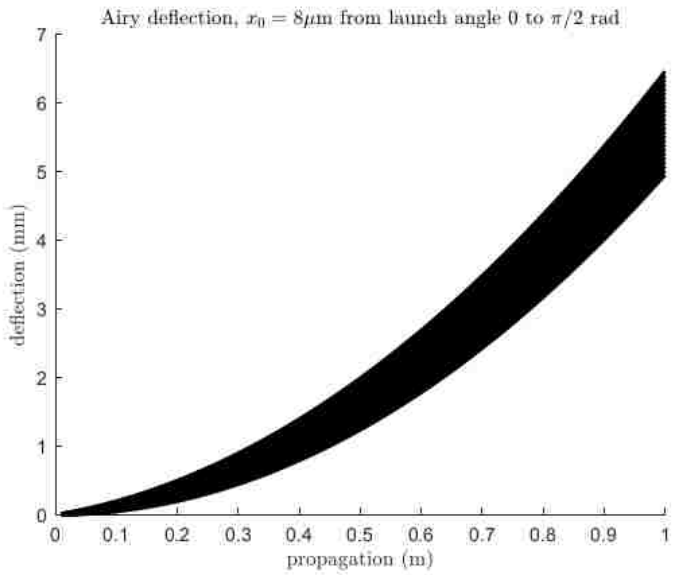

Figure 3.4: The effect, shown above, of how the parabolic trajectory is evident as the launch angle is varied with a constant, initial "velocity". The shaded area in the graph is the range deflections controlled by launch angle, θ, which varied from 0 rad (lower boundary) to $\pi/2$ rad (upper boundary) is increments of $\pi/50$ rad. It is evident that deflection increases as the launch angle increases.

for the path of the beam is then similar to

$$x_{disp} = v_{x,0}t + \left(\frac{z^2}{sk^2x_0^3}\right), \tag{3.21}$$

where x_{disp} is the horizontal displacement, $t \to z$ for time, $v_{x,0} \to \theta$ as the initial horizontal velocity, and $a/2 \to 1/4k^2x_0^3$ as the acceleration.

In Figure (3.5), the deflection of the Airy beam and the effect of several launch angles is shown for a beam with $x_0 = 8$ μm from $\theta = 0$ to $\pi/2$ rad in steps of $\pi/50$ rad. In maintaining that momentum is conserved for this beam, an analogy can be made between the center of gravity of this beam and that for a system of particle(s). Taking advantage of this idea, the center of gravity is the center of this wave packet allows for determining the average transverse position, or the first momentum of the square modulus, of the wave

packet as [29]

$$\langle x(\xi)\rangle = \left(\frac{1}{N}\right)\int_{-\infty}^{\infty} s|\psi(s,\xi)|^2 ds. \tag{3.22}$$

In Equation (3.22), ψ is the field amplitude, x the transverse position, z the propagation position, and $N = \int |\psi|^2 ds = (8\pi a)^{-1/2}\exp(2a^3/3)$. With Equation (3.22) and Ehrenfest's theorem, $m(d\langle s\rangle/d\xi) = \langle p\rangle$, can be applied to give an expression for the "center of gravity" as [29]

$$x(t) = vt + \frac{1}{2}\frac{dv}{dt}t^2 \tag{3.23}$$

Then, Equation (3.23) shows that the average transverse position changes linearly with ξ, conserving momentum.

3.2.1 Finite Airy beam

Another property of a realistic Airy beam mentioned in the last section is that its power is finite. A truncation factor, a, was included for a realistic description for the Airy beam. Without that factor, the square modulus of the Airy function extends to $-\infty$ which would mean an infinite amount of energy for the beam. This factor, that ranges from 0 to 1, is a controllable, dimensionless, free parameter. The effect of truncation is shown in Figure (3.4) for both the dominant and cross components.

When a approaches 0, the finite Airy beam profile approaches that of the infinite Airy beam. In the opposite limit, as a approaches 1, the extent of the Airy beam decreases rapidly. The number of peaks will decrease to a single peak. The parameter a may be allowed to have values above 1, but the end result of arbitrarily large truncations are the

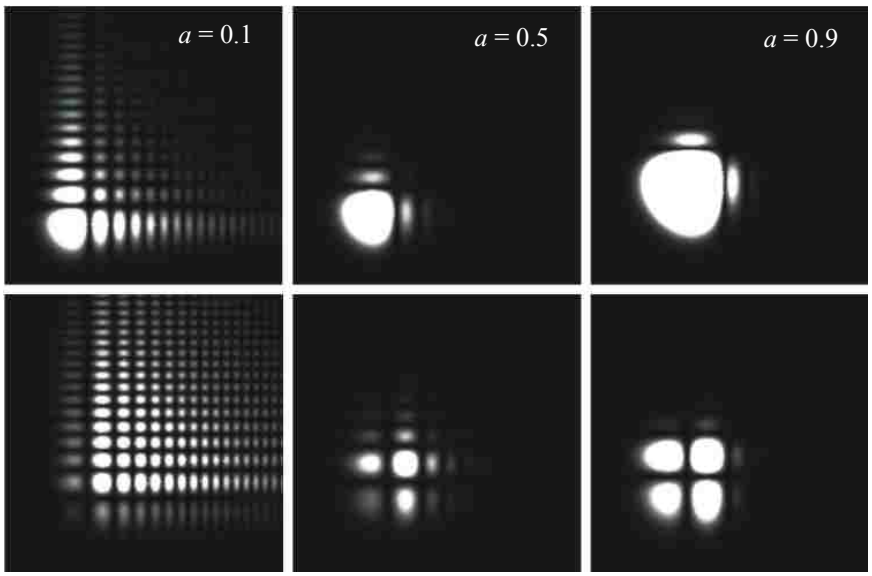

Figure 3.5: Theoretical plots of the dominant (top row) and cross (bottom row) intensities for varying truncation a at the beam waist. Number of peaks increases roughly 3-4 times from dominant to cross component distributions and the effect of the increase in the truncation factor decreases the overall number of peaks as expected.

same; a single peak as obtained for a Gaussian, but an asymmetric one. It does have bilateral symmetry between the vertical and horizontal directions in its transverse plane, but no radial symmetry as with the fundamental Gaussian mode.

3.2.2 Airy beam polarization

The cross polarization components of a linearly polarized beam, (dominantly linearly polarized beam) are given by Equations (1.30)-(1.32). For the Airy beam, the solution (3.18) may be used to obtain expressions for the two transverse field components and the longitudinal one.

For the dominant component, Equation (1.30) is implemented in the form

$$E_x = \psi(\tilde{x}, \tilde{y}, \tilde{z}). \tag{3.24}$$

Then, the dominant component is specified directly. The amplitude of the cross component, $E_{\tilde{y}}$, has the form

$$E_y = \frac{1}{2k^2x_0^2}\frac{\partial^2\psi(\tilde{x},\tilde{z})}{\partial\tilde{x}\partial\tilde{y}}. \tag{3.25}$$

And, in order to compare experimental observations of the Airy beam to field amplitude Equations (3.24) and (3.25), the square modulus of the fields are found from [11]

$$\begin{aligned} I_x \propto |E_x|^2 &= |\mathrm{Ai}(\tilde{x}+ia\tilde{z}-(\tilde{z}/2)^2)|^2|\mathrm{Ai}(\tilde{y}+ia\tilde{z}-(\tilde{z}/2)^2)|^2 \\ &\quad\times\exp(a(2\tilde{x}+2\tilde{y}-\tilde{z})) \end{aligned} \tag{3.26}$$

$$\begin{aligned} I_y \propto |E_y|^2 &= \frac{1}{4k^4x_0^4}\exp(a(2\tilde{x}+2\tilde{y}-\tilde{z})) \\ &\quad\times\left|\left(a+i\tilde{z}/2+\frac{\partial}{\partial\tilde{x}}\right)\mathrm{Ai}(\tilde{x}+ia\tilde{z}-(\tilde{z}/2)^2)\right|^2 \\ &\quad\times\left|\left(a+i\tilde{z}/2+\frac{\partial}{\partial\tilde{y}}\right)\mathrm{Ai}(\tilde{y}+ia\tilde{z}-(\tilde{z}/2)^2)\right|^2. \end{aligned} \tag{3.27}$$

In Equation (3.26), there is not much for surprise in the expected intensity for the dominant component. That is, the field is only multiplied by itself. However, in Equation (3.27), the interesting part comes from the partial derivatives of Equation (3.26) which are seen to be carried through into (3.27). In the expression for the intensity Equation (3.27) for the cross polarization component, the order of the derivatives do not affect the final result.

3.3 Airy beam Generation and Application

With all the interesting properties of Airy beams, multiple methods have been developed to generate these types of beams not only (as their truncated versions but also in several

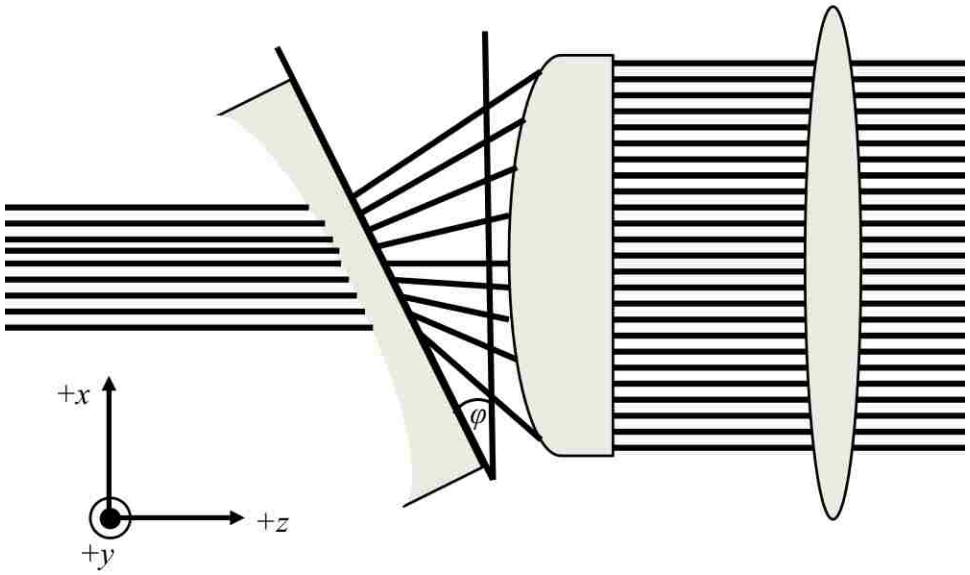

Figure 3.6: Figure (3.6) shows the lens method for producing 1D Airy beams. A collimated Gaussian beam enters from the left and passes through a concave cylindrical lens, then a convex cylindrical lens, and finally, a double convex lens for a Fourier transform. The tilt of the first lens is at angle ϕ with respect to the $+x$ axis where the $+z$ is the propagation direction.

other varieties such as stretched or oblique Airy beams [30], arrays) of Airy beams [31], pulsed Airy beams [32], evanescent Airy beams [33], etc.

Most popular method, due to its ease of programming is the phase modulation method using a spatial light modulator (SLM). The specifics of the SLM will be discussed later in the Experiment section of this chapter. Other methods, in general, use non-linear materials for phase modulation, and the same phase can also be achieved via lens. In all of the methods discussed here, it all amounts to following the Fourier prescription of forcing a cubic phase to the fundamental Gaussian and transforming that into the Airy beam. The lens method is implemented by starting with an expanded Gaussian beam as the input for a concave cylindrical lens that is tilted by angle ϕ as shown in Figure (3.6). After the light

passes through the concave lens, a second cylindrical convex lens is used with its angle $\phi = 0$. Both lenses are aligned with matching curvature and long axes parallel. The ϕ angle of tilt imparts a cubic phase to the Gaussian beam [34]. After the light passes through both lenses, a final lens is used to perform a Fourier transform on the cubic phase modulated beam. Then, a one dimensional Airy beam is produced. For the two dimensional case, two sets of cylindrical lenses perpendicular to each other are used in succession. One cylindrical lens is orientated with its long axis along the horizontal and the second lens along the vertical so that there the axes of the lenses are perpendicular to each other. Papazoglou, et al [34] demonstrates this procedure using a concave lens and a cylindrical lens right after. The difference in this procedure is that since two transformations are to be performed on the beam, the simple, single lens approach won't suffice and it is advantageous to use the concave lenses to keep the wavefront of the beam collimated, or parallel, allowing for simpler phase modulation.

Another method that has been used to generate Airy beams uses non-linear optical materials. Ellenbogen, et al, [35] use an interesting method of three-wave mixing (TWM) to generate an Airy beam. The material used in the process is of second order, $\chi^{(2)}$, lithium tantalate, and is made with an asymmetric poled structure. The spatial frequencies in the crystal are binary and linear along the beam propagation direction. The frequency in the transverse direction in the crystal is cubic. A pump beam is used to induce first and second harmonic generation of waves. Quasi phase matching conditions force the momentum wave vectors between first and second harmonic polarization to diminish with the beam propagation. The additional feature here is that the lithium tantalate $\chi^{(2)}$ structure induces a cubic phase which now dominates over the diminishing

waves. The output wave with the dominating cubic phase is the transformed into the Airy beam via lens as a Fourier transform. The more novel aspect of this experiment shows that smaller, more compact systems can be constructed to generate Airy beams. Such is the example of an Airy beam produced from a microchip as proposed by Longhi, et al [36].

Lastly, the same idea of phase modulation is done often using spatial light modulators. Porat et al, [37] achieve the generation of Airy beams by preparing image files that encode the phase of the beam and uploading them to the LCD screen of the SLM. Then, a Gaussian beam is reflected off of the LCD pattern where the beam now has the added cubic phase. The beam is passed through a lens and the Airy beam produced at the secondary focal plane of that lens. This is the approach used in this work to generate Airy and Ince-Gauss beams. This method will be discussed in more detail in the Experiment chapter.

There are other interesting manipulations of Airy beams that have been realized theoretically and experimentally, and presented here are a few of those derivative generations of Airy beams.

One example of further engineering is the proposal of a dual Airy beam by Hwang, et al [31]. The dual Airy beam is created by crossing their paths resulting in what was named the quad Airy beam. By controlling the initial launch angles and positions of two Airy beams (1D or 2D) and intersect as they propagate. The novelty, or appeal, for this proposal is that it creates a symmetric array of peaks that may be uesd for optical trapping and the self healing of the Airy beam is an added benefit. In fact, their study has shown that the self healing improves the dual Airy beam over the standard, finite case. Also, the dual or quad Airy beams have the capability of being controlled simultaneously,

which is to be expected since each beam can be controlled individually anyway. However, the shape and self healing prove useful in trapping applications.

Another investigation has shown that a potential function in the PWE for the Airy beam can be predefined along a propagation to directly control the trajectory of the Airy beam assuming that it may be in a material in which a gradient index can be applied [38]. It is an interesting study showing that the overall phase of the Airy beam is determined by a polynomial function for which its coefficients may be found for the desired path of the caustic, or maximum amplitude of the Airy beam. Types of paths demonstrated are the power law, exponential, logarithmic, and sinusoidal. One possible limitation is the discontinuity in the potential functions defined for which, the Heaviside function, as the derivative of the dirac delta function, may be utilized to characterize the gradient index.

Airy beams can be modified not only in their superposition or direction but also their appearance individually as skewed or stretched with respect to a Cartesian coordinate system. This is the case in what are called oblique Airy wave packets. The oblique part of the beam originates from the obliquity, a parameter angle characterizing the amount of skew or stretch. Such studies are of interest for producing Airy beam pulses, or wave packets, that are engineered spatially and temporally.

3.4 Experiment

In the following experiment, the main objective was to measure the irradiance of the cross polarization component of a dominantly, linearly polarized Airy beam for varying values of truncation parameter and propagation distances from the waist. There are two main parts

to the experiment which are the generation of the Airy beams and measuring the intensity profiles of their polarization. First, an outline of the procedure is given with an explanation of the generation via the spatial light modulator (SLM). Then, the measurement part of the procedure is discussed.

3.4.1 Outline

A HeNe laser of wavelength 632 nm was used to direct a Gaussian beam a SLM. The SLM was a reflective type which modulated the phase of the incident beam. The reflected, modulated beam was passed through a lens to perform a Fourier transform to produce an Airy beam at approximately $2f$ away from the SLM device.

At $2f$, where we presume $\tilde{z} = 0$, a charged coupled device (CCD) camera was placed to record the irradiance of the dominant and cross polarization components of the Airy beam. Just before $\tilde{z} = 0$, a pair of linear polarizers was placed in tandem to control the polarization of the beam at the CCD.

3.4.2 Spatial Light Modulator (SLM)

Background and Operation

The SLM, is a phase modulation device that is controlled via a computer and digital visual interface (DVI) controller. The device itself includes the DVI controller box, LCD array for the modulation, and software for control. Figure (3.7) shows a picture of the device from Boulder Non linear Systems company (BNS). A summary of the specifications for the SLM model used may be found in Appendix B.1. The main feature of the device is that the DVI controller connecting the computer and the SLM allows for pixel by pixel voltage

Figure 3.7: A photograph of the BNS phase-only spatial light modulator (SLM) from the BNS user manual. A device used to modulate the phase of incoming light which is then reflected.

control across the whole LCD array. This control enables direct manipulation of the refractive index, and hence, phase modulation for each pixel over a range of approximately 0 to 2π.

The LCD array area is 7.68 x 7.68 mm^2 with 512 x 512 pixels. Each 15 x 15 $microns^2$ area pixel has stacks of organic molecules which are allowed to rotate in planes parallel to the LCD surface. Each pixel may be controlled to rotate through an angle by applying a voltage across the pixel. Figure (3.8) below shows the layers of the LCD array on the SLM where the light is incident from the top of the page and reflected to the top of the page from the dielectric mirror.

In Figure (3.8), there are three main layers: coverglass with InO conducting film, rod like organic molecules, and the mirror, also coated with the conductive film. The voltage applied is across the conductive films. The stack molecules will then rotate

Figure (3.8) shows the stack of molecules that rotates parallel to the LCD surface. The

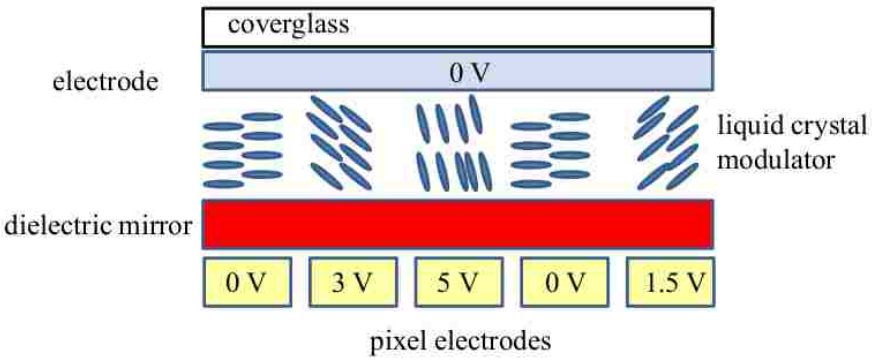

Figure 3.8: Diagram showing the different layers in the operation of the SLM phase modulation. From the top, incoming wave enters the coverglass and passes the electrode. The wave passes through the liquid crystals which are rotated to a fixed position determined by the voltage between the top electrode and each individual pixel electrode. The diagram shows the variation of the crystal rotation as the voltage is increased from 0 volts. The wave is reflected from the dielectric mirror and passes again through the entire cell out the coverglass now with a pixel by pixel phase modulated wavefront.

cartoon shows rotation in a plane parallel to the page perpendicular to the actual rotation plane only to illustrate the effect of the voltage difference between the electrode layer and the pixel electrodes layer. From this, the index of refraction for that pixel in the array will change to some desired value.

With this ability of being able to control every pixel, a beam incident on the array can be modulated in phase across the surface. An important detail is that the polarization of the incident beam, to be properly modulated with most efficiency of conversion, must be dominantly polarized vertically with respect to the orientation of the SLM.

In this sense, the LCD array is akin to a dynamically controlled wave plate so that the fast axis of the LCD molecules may twist allowing for a phase difference of $\phi = 2n\Delta d$, where n is the refractive index at some pixel, and Δd is the thickness of the LCD array. The factor of 2 takes into account the double passage through the layers. Ignoring the 2 mm coverglass, the thickness of the LCD array is approximately 1 micron.

There are other types of SLM devices that also modulate the amplitude which are ferroelectric LCDs. Combinations of phase and amplitude modulation are available and consist of both types of LCDs. The type of SLM used was for phase modulation only. The LCD is of a nematic type. In order to control the modulation of the SLM, a bitmap image file is created of the desired phase profile. The image file the color index of each pixel determines the amount of voltage to apply to each LCD pixel for phase modulation.

Two programs were used that were both supplied by the manufacturer, MeadowLark. One program was a Matlab Script interface and the other is a GUI interface developed by BNS, originally.

The Matlab script was used most often. A copy of the script "DVI_Matlab_GUI.m" is reproduced in the Appendix A.1.

Operation of the SLM is convenient in that one needs only to run the software and upload pre-programmed bitmaps that represent the desired phase modulation. The image files may be created by any method. The phase profiles must be a 512 x 512 array, bitmap file type, and the pixel value (by color) to be in an RGB mode as opposed to color index mapping so that the total array dimension is 512 x 512 x 3. Each phase profile created is a $512 \times 512 \times 3$ array as a windows bitmap. The extra 3 for the array dimension corresponds to the "RGB" values.

Once a bitmap image is selected in the 512×512 and RGB format, the SLM Matlab program reads the colors and codes them into 16 bit strings of numbers. The binary strings are converted, using a lookup table, provided by the software, to voltages to be applied across the LCD array in the SLM. The manufacturer measures the LCD phase modulation for the designed wavelength(s) and then creates the lookup table for accurate

conversion of binary strings to phase modulation as supplied by the manufacturer. The pitch of the phase modulation is approximately 2π or one full wave.

3.4.3 Airy beam production

For the Airy beam, phase profiles computed were according to [37]

$$\phi(x,y) = \frac{2\pi x}{\Lambda} + \frac{x^3 + y^3}{R^3}. \tag{3.28}$$

Equation (3.28) is the cubic phase from equation (3.11) in two dimensions where x and y coordinates correspond to the SLM pixel locations. An example of the phase profile is shown below in Figure (3.9).

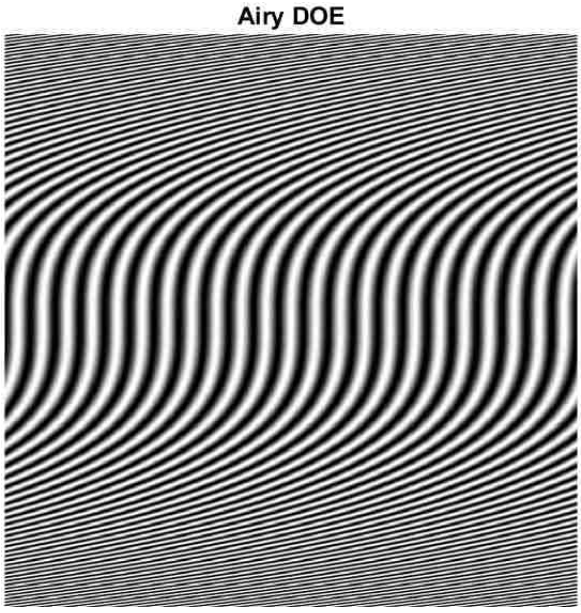

Figure 3.9: Example of the phase mask, or diffractive optical element (DOE), from Equation (3.28) for the SLM for Airy beam production.

A blazed cubic phase grating, given by

$$\phi(x,y) = \frac{2\pi x}{\Lambda} + \frac{x^3 + y^3}{R^3}, mod(\pi), \tag{3.29}$$

corresponding to the Airy beam phase, was written on the SLM to modulate the incident Gaussian beam.

The main difference between Equations (3.28) and (3.29) is that the phase profile is modulated by π. This modulation causes the grating to become blazed. A blazed grating is a diffraction grating that diffracts light such that the first order diffraction location has the dominant intensity leaving other orders significantly weaker in intensity. It should be noted that in this experiment only a π phase modulation across the phase mask was used as indicated by Equation (3.29). The appearance of the mask, therefore, changes as shown in Figure (3.10) below. This π phase modulation ensured that the diffraction has highest intensity in the first order.

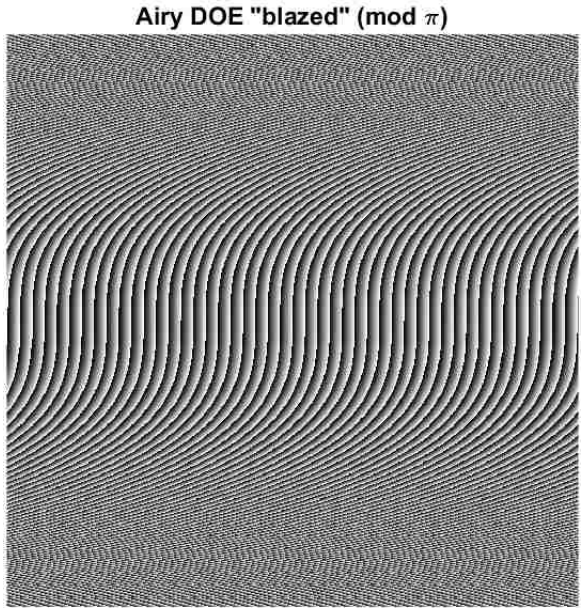

Figure 3.10: Similar to the DOE of Figure (3.9), this DOE has a phase modulation of π in order to blaze this DOE and produce highest diffraction efficiency in the first order.

In Equations (3.28) and (3.29), Λ is the grating period, R is a parameter controlling the curvature of the cubic phase modulation, and x and y are the coordinates of a pixel on the LCD array. Increasing R decreases the cubic modulation and yields Airy beams with a

close to 1, whereas decreasing R increases the modulation yielding Airy beams with a close to 0. The grating period was kept fixed to ensure that the first order diffraction was reflected from the SLM by approximately the same angle for different R values which correspond to different a values used in this experiment. A Matlab script for producing the Airy beam phase mask may be found in the Appendix A.2.

When using the SLM, the incident beam may be directed normal to the LCD surface using a beam splitter or at a small angle to the normal without a beam splitter.

At an angle, there is potentially an issue concerning cross talk between adjacent pixels where light from entering one pixel may end up partially traveling into adjacent pixels. The cross talk has not been a significant issue as long as the angle is kept small. Angles above $15 - 20°$ begin to show cross talk or modulation deviating from the manufacturer modulation at normal incidence.

In this experiment direct incidence at a small angle was chosen in order to avoid large loss of laser power.

3.4.4 Procedure

The properties of the parabolic trajectory of the Airy beam effect of the truncation of the beam, and observation of the cross polarization were the foci of this experiment. As the beam exhibits a parabolic trajectory as a function of the propagation distance, z. The decay, or truncation, parameter decreases the spatial extent of the beam with a ranging from 0 to 1. Finally, as shown in this Chapter, the cross polarization of the Airy beam is expected to follow trends and peak splittings observed for HG, LG, and the fundamental beams.

Figure (3.11) shows an outline of the experimental setup.

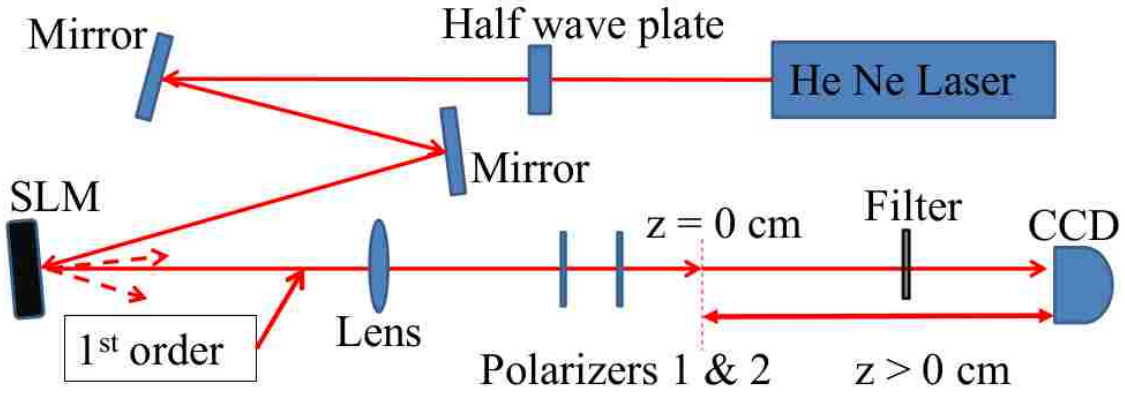

Figure 3.11: Experimental setup for the Airy beam cross polarization observation.

A linearly polarized 50 mW 633-nm He-Ne laser beam of nominally 2 mm diameter was incident on a BNS 512 phase only spatial light modulator (SLM). The LCD array of the SLM has dimensions of 7.68 mm $\times$ 7.68 mm with pixel size of 15 μm $\times$ 15 μm. A half wave plate was used to adjust the incident beam polarization to match the polarization required by the SLM for optimum phase modulation. As mentioned in the Airy phase modulation, a Gaussian beam was reflected from the SLM and diffracted into multiple orders from the blazed Airy grating. The first order diffracted beam from the SLM was passed through a lens placed one focal length ($f = 50$ cm) away from the SLM. The Airy beam was produced in the back focal plane of the lens at a distance of $2f$ from the SLM. The back focal plane of the lens defined the plane $z = 0 = \tilde{z}$. A CCD camera (Spiricon 480M) recorded the intensity profiles of the polarization components at different distances z for $a = 0.11, 0.22,$ and 0.97. The intensity profiles of the dominant polarization component were recorded with the transmission axes of both linear polarizers (Meadowlark Optics) aligned with the dominant polarization direction. To measure the cross-polarization intensity profile the second polarizer was oriented such that its transmission axis was crossed relative to the

first. The extinction ratio of the polarizers in the experiment was 10^5.

The trajectory of the dominant polarization component of the Airy beam was measured relative to the trajectory of a first order Laguerre-Gauss (LG) beam produced by the same method as the Airy beam but with a forked grating phase mask with $\ell = 1$. As the LG beam propagates along a straight line trajectory, it was used as the reference for measuring the Airy beam trajectory. The first order LG beam was chosen over the zeroth order Gaussian because all phase masks used were blazed and the Airy beam and Gaussian could not be recorded at the propagation distance without translating the CCD in the transverse direction.

Airy beam Trajectory

In characterizing the Airy beams produced, its trajectory was measured to establish that the beams studied were in fact Airy beams.

Experimentally recorded intensity profiles of the dominant and cross polarization components were compared to those obtained from Equations (3.26) and (3.27). This required a determination of the aperture and scaling parameters a and x_0. These were determined by fitting line profiles of the DP component intensity to the curve obtained from (3.27) for $\tilde{z} = 0$. In order to determine x_0, the transverse displacement of the central peak of the Airy beam was measured relative to the center of a first order LG beam. The first order Airy beam appeared in a slightly different direction α relative to the first order LG beam. The deflection of the Airy beam was calculated by

$$r_d = r_{rel} + \sqrt{2}\,\alpha\, z_{slm}\,, \tag{3.30}$$

where r_{rel} is the distance between the dominant corner peak of the Airy beam and center of the LG beam, z_{slm} is the distance from the SLM to the plane of observation, and α is the angle between the LG and Airy beams in the first order of diffraction. The factor of $\sqrt{2}$ accounts for the fact that the calculated trajectory is two dimensional in the plane transverse to the propagation direction. Figures (3.13) shows the measured values of r_d along with the parabolic curve (12) for the Airy beam for three different values of aperture parameter a. The two appear to be in good agreement in all cases. Figure (3.12) demonstrates how the Airy beam path orientated relative to the LG beam.

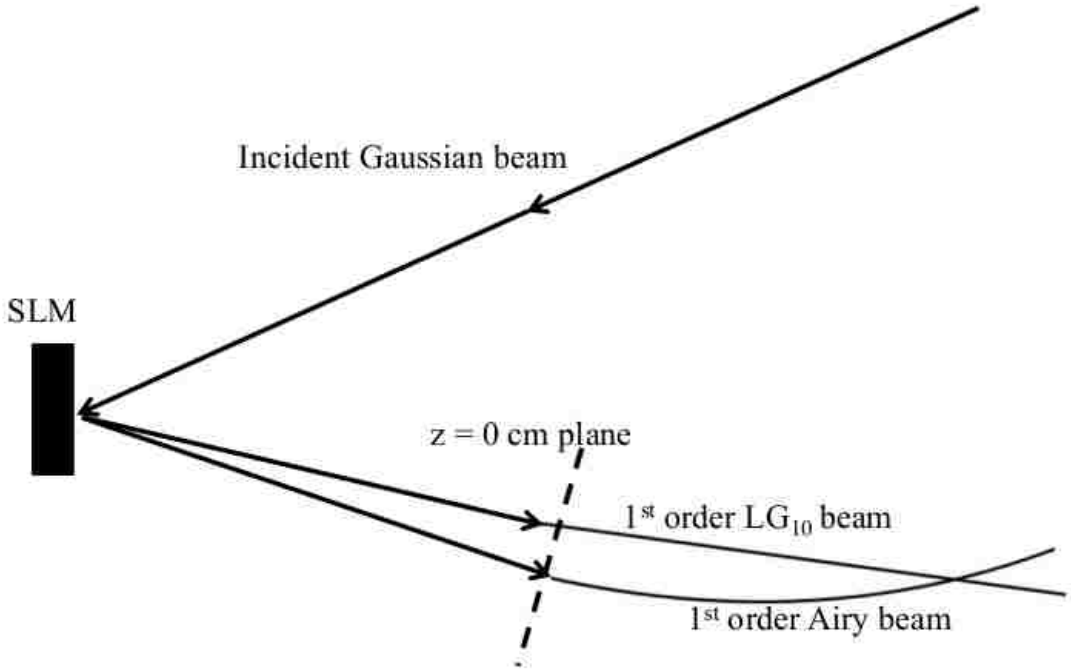

Figure 3.12: The trajectory of the Airy beam was measured relative to the path of the linearly propagating LG_{10} mode.

Though at an angle, the Airy beam still has a parabolic shift in the transverse plane relative to the linear path of the LG beam. To determine the trajectory for a given 'a' value, the Airy beam irradiance was recorded for distances $z = 0, 25, 50, 75, 100, 150, 200$

cm for the cases $a = 0.11, 0.22, 0.97$. For each z, the phase pattern on the SLM was first set to the Airy phase. After recording the irradiance, nothing was adjusted except for the phase pattern on the SLM to switch to the LG beam grating. Then, the LG beam profile was recorded on the CCD. This process was repeated to generate a series of pairs of images that then allows for determining the transverse parabolic path of the Airy beam relative to the LG beam.

3.5 Analysis: Airy beam

For characterization purposes, the trajectory of the Airy beam was tracked relative to the linearly propagating LG beam of first order. This characterization involved, for each pair of images, locating the the vortex of the LG beam and the dominant peak location of the Airy beam profile. The image program, Imagej [39], was used to find the locations of interest in units of pixels by pixels. From the COHU 4800 CCD specifications, the correct conversion from pixels to microns could be determined and then ultimately yield overall transverse displacement in mm versus propagation distance z in cm.

Transverse displacements were plotted against the propagation and the parabolic behavior is shown in the plots in the Figures (3.13) below for each case of 'a' studied.

The value of 'a' for each was further characterized by analyzing the intensity profile at the image plane $z = 0$ cm. The location of the highest intensity value was located using Matlab software with a peak finding function. Once that peak location was determined, the corresponding row of pixels in the image was extracted to plot as a 1D scatter plot. Using OriginLab version 8.0, the intensity was plotted as points against the scaled

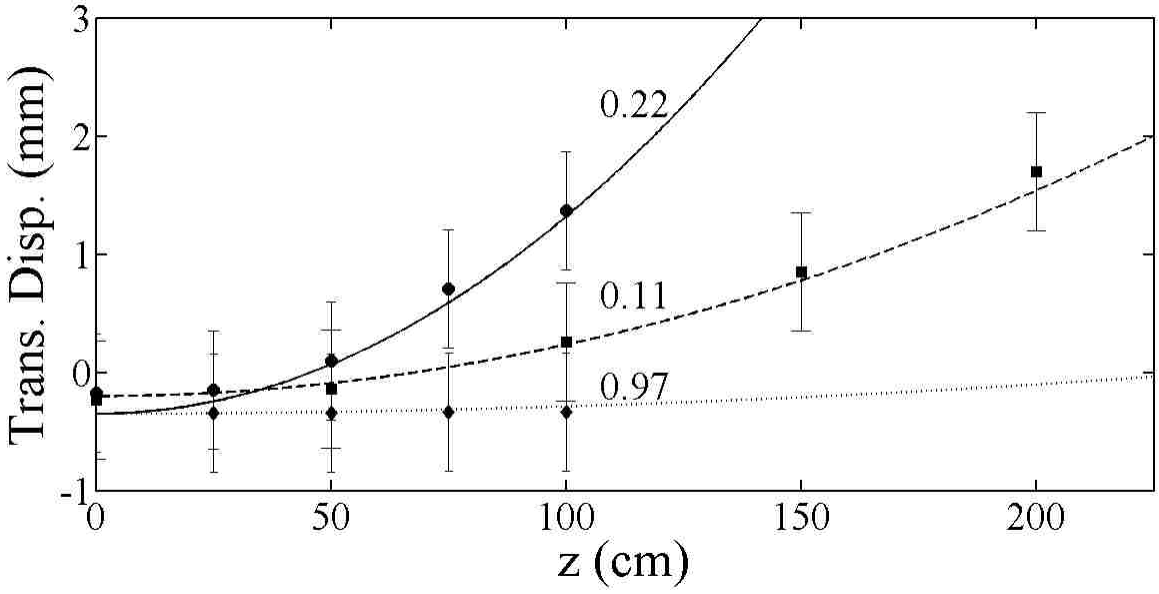

Figure 3.13: Plot showing the trajectories determined for the three cases of $a = 0.1, 0.22, 0.9$.

transverse coordinate, and fit parameters were used for the three values of $a = 0.1, 0.22, 0.9$, with a fitting function of the form

$$f(x) = a + be^{-\frac{c(x-e)}{d}}\mathrm{Ai}(-(x-e)/d)^2. \tag{3.31}$$

Note that the fit parameters were a, b, c, d, and e where the parameter 'e' should not be confused confused with the number e, the exponential base in Equation (3.31). Values for the characteristic length, x_0, from the parabolic plots were used in fit parameters. Visually, the intensity profiles calculated via Mathematica revealed using the a and x_0 values noted here closely match the measured intensity profiles. Mathematica program for the Airy beam intensity is included in Appendix A.3.

With the parabolic trajectory and truncation accurately characterized, it may be concluded that the Airy beam was observed.

The trajectory of the three Airy beams is shown in a plot in Figure (3.15). It should

also be noted that the cross polarization component was also observed to follow the same trajectory. That is, crossing the transmission axes of the polarizer had no observable effect on the transverse displacement between the dominant and cross components.

3.6 Results

Experimentally measured intensity profiles for the DP and CP components of the Airy beam are shown alongside the theoretically computed intensity profiles (from Equations (3.26) and (3.27)) in Figures (3.14)-(3.16) for $a = 0.11$, 0.22, and 0.97 for different propagation distances. The experiments demonstrate the inhomogeneity of polarization of the Airy beam and, in particular, the existence of its cross-polarization component as well as its evolution with propagation distance. For small a (0.11), the intensity profile of the DP component is closer to that of an ideal Airy beam with a large number of peaks and propagates farther without significant diffraction. The CP intensity shows a similar behavior with added feature that each DP peak splits into four asymmetric lobes. With increasing propagation distance, the CP intensity approaches an intensity pattern similar to that of the CP component of a Gaussian beam. With increasing aperture parameter a (0.22), the DP intensity profile has a significantly reduced number of peaks and diffracts faster. The CP intensity profile shows similar behavior with peak splittings.

For large a (≈ 1) case, shown in Figure (3.16), the intensity profiles for both DP and CP components appear similar to those for an asymmetric Gaussian beam. For all values of a used in the experiment, the intensity profiles for both DP and CP components – their spatial structure and evolution with propagation – are found to be in agreement with the

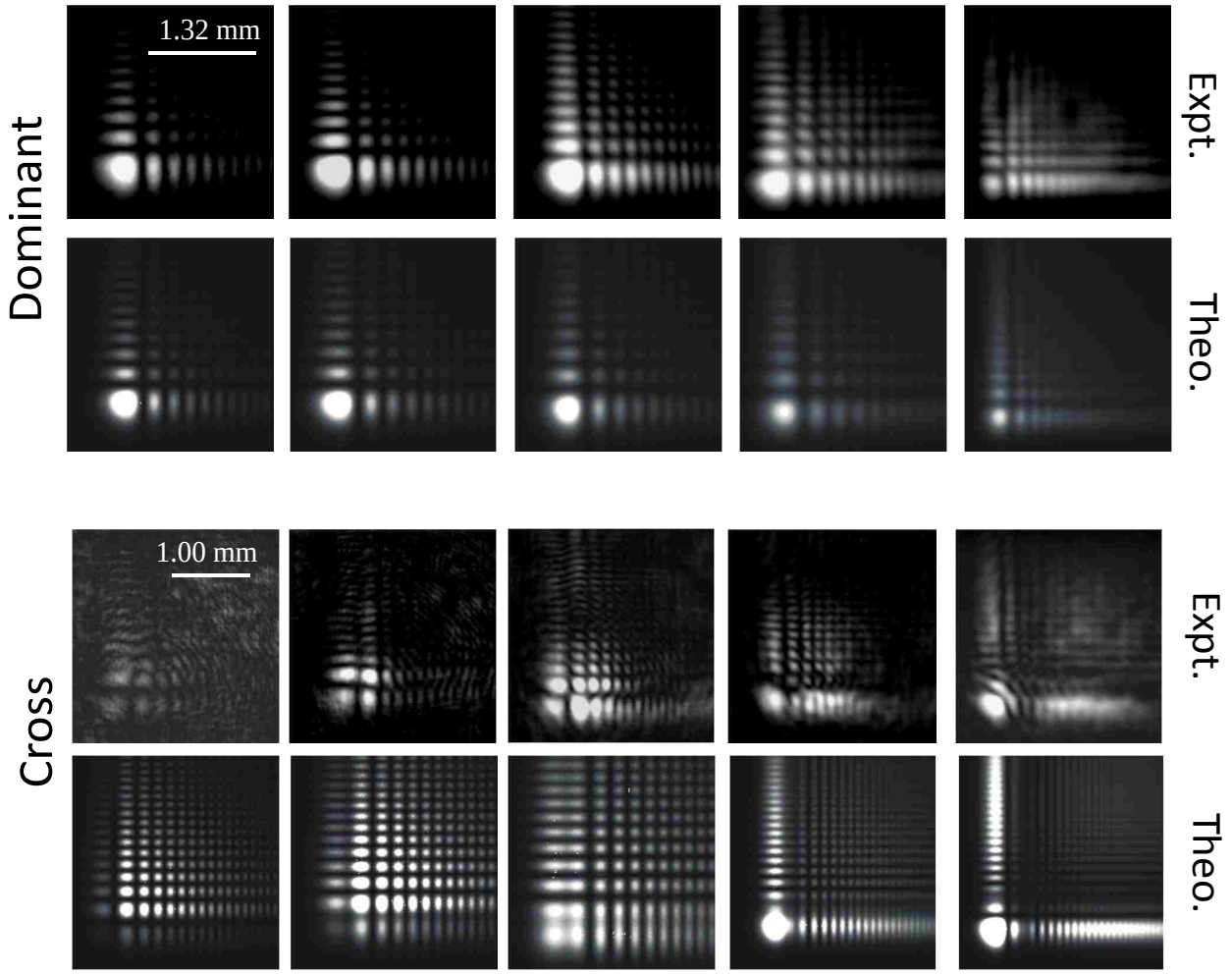

Figure 3.14: Airy beam comparison of experiment to theory for $a = 0.1$ for dominant and cross polarization profiles.

theoretically predictions.

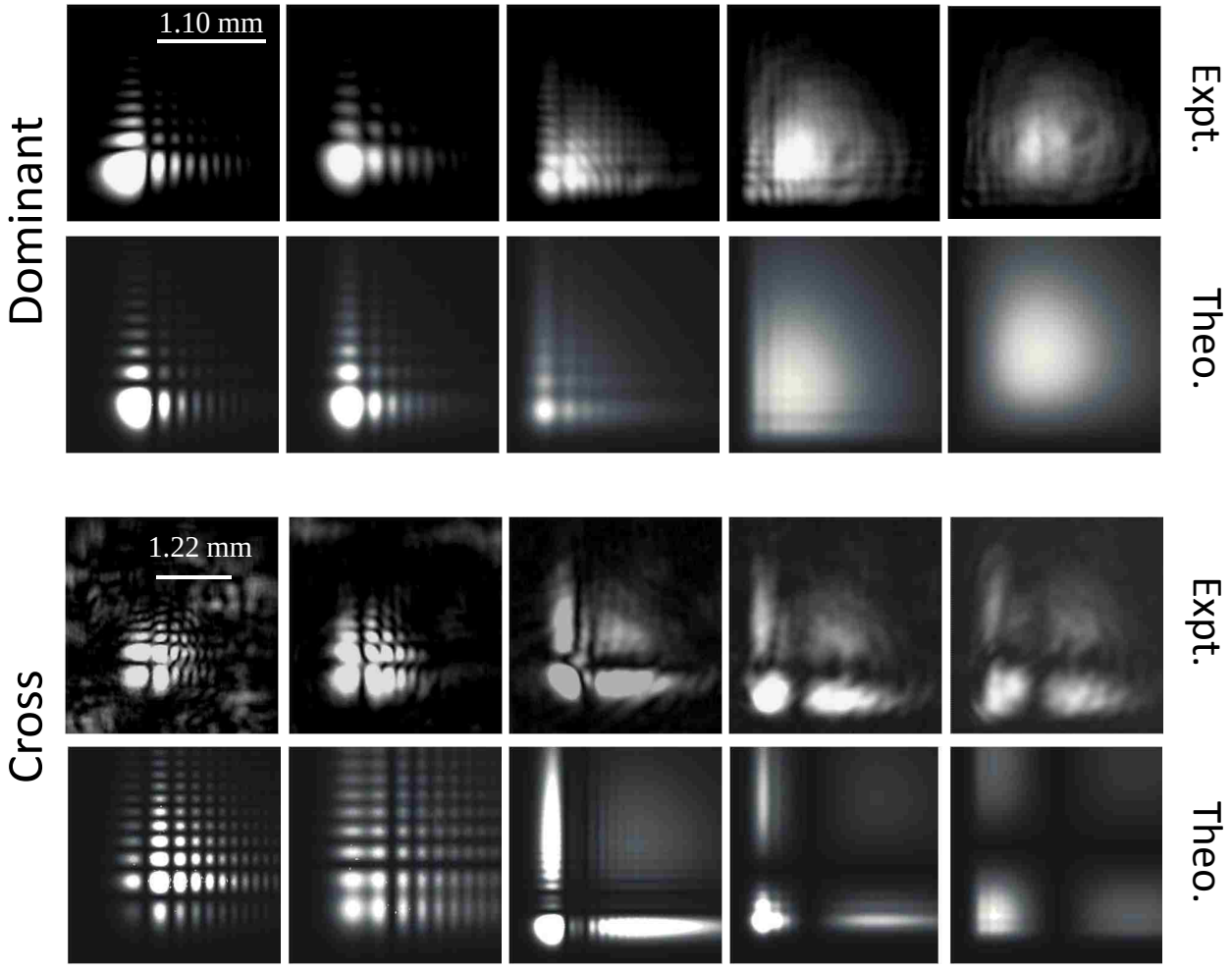

Figure 3.15: Airy beam comparison of experiment to theory for $a = 0.22$ for dominant and cross polarization profiles.

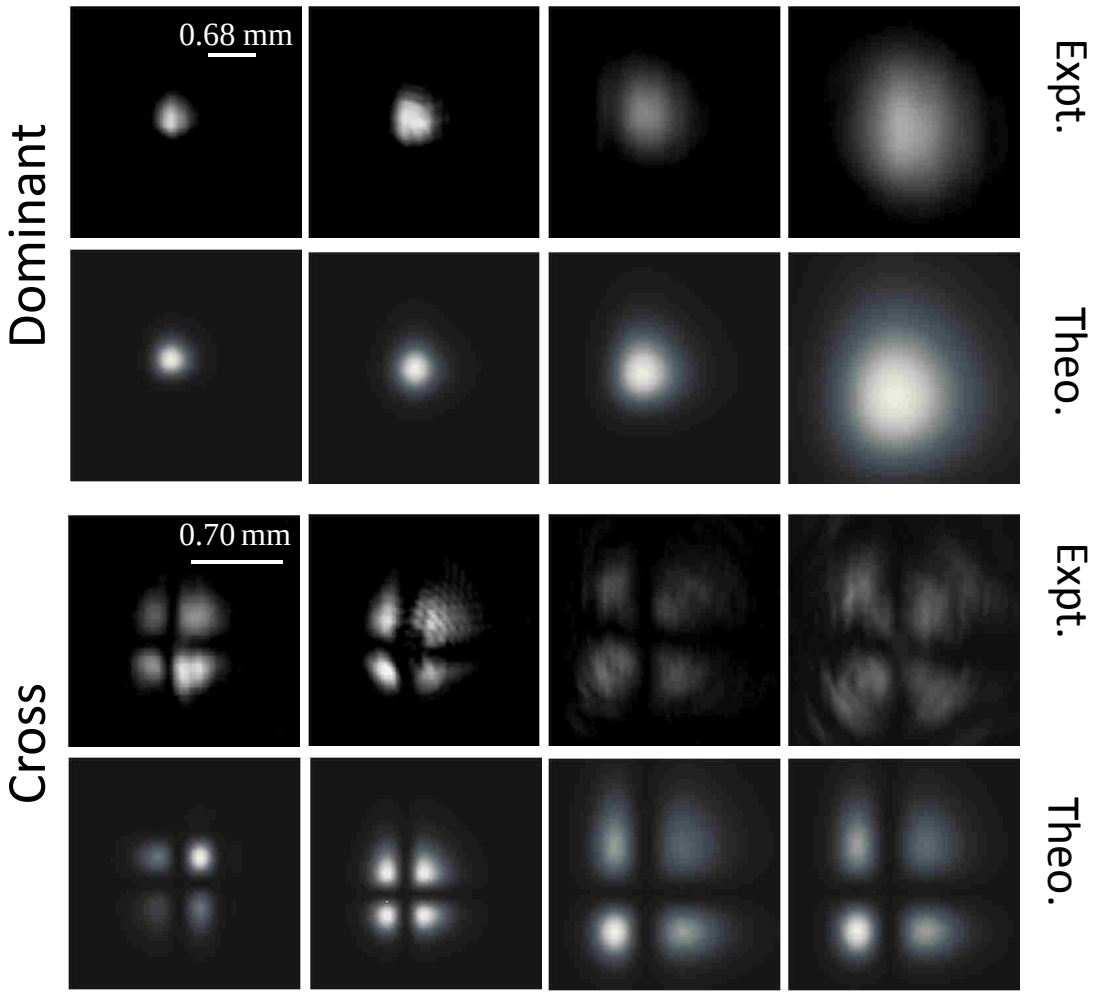

Figure 3.16: Airy beam comparison of experiment to theory for $a = 0.9$ for dominant and cross polarization profiles.

Chapter 4

Polarization Properties of Ince-Gauss Beams

In this chapter, the experiments for measuring the cross polarization of IG beams are discussed [7]. We begin with an introduction of the elliptical coordinate system and the PWE in this system. Then, a derivation of the IG solutions to the PWE is given. Next, the IG beam polarization is discussed along with other properties of IG beams.

After the background theory is given, the experimental procedure on generation of IG beams, observation of polarization intensity profiles, and analysis are presented in that order. Finally, the results of the experiment are shown and compared with theoretical prediction.

4.1 Ince-Gauss Solutions: Elliptical coordinates

Cylindrical polar and Cartesian coordinate systems are the most commonly used systems for discussing beam like solutions of the PWE. There are, however, many more coordinate systems [17] in which the transverse plane can be described. One of them is the elliptical cylindrical coordinate system. This gives the Ince-Gaussian (IG) beam solutions. The transformation from Cartesian to the elliptical cylindrical coordinate system is described as

$$x = f_0 \cos(v) \cosh(u), \tag{4.1}$$

$$y = f_0 \sin(v) \sinh(u), \tag{4.2}$$

for $u \in [0, \infty), v \in [0, 2\pi)$, where f_0 is the semifocal separation related to the ellipticity parameter, $\epsilon = 2f_0^2/w_0^2$ with w_0 as the beam waist at the focus. The semifocal separation

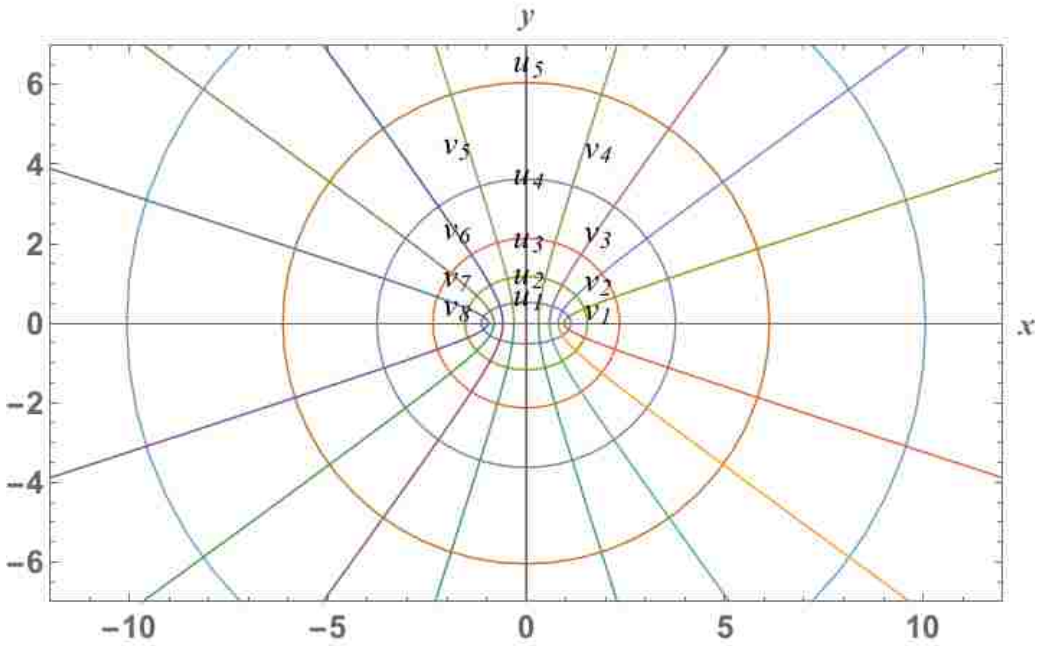

Figure 4.1: Elliptical coordinate system according to variables in Equations (4.1) and(4.2) for $\epsilon = 0.8$.

at the waist is related to the semifocal separation at some z by

$$f(z) = \frac{f_0 w(z)}{w_0}. \tag{4.3}$$

It is important here to note that the ellipticity paramter given here is not the standard definition of ellipticity.

Using the transformations (4.1) and (4.2) to rewrite the PWE, we get

$$\left[\frac{\left(\frac{\partial^2}{\partial u^2} + \frac{\partial^2}{\partial v^2}\right)}{f_0^2(\sinh(u)^2 + \sin(v)^2)} + 2ik\frac{\partial}{\partial z}\right]\psi(\vec{r}) = 0. \tag{4.4}$$

The solutions to the PWE (2.14) use the Ince polynomials $C_p^m(iu,\epsilon)C_p^m(iv,\epsilon)$. For the cosine solution, the Ince-Gaussian mode can be written as

$$IG_{p,m,c}(\vec{r}) = \frac{Aw_0}{w(z)}C_p^m(iu,\epsilon)C_p^m(v,\epsilon)e^{-i(p+1)\phi_{Guoy}(z)}e^{\frac{ikr^2}{2R(z)}}e^{-\frac{r^2}{w(z)^2}}, \tag{4.5}$$

and for sine solution, the IG mode can be expressed as

$$IG_{p,m,s}(\vec{r}) = \frac{Aw_0}{w(z)} S_p^m(iu,\epsilon) S_p^m(v,\epsilon) e^{-i(p+1)\phi_{Guoy}(z)} e^{\frac{ikr^2}{2R(z)}} e^{-\frac{r^2}{w(z)^2}}, \tag{4.6}$$

derived in the next section.

In Equations (4.5) and (4.6) p, m, are the indices for the Ince polynomials, u, v are the radial and azimuthal coordinates with allowed values of $0 \leq m \leq p$ for m, p both being even or odd and $w(z)$ is the beam width at z. In this study, both even and odd IG solutions will be considered. For odd solutions, $S_p^m(iu,\epsilon)$ and $S_p^m(v,\epsilon)$ are the odd Ince polynomials used in place of $C_p^m(iu,\epsilon)$ and $C_p^m(v,\epsilon)$, respectively. Figure (4.1) shows a coordinate system with axes u and v for $\epsilon = 0.8$.

In that system, contours of constant u are hyperbolas which are orthogonal to ellipses, which are contours of constant v for the azimiuthal constant contours. Then, the scalar field amplitudes (4.5) and (4.6) will have nodal lines along those two orthogonal contours.

In general, from indices p and m, $(p-m)/2$ gives the number of nodal lines along the ellipses while the order m is the number of hyperbolic nodal lines. For example, for $(p = 5, m = 5)$, the number hyperbolic nodal lines is 5 which give the five peaks seen in Figures (4.2) and (4.3) where each figure shows an array of IG intensities with p rows and m columns for even IG solutions and odd solutions, respectively. Also, there are $(p-m)/2 = 0$ elliptic nodal lines. The eccentricity for all the plots in Figures (4.2) and (4.3) is $\epsilon = 0.8$.

As the indices change from one value to another, the number of elliptical and hyperbolic nodal lines change. A few examples are as follows.

For (5,5), there are no elliptic nodal lines yet, but for (5,3), the number of elliptic

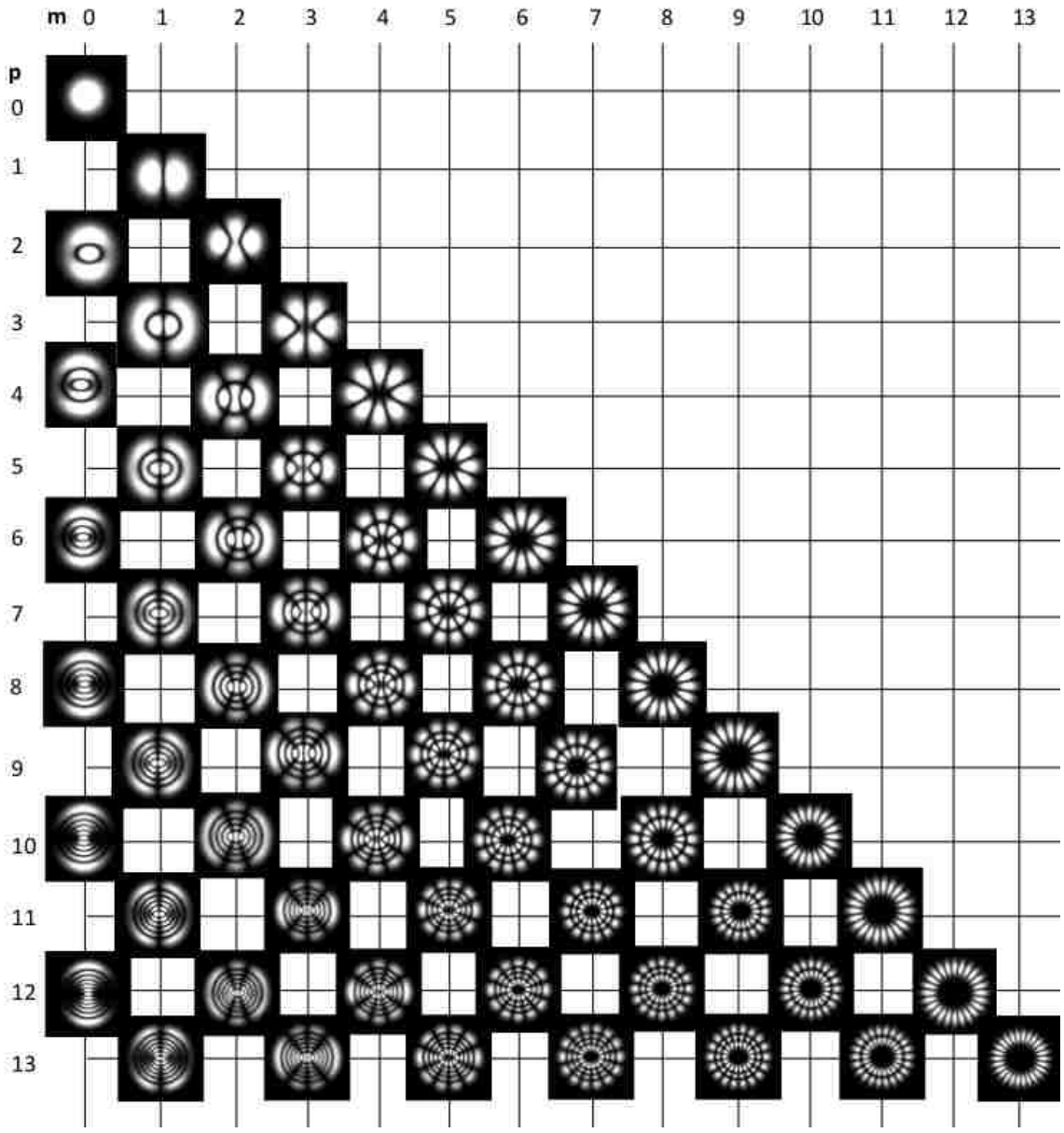

Figure 4.2: An array diagram showing cosine solution $IG_{p,m,c}$ profiles up to $p = 13$ and $\epsilon = 0.8$. Follow the (p, m) coordinate chart to locate the mode of interest. Diagonal, vertical, and horizontal translations within the tree structure reveal nodal line trends as indices change order.

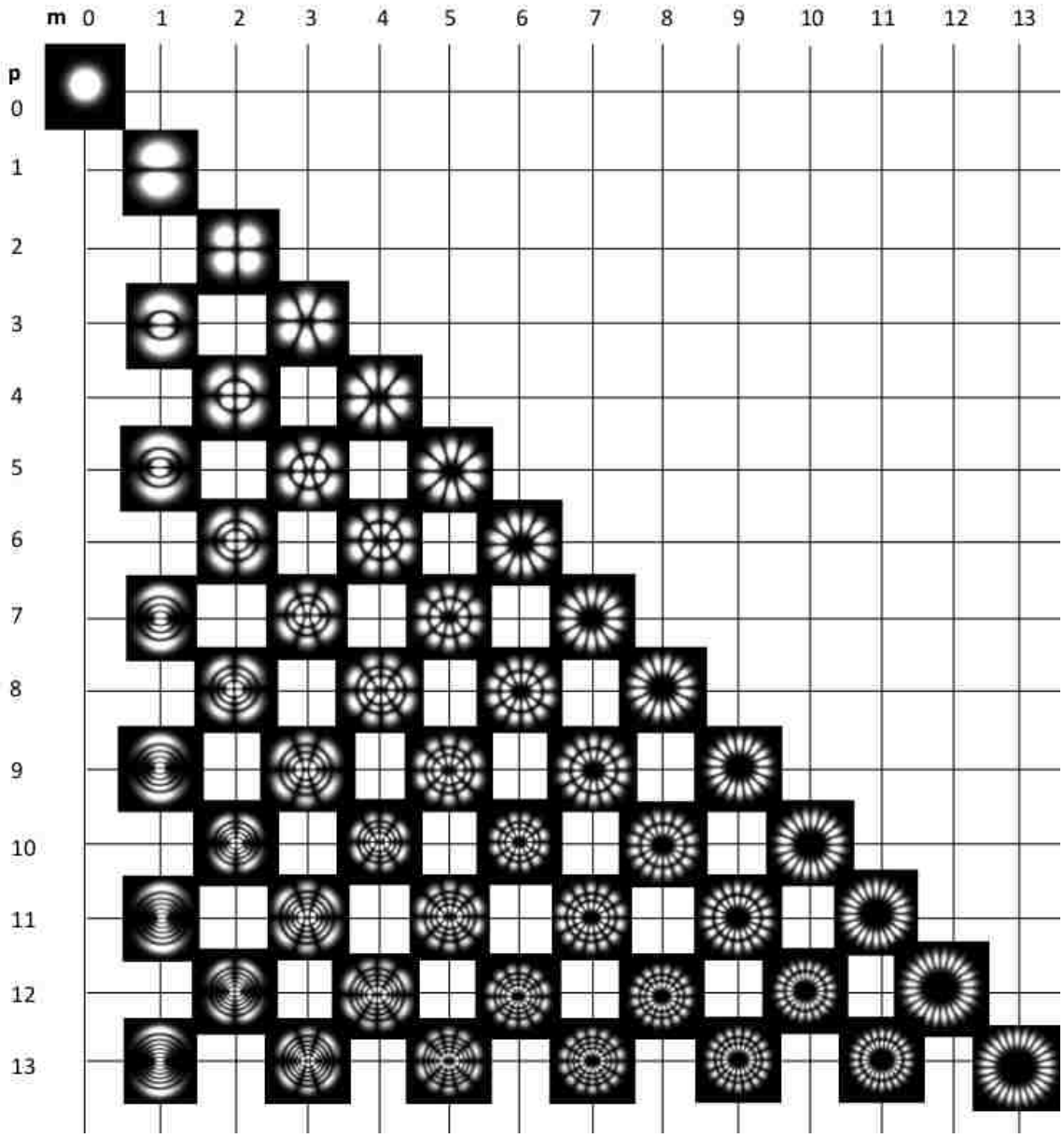

Figure 4.3: An array diagram showing sine solution $IG_{p,m,s}$ profiles up to $p = 13$ and $\epsilon = 0.8$.

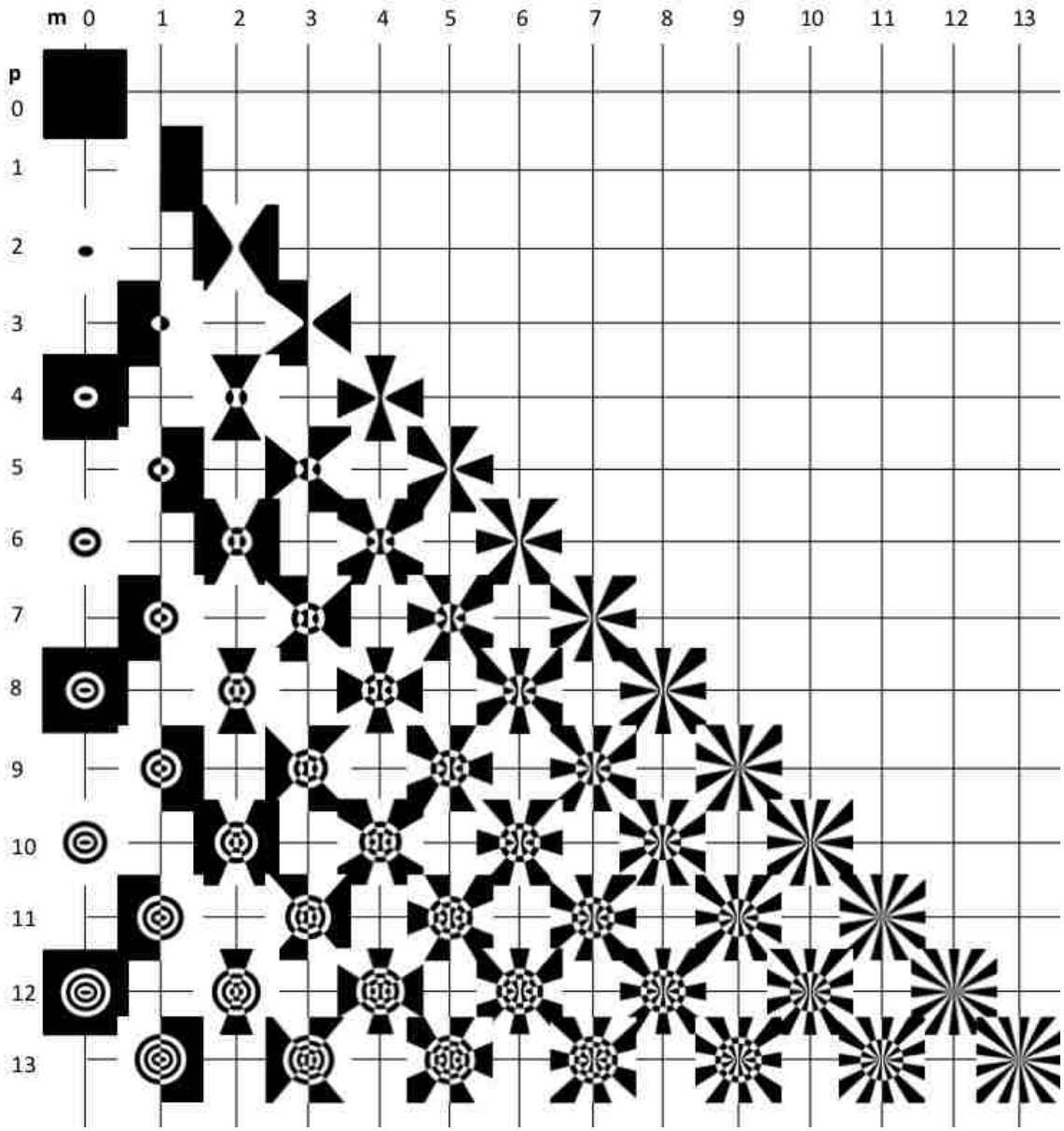

Figure 4.4: Array diagram showing phase profiles up to $p = 13$ and $\epsilon = 0.8$ for cosine type solutions.

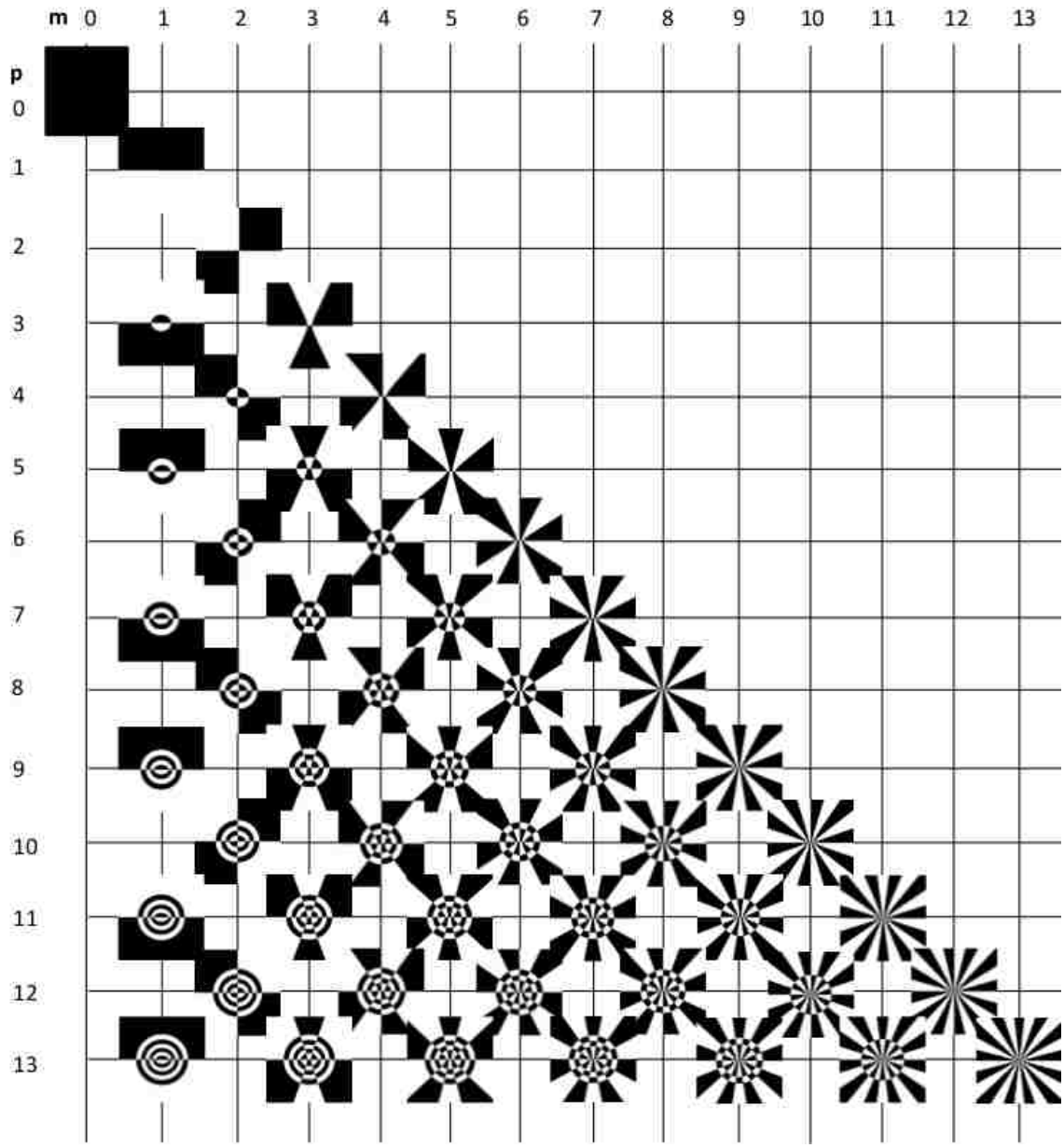

Figure 4.5: Array diagram showing phase profiles up to $p = 13$ and $\epsilon = 0.8$ for sine type in Figure (4.3).

nodal lines increases by 1, but a decrease by 2 of the hyperbolic nodal lines which is present in both Figures (4.2) and (4.3). From (5,3) to (5,1), there is an increase by 2 of the elliptic lines from (5,3) and a decrease of hyperbolic by 2. This trend is also in both Figures (4.2) and (4.3).

In summary, for both even and odd solutions, m is the number of hyperbolic nodal lines, and $(p-m)/2$ is the number of elliptic nodal lines.

In Figures (4.2) and (4.3), visual comparison of the cosine and sine sets of modes shows that they are similar but there are differences. The phase profiles of IG fields show that the adjacent peaks in the amplitude do oscillate out of phase by π as seen with the HG and LG solutions. Phase profiles of IG amplitudes can all be found for modes up to $p = 13$ in Figures (4.4) and (4.5) corresponding to the odd and even solutions, respectively. In each profile, black and white sections in each plot indicate where the phase is either 0 as white or π as black. Then, the transitions between black and white show the π phase shifts which directly correspond to the locations all the nodal lines discussed previously.

and (4.5) show plots of mode phase. It is observed that the plots in Figures (4.4) are different from those in Figures (4.5) by a rotation of $\pi/2$. The phase plots in Figures (4.4) and (4.5) also clearly show the nodal lines and trends observed in the intensity plots in Figures (4.2) and (4.3).

Noting the eccentricity, ϵ is proportional to the distance between the two foci in an elliptical coordinate system, ϵ can range from 0 to ∞. For eccentricity of 0, the foci are superposed at the origin and the coordinate system becomes circular. As the eccentricity increases from 0 to 1, the foci move away from each other and the system becomes elliptical. Once eccentricity reaches 1, the constant value hyperbolic contours will be

parabolic with the orthogonal constant contours as ellipses. But, once the eccentricity goes beyond 1, the system becomes increasingly rectangular as the foci move further and further apart to an infinite separation. The infinite separation of the foci causes the coordinate system to be rectangular, or Cartesian.

In terms of the HG, LG, and IG modes mentioned, the eccentricity describes how the IG modes evolve beginning at LG modes with $\epsilon = 0$ and ending at HG modes with $\epsilon = \infty$.

Thus, at $\epsilon = 0$, we have the cylindrical polar coordinate system for LG solutions, HG solutions at $\epsilon = \infty$ with a rectangular coordinate system and IG solutions for any intermediate value of ϵ in an elliptical cylindrical coordinate system.

In addition to having the IG solutions as shown in Equations (4.5) and (4.6), there also exist helical IG solutions, HIG, that are a superposition of the even and odd IG solutions of the form

$$HIG_{p,m} = IG_{p,m,c} + iIG_{p,m,s}. \tag{4.7}$$

More about HIG beams will be discussed later.

4.2 Ince Gauss derivation

The paraxial wave equation in elliptical coordinates via the transformation by Equations (4.1) and (4.2) was given by Equation (4.4).

As with the LG and HG solutions, we look for solutions of the form

$$\psi(\vec{r}) = g(\xi)h(\eta)e^{iP(z)}e^{\frac{ikr^2}{2q(z)}}. \tag{4.8}$$

where the scaled coordinates ξ and η are

$$\xi = \frac{u}{w(z)} \tag{4.9}$$

and

$$\eta = \frac{v}{w(z)}. \tag{4.10}$$

To start, Equation (4.8) can be substituted into (4.4). This gives

$$\begin{aligned}
&\beta^2 g(\xi)h(\eta)e^{iP(z)}\left(\frac{\partial^2}{\partial u^2}+\frac{\partial^2}{\partial v^2}\right)\psi(\vec{r}) + 2\left[\beta\left(\frac{\partial}{\partial u}+\frac{\partial}{\partial v}\right)(g(\xi)h(\eta)e^{iP(z)})\beta\left(\frac{\partial}{\partial u}+\frac{\partial}{\partial v}\right)\psi(\vec{r})\right] \\
&+ \beta^2\psi(\vec{r})\left(\frac{\partial^2}{\partial u^2}+\frac{\partial^2}{\partial v^2}\right)(g(\xi)h(\eta)e^{iP(z)}) \\
&+ \left(\psi(\vec{r})\frac{d}{dz}\left(g(\xi)h(\eta)e^{iP(z)}\right) + g(\xi)h(\eta)e^{iP(z)}\frac{d}{dz}\psi(\vec{r})\right) = 0.
\end{aligned} \tag{4.11}$$

In Equation (4.11),

$$\beta^2 = 1/(f_0^2(\sinh^2 u + \sin^2 v)), \tag{4.12}$$

was used. Each of the five terms here, in Equation (4.11), may be simplified individually.

In order, the first term is

$$\begin{aligned}
&\beta^2 g(\xi)h(\eta)e^{iP(z)}\left(\frac{\partial^2}{\partial u^2}+\frac{\partial^2}{\partial v^2}\right)\psi(\vec{r}) \\
&= \beta^2 g(\xi)h(\eta)e^{iP(z)}\left[\frac{ik}{q(z)}(\cosh(2u)-\cos(2v)) - \frac{k^2(\sinh(2u)^2 + sin(2v)^2)}{4q(z)^2}\right]\psi(\vec{r}).
\end{aligned} \tag{4.13}$$

Using the chain rule, the partial derivatives of η and ξ respect to u and v, respectively, are

$$\frac{\partial \xi}{\partial u} = \frac{1}{w(z)}\frac{\partial u}{\partial u} = \frac{1}{w(z)} \tag{4.14}$$

and

$$\frac{\partial \eta}{\partial v} = \frac{1}{w(z)} \frac{\partial v}{\partial v} = \frac{1}{w(z)}. \tag{4.15}$$

Then, further using the chain rule for $g(\xi)$ and $h(\eta)$ then is just

$$\frac{\partial g(\xi)}{\partial u} = \frac{dg(\xi)}{d\xi} \frac{\partial \xi}{\partial u} = \frac{dg(\xi)}{w(z) d\xi} \tag{4.16}$$

and

$$\frac{\partial h(\eta)}{\partial u} = \frac{dh(\eta)}{d\eta} \frac{\partial \eta}{\partial u} = \frac{dh(\eta)}{w(z) d\eta}. \tag{4.17}$$

Then, the second term, the cross term from Equation (4.11), becomes

$$\begin{aligned} &2\left[\beta\left(\frac{\partial}{\partial u} + \frac{\partial}{\partial v}\right)(g(\xi)h(\eta)e^{iP(z)})\beta\left(\frac{\partial}{\partial u} + \frac{\partial}{\partial v}\right)\psi(\vec{r})\right] \\ &= 2\beta^2 e^{iP(z)}\left(\frac{g(\xi)'}{w(z)}h(\eta)\frac{h(\eta)'}{w(z)}g(\xi)\right)\left(\frac{ik}{q(z)}(\cosh(u)\sinh(u) - \cos(v)\sin(v))\right)\psi(\vec{r}) \end{aligned} \tag{4.18}$$

After more derivation, third term is

$$\beta^2\psi(\vec{r})\left(\frac{\partial^2}{\partial u^2} + \frac{\partial^2}{\partial v^2}\right)(g(\xi)h(\eta)e^{iP(z)}) = \beta^2\psi(\vec{r})e^{iP(z)}\left(\frac{g''(\xi)}{w(z)^2}h(\eta) + \frac{h''(\eta)}{w(z)^2}g(\xi)\right). \tag{4.19}$$

The fourth term is

$$\begin{aligned} &2ik\psi(\vec{r})\frac{d}{dz}\left(g(\xi)h(\eta)e^{iP(z)}\right) \\ &= -2ik\psi(\vec{r})e^{iP(z)}\left[\frac{w'(z)f'(z)}{w(z)^2}(g'(\xi)h(\eta) + h'(\eta)g(\xi)) - iP'(z)g(\xi)h(\eta)\right] \end{aligned} \tag{4.20}$$

after noting the chain rules with respect to z, and using Equation (4.3) for $f'(z)$.

$$\frac{dg(\xi)}{dz} = \frac{dg(\xi)}{d\xi}\frac{\xi}{z} = -\frac{w'(z)f'(z)g'(\xi)}{w(z)^2} \tag{4.21}$$

$$\frac{dh(\eta)}{dz} = \frac{dh(\eta)}{d\eta}\frac{\eta}{z} = -\frac{w'(z)f'(z)h'(\eta)}{w(z)^2} \tag{4.22}$$

The last term in Equation (4.11) is now

$$\begin{aligned} &2ikg(\xi)h(\eta)e^{iP(z)}\frac{d}{dz}\psi(\vec{r}) \\ &= -2ik\psi(\vec{r})e^{iP(z)}\left[\frac{ik}{4q(z)^2}(\cosh(2u)+\cos(2v))\right]. \end{aligned} \tag{4.23}$$

In rewriting Equation (4.11), (4.16) and (4.17) have a couple relations useful for simplification.

$$\beta^2\left[\frac{ik}{q(z)}(\cosh(2u)-\cos(2v))\right] = \frac{2ik}{f_0^2 q(z)} \tag{4.24}$$

$$\beta^2\left[-\frac{k^2(\sinh(2u)^2+\sin(2v)^2)}{4q(z)^2}\right] = -\frac{k^2(\cosh(2u)+\cos(2v))}{2f_0^2 q(z)^2} \tag{4.25}$$

Then, (4.24) and (4.25) allow for the separation of some of the functions in the trial solution Equation (4.8). That is, the term $g(\xi)h(\eta)e^{iP(z)}\psi(\vec{r})$ may be divided through the simplified Equation (4.11).

The result then becomes

$$\begin{aligned} &\frac{2ik}{f_0^2 q(z)} + \frac{2\beta^2}{w(z)}\left[\left(\frac{g'(\xi)}{g(\xi)}+\frac{h'(\eta)}{h(\eta)}\right)\frac{ik}{2q(z)}(\sinh(2u)-\sin(2v))\right] \\ &+\frac{\beta^2}{w(z)^2}\left(\frac{g''(\xi)}{g(\xi)}+\frac{h''(\eta)}{h(\eta)}\right) - \frac{2ik}{w(z)^2}\left[w'(z)f'(z)\left(\frac{g'(\xi)}{g(\xi)}+\frac{h'(\eta)}{h(\eta)}\right)\right] - 2kP'(z) = 0. \end{aligned} \tag{4.26}$$

Rearranging Equation (4.26) and multiplying by $w(z)^2$,

$$\begin{aligned}&\beta^2\left(\frac{g''(\xi)}{g(\xi)}+\frac{h''(\eta)}{h(\eta)}\right)+2ik\beta^2\left[\left(\frac{w(z)}{2R(z)}-\frac{if'(z)}{kw(z)}\right)(\sinh(2u)-\sin(2v))\right]\\&\times\left(\frac{g'(\xi)}{g(\xi)}+\frac{h'(\eta)}{h(\eta)}\right)=-\left[\frac{2ik}{q(z)}-2kP'(z)\right]w(z)^2\end{aligned}\tag{4.27}$$

then it is more convenient to apply the separation of variables. With Equation (4.27), both sides of the equation must be equal to a constant.

$$\frac{g''(\xi)}{g(\xi)}+\frac{h'(\eta)}{h(\eta)}+2ik\left[\left(\frac{w(z)}{2R(z)}-\frac{if'(z)}{kw(z)}\right)(\sinh(2u)-\sin(2u))\right]\left(\frac{g'(\xi)}{g(\xi)}+\frac{h'(\eta)}{h(\eta)}\right)=\frac{d^2}{\beta^2}\tag{4.28}$$

$$-\left[\frac{2ik}{q(z)}-2kP'(z)\right]w(z)^2=d^2\tag{4.29}$$

Here, $d^2=s^2/w_0^2$ where $s2$ is a separation constant. Equation (4.29) may be solved for $P(z)$ to determine the Guoy phase for an Ince-Gauss beam. The Equation (4.28), much like with the previous derivations having separable functions of Cartesian or cylindrical coordinates, has separable functions of the variables ξ and η and can be rewritten to reveal the two second order differential equations.

$$\begin{aligned}&\frac{g''(\xi)}{g(\xi)}+2ik\left(\frac{w(z)}{2R(z)}-\frac{if'(z)}{kw(z)}\right)\sinh(2u)\frac{g'(\xi)}{g(\xi)}-d^2f_0^2\sinh(u)^2\\&+\frac{h''(\eta)}{h(\eta)}+2ik\left(\frac{w(z)}{2R(z)}-\frac{if'(z)}{kw(z)}\right)\sin(2v)\frac{h'(\eta)}{h(\eta)}-d^2f_0^2\sin(v)^2=0\end{aligned}\tag{4.30}$$

In Equation (4.30), the two lines show that this equation can be reduced further via some separation constant, c. Then, multiplying the top and bottom expressions by g and h, respectively, and applying the paraxial approximation to the middle terms of each, the following two differential equations are and are becoming closer to the desired forms for

elliptical coordinates from the paraxial equation.

$$g''(\xi) - 2\frac{f_0^2}{w_0^2}\sinh(2u)g'(\xi) - (c + d^2 f_0^2 \sinh^2(u))g(\xi) = 0 \tag{4.31}$$

$$h''(\eta) + 2\frac{f_0^2}{w_0^2}\sin(2v)h'(\eta) + (c - d^2 f_0^2 \sin^2(v))h(\eta) = 0 \tag{4.32}$$

There are a couple of steps remaining to get to the known differential equations desired from Equations (4.31) and (4.32). The zero order terms for g and h can be rewritten leaving the hyperbolic functions linear instead of quadratic, non-linear.

$$\sinh^2 u = \frac{\cosh 2u - 1}{2} \tag{4.33}$$

$$\sin^2 v = \frac{1 - \cos 2v}{2} \tag{4.34}$$

Then, the identification

$$a = c - \frac{d^2 f_0^2}{2}, \tag{4.35}$$

$$p = -\frac{d^2}{4}, \tag{4.36}$$

$$\epsilon = 2\frac{f_0^2}{w_0^2}, \tag{4.37}$$

in Equations (4.32) and (4.33) lead to the modified Ince equation and the Ince equation

$$h'(\eta) + \epsilon\sin(2v)h'(\eta) + (a - p\epsilon\cos(2v))h(\eta) = 0 \tag{4.38}$$

and

$$g''(\xi) - \epsilon\sinh(2u)g'(\xi) + (a - p\epsilon\cosh(2u))g(\xi) = 0, \tag{4.39}$$

respectively [40]. The modified equation is obtained from the Ince equation by changing the arguments to be imaginary, $\eta \to i\xi$. The Ince equation (4.37) has solutions called the

Ince polynomials. These periodic series have even or odd parity. To derive the Ince polynomials, a trial solution for Equation (4.38) of the form

$$h(v) = \Sigma_{r=0}^{\infty} A_r \cos(2rv) \tag{4.40}$$

gives the recurrence relation

$$-aA_0 + (p/2+1)\epsilon A_1 = 0, r = 0, \tag{4.41}$$

$$p\epsilon A_0 + (4-a)A_1 + (p/2+2)\epsilon A_2 = 0, r = 1, \tag{4.42}$$

$$(p/2-r)\epsilon A_r + (4(r+1)^2 - a)A_{r+1} + (p/2+r+2)\epsilon A_{r+2} = 0, r \geq 1. \tag{4.43}$$

Setting the order $p = 2n$ as even and $A_{n+1} = 0$ for some a the recurrence relations terminate at a finite n leading to the following set of equations

$$-aA_0 + (n+1)\epsilon A_1 = 0, \tag{4.44}$$

$$2n\epsilon A_0 + (4-a)A_1 + (n+2)\epsilon A_2 = 0, \tag{4.45}$$

$$(n-r)\epsilon A_r + (4(r+1)^2 - a)A_{r+1} + (n+r+2)\epsilon A_{r+2} = 0, \tag{4.46}$$

$$(r = 1, 2, \ldots, n-2),$$

$$\epsilon A_{n-1} + (4n^2 - a)A_n = 0. \tag{4.47}$$

The set of Equations (4.44)-(4.47) can be set up as a tridiagonal matrix in order to solve for the coefficients, A_r and $n+1$ eigenvalues of a. The eigenvalues are written as $a_{p=2n}^{m=2k}(\epsilon)$ with $k = 0, 1, \ldots, n$. The eigenvalues for system of equations relate to the coefficients of the Ince polynomials. For the current $p = 2n$, the number of eigenvalues is $n+1$, and the index m is equal to $2k$. The series is given in Equation (4.40). A trial solution using a sine

function in place of cosine results in Equation (4.50).

If the order is defined to be odd, $p = 2n + 1$, there are still $n + 1$ eigenvalues, but the argument of the trigonometric functions in the series is changed to include only odd integers of the form $2r + 1$. Finite order n still applies for these index conditions.

Thus, there are four possible cases: even indices with cosine or sine solutions or odd indices with cosine or sine solutions. The series are for all four cases are [40]

$$C_p^m(u,\epsilon) = \Sigma_{r=0}^{n} A_r \cos(2ru),\ p,m \in even \tag{4.48}$$

$$C_p^m(u,\epsilon) = \Sigma_{r=0}^{n} A_r \cos((2r+1)u),\ p,m \in odd \tag{4.49}$$

$$S_p^m(u,\epsilon) = \Sigma_{r=1}^{n} B_r \sin(2ru),\ p,m \in even \tag{4.50}$$

$$S_p^m(u,\epsilon) = \Sigma_{r=0}^{n} B_r \sin((2r+1)u),\ p,m \in odd. \tag{4.51}$$

Each of the Equations (4.48)-(4.51) are normalized by

$$\int_{-\pi}^{\pi} [S_p^m(u,\epsilon)]^2 du = \int_{-\pi}^{\pi} [C_p^m(u,\epsilon)]^2 du = \pi. \tag{4.52}$$

Equation (4.52) holds for either even or odd indices. Each of the Equations (4.48)-(4.51) may be substituted into the modified Ince's equation (4.38) and each series produces recurrence relations for coefficients, A_r and B_r. Equations (4.53)-(4.56) show sets of recurrence relations each of which may be rearranged to set up a system of equations with the coefficients as the basis. The recurrence relations for (4.48)-(4.51) are

$$C_p^m, even: \begin{cases} (\frac{p}{2}+1)\epsilon A_1 = aA_0, \\ (\frac{p}{2}+1)\epsilon A_2 = -p\epsilon A_0 - (4-a)A_1, \\ (\frac{p}{2}+1)\epsilon A_{r+2} = [a - 4(r+1)^2]A_{r+1} + (r - \frac{p}{2})\epsilon A_r, \end{cases} \tag{4.53}$$

$$C_p^m, odd: \begin{cases} (p+3)\frac{\epsilon}{2}A_1 = [a - \frac{\epsilon}{2}(p+1) - 1]A_0, \\ (p+2r+3)\frac{\epsilon}{2}A_{r+1} = [a-(2r+1)^2]A_r + \frac{\epsilon}{2}(2r-p-1)A_{r-1}, \end{cases} \tag{4.54}$$

$$S_p^m, even: \begin{cases} (\frac{p}{2}+2)\epsilon B_2 = (\beta - 4)B_1, \\ (\frac{p}{2}+r+2)\epsilon B_{r+2} = [\beta - 4(r+1)^2]B_{r+1} + (r-\frac{p}{2})\epsilon B_r, \end{cases} \tag{4.55}$$

$$S_p^m, odd: \begin{cases} (p+3)\frac{\epsilon}{2}B_1 = [\beta - \frac{\epsilon}{2}(p+1) - 1]B_0, \\ (p+2r+3)\frac{\epsilon}{2}B_{r+1} = [\beta-(2r+1)^2]B_r + \frac{\epsilon}{2}(2r-p-1)B_{r-1}. \end{cases} \tag{4.56}$$

Each system of equations results in a tridiagonal matrix, $\mathbb{M}$, which can then be diagonalized by taking the determinant of $\mathbb{M}$ and solving for the roots of the secular equation, $\det|(\mathbb{M} - a_m^p\mathbb{I})| = 0$, to obtain eigenvalues, a_m^p [40].

The obtained eigenvalues are substituted back into recurrence relations (4.53)-(4.56) to determine coefficients, A_r and B_r. The now known coefficients can be substituted back into either Equations (4.48) and (4.49) for A_r and Equations (4.50) and (4.51) for B_r to reveal the Ince polynomials for a given order p. Thus, Equation (4.28) has been solved, but Equation (4.29) remains.

The solution to Equation (4.29), derived in [6], is the Guoy phase for Ince-Gauss beams. With beam parameter, $q(z)$, Equation (2.20), and noting that

$$\frac{i}{q(z)} = \frac{iz}{z^2+z_R^2} - \frac{z_0}{z^2+z_R^2}, \tag{4.57}$$

the solution to Equation (4.29) is

$$\exp(iP(z)) = \frac{w_0}{w(z)} \exp(-i(p+1)\phi_{Guoy}(z)). \tag{4.58}$$

Similar expressions were discussed previously with the HG and LG beams. The Guoy phase for IG beams is $(p+1)\arctan^{-1}(z/z_R)$. Compared to HG and LG beams, the integer factor for their Guoy phases are $m+n+1$ and $2|l|+p$, respectively.

Combining the solutions of (4.29) and (4.30) gives the entire solution to the PWE in elliptical cylindrical coordinates as Equations (4.4) and (4.5).

Thus, once indices p and m are chosen, the above derivation and procedure can be used to determine the IG solutions. The indice p and m must both be either even or odd. Index p determines the maximum range for integer values of m. For example, let $p = 5$, then m must be odd and can take on values of $1, 3$, or 5. Or, suppose $p = 8$, then even m may be $2, 4, 6$, or 8. So that, given that p is an integer, $min(p) \leq m \leq p$, where p, m are both even or odd. The various allowed values for p and m dictate the overall symmetry in the IG mode of interest and the number of elliptic or hyperbolic nodal lines expected in the IG mode and also then for the intensity as well. The choice of $p = m = 0$ will yield the fundamental Gaussian beam as expected. However, with $p \neq 0$, begins to show modes with real structure. With (p=1,m=1), the field, shown in Figure (4.2), is identical to the HG mode HG_{11} [8]. When $p = 1$, note that there are no other allowed modes for this order.

For the next order of $p = 2$, there are two possible modes since m may be 0 or 2. With (2,0), the mode has only two elliptical nodal lines leaving the intensity appearing similar to the CBS television logo with some eccentricity. But, for the (2,2) mode, the elliptical (or azimuthal) nodal lines are gone and the hyberbolic (radial) nodal lines manifest themselves

twice - two nodal lines in this direction. The result being the intensity having four distinct peaks. This $p = 2$ mode is shown in the figure below along with modes up to $p = 5$. The same trend is observed for all the modes. For example, with (5,5), (5,1) has 5 azimuthal nodal lines counting from how many intersections a vertical line makes with the azimuthal nodes. For the first increment of +2 in m, (5,3), the number of azimuthal nodal lines decreases by 2 while the number of radial nodal lines increases by 2. The node across the "+x-axis" is counted as an azimuthal nodal line. After one more jump to (5,5), the azimuthal lines are gone, but the radial nodal lines are there in full with 5 of them resulting in the 10 total peaks surrounding the origin.

An additional parameter that can be changed continuously is the eccentricity, or also referred to as the ellipticity parameter [21]. This parameter is one that sets this family of solutions apart from the HG and LG modes in that changing the eccentricity allows one to change the modes continuously.

Figure (4.6) shows the modes from (1,1) up to (5,5), and also how these modes appear as the eccentricity, ϵ, changes from nearly zero up to 4.0. From that figure, it can be seen directly that the modes are very much circular and radially symmetric for near zero eccentricity. At zero ellipticity, the solutions are exactly radially symmetric. Quickly, even before the eccentricity reaches 1.0 for a parabola, the approximate radial symmetry is broken and the elliptical appearance is noticeable.

The range of eccentricity $[0, \infty)$, allow IG beams to transition between HG and LG beams. As $\epsilon \to \infty$ the three families of modes become HG modes and as $\epsilon \to 0$ the modes become LG modes. Values of ϵ in between the range limits are IG modes with either more HG character, larger ϵ or more LG character, smaller ϵ.

As ϵ is varied to either of its range limits, the indices of HG, LG, and IG modes must change. The relations between the indices of the three modes are

$$HG_{n_x,n_y} \leftrightarrow IG_{p,m,s\,,or\,c}\, n_x = m, n_y = p - m, \tag{4.59}$$

$$LG_{l,p} \leftrightarrow IG_{p,m,s\,,or\,c}\, l = m, n = (p - m)/2, \tag{4.60}$$

where n in Equation (4.60) is the total order of the beam mode.

So far, the IG modes have been discussed as standalone modes. But, the even and odd IG modes may be added as linear combinations to produce what are called helical Ince-Gaussian modes.

$$HIG^{\pm}_{p,m} = IG_{p,m,c} \pm iIG_{p,m,s} \tag{4.61}$$

Note the $\pm i = e^{\pm i\pi}$ factor in this basis. Though it is not explicit in the arguments of the functions in (4.61), they also depend on ellipticity, ϵ. Figure 4.7 below shows example of an $HIG^{+}_{5,5}$ beam (intensity) cross section with changing ellipticity.

The interesting similarity here is the likeness to the LG beams. HIG beams are very much like the LG beams except in that the HIG beams are an elliptical version of them. Not only in intensity or spatial distribution are they elliptic in nature, but the HIG modes also exhibit a rotating phase, albeit an elliptical one. Besides the shape, the order p determines how many concentric ellipses are to be observed in the cross section of the HIG modes. This is similar to the way LG beams have concentric rings with an increase in order p.

Before moving on to polarization, the propagation of the IG beams, is the higher order HG and LG modes discussed earlier. The spatial extent in terms of the spot size and radii

of curvature are the same for the HG, LG and IG beams since the z dependence in the solutions to the PWE for there three beams are all similar functions.

As the beam propagates, its size changes but its spatial structure remains the same. This is to be expected since the solutions satisfy the same PWE for each value of z.

4.3 IG polarization

It was shown earlier that a Maxwell solution for a beam dominantly, linearly polarized in the x-direction has all three fields components, non-zero, and given by [7]

$$E_x = A\psi(\vec{r}), \tag{4.62}$$

$$E_y = \left(\frac{A}{2k^2}\right)\frac{\partial^2\psi(\vec{r})}{\partial x \partial y}, \tag{4.63}$$

$$E_z = \left(\frac{iA}{k}\right)\frac{\partial\psi(\vec{r})}{\partial x}, \tag{4.64}$$

Then, as with the previous solutions of the paraxial equation for a linearly polarized IG beam we take

$$\psi(\vec{r}) = IG_{p,m,s\,or\,c}(\vec{r}). \tag{4.65}$$

The three field expressions have been truncated to the leading order in the expansion of the ratio of the wavelength to the beam spot size. As mentioned before, the dominant component has the greatest amount of power associated with it, being directly proportional to the modulus squared of the scalar solution. Then, the longitudinal followed by the cross polarization components are next in order of decreasing power.

To derive expressions for the fields, it will be necessary to differentiate (4.63) and

(4.64), so the inverse transformations, $u(x,y), v(x,y)$, are necessary for evaluating the operations $\partial/\partial x$ and $\partial/\partial y$.

$$u(x,y) = Re\left[\cosh^{-1}\left(\frac{x+iy}{f_o}\right)\right], \tag{4.66}$$

$$v(x,y) = Im\left[\cosh^{-1}\left(\frac{x+iy}{f_o}\right)\right] \tag{4.67}$$

In order to carry out the operations efficiently and taking into account the chain rules associated with the above transformations, various first and second order differentiations are tabulated below.

$$\begin{aligned} c_x &= \frac{\partial u}{\partial x} & d_x &= \frac{\partial v}{\partial x} \\ c_y &= \frac{\partial u}{\partial y} & d_y &= \frac{\partial v}{\partial y} \\ c_{xy} &= \frac{\partial^2 u}{\partial x \partial y} & d_{xy} &= \frac{\partial^2 v}{\partial x \partial y} \end{aligned} \tag{4.68}$$

Note that the first order partial derivatives commute and $d_x = -c_y$ and $c_y = c_x$. The following shows the longitudinal component for the Ince polynomial series solutions for cosine and sine trigonometric functions and the even and odd indices for each series solutions. In the following solutions, the indices p, m are denoted as $2n$, $2k$ and $2n+1$, $2k+1$ for even and odd indices, respectively.

First, the cosine solution with even indices is given by [41]

$$E_{z,even}^{p,m}(\vec{r}) = \frac{iA}{k}\left(-2[ic_x S_p'^m(iu,\epsilon)C_m^p(v,\epsilon) - c_y S_{ip}^m(v,\epsilon)C_p^m(iu,\epsilon)] + \alpha C_p^m(iu,\epsilon)C_p^m(v,\epsilon)\right), \tag{4.69}$$

where

$$\alpha = \left(\frac{ikf(z)}{R(z)} - \frac{\epsilon}{2} \right) (c_x \sinh 2u + c_y \sin 2v), \tag{4.70}$$

and

$$E_{z,\,odd}^{p,m}(\vec{r}) = \frac{iA}{k} \left(2[ic_x C_p'^m(iu,\epsilon) S_m^p(v,\epsilon) - c_y C_p'^m(v,\epsilon) S_p^m(iu,\epsilon)] + \alpha S_p^m(iu,\epsilon) S_p^m(v,\epsilon) \right). \tag{4.71}$$

Constants are absorbed in A for Equations (4.69), (4.71), (4.72), (4.73), (4.78), (4.79), (4.82), and (4.83). For the odd indices [41]:

$$\begin{aligned} E_{z,\,even}^{p+1,m+1,e}(\vec{r}) = \frac{iA}{k} \Bigg(& -ic_x [2S_{p+1}'^{m+1}(iu,\epsilon) + S_{p+1}^{m+1}(iu,\epsilon)] C_{p+1}^{m+1}(v,\epsilon) \\ & + c_y [2S_{p+1}'^{m+1}(v,\epsilon) + S_{p+1}^{m+1}(v,\epsilon)] C_{m+1}^{p+1}(iu,\epsilon) + \alpha C_{p+1}^{m+1}(v,\epsilon) \Bigg) \end{aligned} \tag{4.72}$$

and

$$\begin{aligned} E_{z,\,odd}^{p+1,m+1}(\vec{r}) = \frac{i}{k} \Bigg(& -ic_x [2C_{p+1}'^{m+1}(iu,\epsilon) + C_{p+1}^{m+1}(iu,\epsilon)] S_{p+1}^{m+1}(v,\epsilon) \\ & + c_y [2C_{p+1}'^{m+1}(v,\epsilon) + C_{p+1}^{m+1}(v,\epsilon)] S_{m+1}^{p+1}(iu,\epsilon) + \alpha S_{p+1}^{m+1}(iu,\epsilon) S_{p+1}^{m+1}(v,\epsilon) \Bigg). \end{aligned} \tag{4.73}$$

The primed Ince polynomial functions are modified such that the coordinate r is absorbed as a factor in the series. For example,

$$S_{p+1}^{m'+1}(v,\epsilon) = \Sigma_{r=0}^{n} r B_r \sin(2r+1)v \tag{4.74}$$

and

$$C_p'^m(v,\epsilon) = \Sigma_{r=0}^{n} r A_r \cos 2rv. \tag{4.75}$$

The terms for the cross polarization component, E_y, are obtained by the same procedure, but the expressions are longer and require a second order modification to some of the Ince polynomials where each modified series has an extra factor of r^2.

$$S_{p+1}^{m''+1}(v,\epsilon) = \Sigma_{r=0}^{n} r^2 B_r \sin(2r+1)v \tag{4.76}$$

and

$$C_p^{''m}(v,\epsilon) = \Sigma_{r=0}^{n} r^2 A_r \cos 2rv. \tag{4.77}$$

Note that for any of the modified Ince polynomials, the first term ($r = 0$) is equal to zero.

Then, the cross polarization components for even indices are given by [41]

$$\begin{aligned} E_{y,\,even}^{p,m}(\vec{r}) = \frac{A}{m^2}\Bigg(& 4c_x c_y [C_p^{''m}(iu,\epsilon) C_p^m(v,\epsilon) + C_p^{''m}(v,\epsilon) C_p^m(iu,\epsilon)] \\ & + 2[c_{xy} S_p^{'m}(iu,\epsilon) C_p^m(v,\epsilon) - d_{xy} S_p^{'m}(v,\epsilon) C_p^m(iu,\epsilon)] + 4(c_y^2 - c_x^2) S_p^{'m}(iu,\epsilon) \\ & S_p^{'m}(v,\epsilon) + 2\beta S_p^{'m}(iu,\epsilon) C_p^m(v,\epsilon) + 2\gamma S_p^{'m}(v,\epsilon) C_p^m(iu,\epsilon) \\ & + \frac{\partial^2 \psi}{\partial x \partial y} C_p^m(iu,\epsilon) C_p^m(v,\epsilon)\Bigg) \end{aligned} \tag{4.78}$$

and

$$\begin{aligned} E_{y,\,odd}^{p,m}(\vec{r}) = \frac{A}{2k^2}\Bigg(& 4c_x c_y [i S_p^{''m}(iu,\epsilon) S_p^m(v,\epsilon) + S_p^{''m}(v,\epsilon) S_p^m(iu,\epsilon)] \\ & + 2[i c_{xy} C_p^{'m}(iu,\epsilon) S_p^m(v,\epsilon) + d_{xy} C_p^{'m}(v,\epsilon) S_p^m(iu,\epsilon)] + 4i(c_y^2 - c_x^2) C_p^{'m}(iu,\epsilon) \\ & C_p^{'m}(v,\epsilon) + 2i\chi C_p^{'m}(iu,\epsilon) S_p^m(v,\epsilon) - 2\gamma C_p^{'m}(v,\epsilon) S_p^m(iu,\epsilon) \\ & + \frac{\partial^2 \psi}{\partial x \partial y} S_p^m(iu,\epsilon) S_p^m(v,\epsilon)\Bigg) \end{aligned} \tag{4.79}$$

with

$$\chi = \left[\left(\frac{ikf(z)}{R(z)} - \frac{\epsilon}{2}\right)\left((c_y^2 - c_x^2)\sin 2v + 2c_x c_y \sinh 2u\right)\right]. \tag{4.80}$$

and,

$$\gamma = \left[\left(\frac{ikf(z)}{R(z)} - \frac{\epsilon}{2}\right)\left((c_y^2 - c_x^2)\sinh 2u - 2c_x c_y \sin 2v\right)\right]. \tag{4.81}$$

The cross polarization for the odd indices is [41],

$$\begin{aligned}
E_{y,\,even}^{p+1,m+1}(\vec{r}) = \frac{A_{pm}}{2k^2}\Bigg(&4c_x c_y[C_{p+1}^{''m+1}(iu,\epsilon)C_{p+1}^{m+1}(v,\epsilon) + C_{p+1}^{''m+1}(v,\epsilon)C_{p+1}^{m+1}(iu,\epsilon)] \\
&+ 4(c_y^2 - c_x^2)S_{p+1}^{'m+1}(iu,\epsilon)S_{p+1}^{m+1}(v,\epsilon) + (\beta + 2c_{xy})S_{p+1}^{'m+1}(iu,\epsilon) \\
&C_{p+1}^{m+1}(v,\epsilon) - (\gamma + 2d_{xy})S_{p+1}^{'m+1}(v,\epsilon)C_{p+1}^{m+1}(iu,\epsilon) + 4c_x c_y[C_{p+1}^{'m+1}(iu,\epsilon) \\
&C_{p+1}^{m+1}(v,\epsilon) + C_{p+1}^{'m+1}(v,\epsilon)C_{p+1}^{m+1}(iu,\epsilon)] + 2(c_x^2 - c_y^2)[S_{p+1}^{'m+1}(iu,\epsilon)S_{p+1}^{m+1}(v,\epsilon) \\
&+ S_{p+1}^{'m+1}(v,\epsilon)S_{p+1}^{m+1}(iu,\epsilon)] + (c_x^2 - c_y^2)S_{p+1}^{m+1}(iu,\epsilon)S_{p+1}^{m+1}(v,\epsilon) + (\beta + c_{xy}) \\
&S_{p+1}^{m+1}(iu,\epsilon)C_{p+1}^{m+1}(v,\epsilon) - (\gamma + d_{xy})S_{p+1}^{m+1}(v,\epsilon)C_{p+1}^{m+1}(iu,\epsilon) \\
&+ \left[2c_x c_y + \frac{\partial^2\psi}{\partial x \partial y}\right] C_{p+1}^{m+1}(iu,\epsilon)C_{p+1}^{m+1}(v,\epsilon)\Bigg)
\end{aligned} \tag{4.82}$$

and

$$E_{y,\,odd}^{p+1,m+1}(\vec{r}) = \frac{A_{pm}}{2k^2}\Bigg(4c_xc_y[S_{p+1}^{''m+1}(iu,\epsilon)S_{p+1}^{m+1}(v,\epsilon) + S_{p+1}^{''m+1}(v,\epsilon)S_{p+1}^{p+1}(iu,\epsilon)]$$

$$+ 4i(c_y^2 - c_x^2)C_{p+1}^{''m+1}(iu,\epsilon)C_{p+1}^{m+1}(v,\epsilon) + i(\beta + 2c_{xy})C_{p+1}^{'m+1}(iu,\epsilon)$$

$$S_{p+1}^{m+1}(v,\epsilon) + (\gamma + 2d_{xy})C_{p+1}^{'m+1}(v,\epsilon)S_{p+1}^{m+1}(iu,\epsilon) + 4c_xc_y[S_{p+1}^{'m+1}(iu,\epsilon)$$

$$S_{p+1}^{m+1}(v,\epsilon) + S_{p+1}^{'m+1}(v,\epsilon)S_{p+1}^{m+1}(iu,\epsilon)] + 2i(c_x^2 - c_y^2)[C_{p+1}^{'m+1}(iu,\epsilon)C_{p+1}^{m+1}(v,\epsilon) \tag{4.83}$$

$$+ C_{p+1}^{'m+1}(v,\epsilon)C_{p+1}^{m+1}(iu,\epsilon)] + i(c_x^2 - c_y^2)C_{p+1}^{m+1}(iu,\epsilon)C_{p+1}^{m+1}(v,\epsilon) + i(\beta + c_{xy})$$

$$C_{p+1}^{m+1}(iu,\epsilon)S_{p+1}^{m+1}(v,\epsilon) + (\gamma + c_{xy})C_{p+1}^{m+1}(v,\epsilon)S_{p+1}^{m+1}(iu,\epsilon)$$

$$+ \left[2c_xc_y + \frac{\partial^2\psi}{\partial x\partial y}\right] S_{p+1}^{m+1}(iu,\epsilon)S_{p+1}^{m+1}(v,\epsilon)\Bigg).$$

The second order partial derivative of ψ is

$$\frac{\partial^2\psi}{\partial x\partial y} = \frac{1}{4R(z)^2w(z)^4}\big[f(z)^2(2R(z) - ikw(z)^2)\big(f(z)^2(2R(z) - ikw(z)^2)$$

$$(c_y\sinh 2u - c_x\sin 2v)(c_x\sinh 2u - c_y\sin 2v) + 2R(z)w(z)^2 \tag{4.84}$$

$$(-2c_xc_y\cosh 2u - 2c_xc_ycps2v - c_{xy}\sinh 2u + d_{xy}\sin 2v)\big)\big]$$

considering the lowest order Gaussian mode.

The cross polarization expressions are more complicated though they contain linear combinations of the polynomials with similar orders as the longitudinal components. For cosine solutions, the number of hyperbolic nodal lines is $m+1$ and the number of hyperbolic nodal lines is m for sine solutions. Both solutions have the same number of elliptic nodal lines.

As the changes in ellipticity affect the dominant profiles of the IG beams, so are the longitudinal and cross components. In fact, Figure 4.8 below demonstrates that the IG mode, $p = 5$, $m = 3$, is elliptical and expected to be so for some nonzero and finite ϵ. But,

as ϵ approaches $0(\infty)$, all the components, dominant, cross and longitudinal, approach LG (HG) modes with circular (rectangular) symmetry. Figure (4.6) illustrates this trend as ellipticity is increased from approximately 0 to 50. Figure (4.7) shows more examples of the eccentricity variation for IG modes up to (3,3).

It is interesting that all the components of the field follow the same trend in the ellipticity variation. This is expected since as the dominant mode tends toward one of the extremes, it ought to have its other accompanying components follow suit. The fact that this does occur is reassuring in that the theory regarding the complete field and the HG, LG, and IG modes involved is consistent and complete.

4.4 IG properties

The expressions given for the cross and longitudinal components are long and complicated, but some insight can be gained from some of the terms within them. From the operation of differentiation, it is expected that the cross and longitudinal components are linear combinations of the same type of polynomials but with orders of $p+1, m+1$ and $p-1, m-1$ as well. First, for the longitudinal profiles, the even polynomials with odd indices have $m+1$ hyperbolic nodal lines and $(p-m)/2$ elliptic nodal lines. But, $p=m$ as a special case, has $p-1$ hyperbolic nodal lines. For even polynomials and even indices, it is still so that there are $m+1$ hyperbolic nodal lines and $(p-m)/2$ elliptic nodal lines including central axial nodal lines when appropriate. The odd polynomials follow a similar pattern. With even indices, the same number elliptic of nodal lines exist, but the number of hyperbolic nodal lines goes as $m-2$. For odd indices, the same pattern holds there now

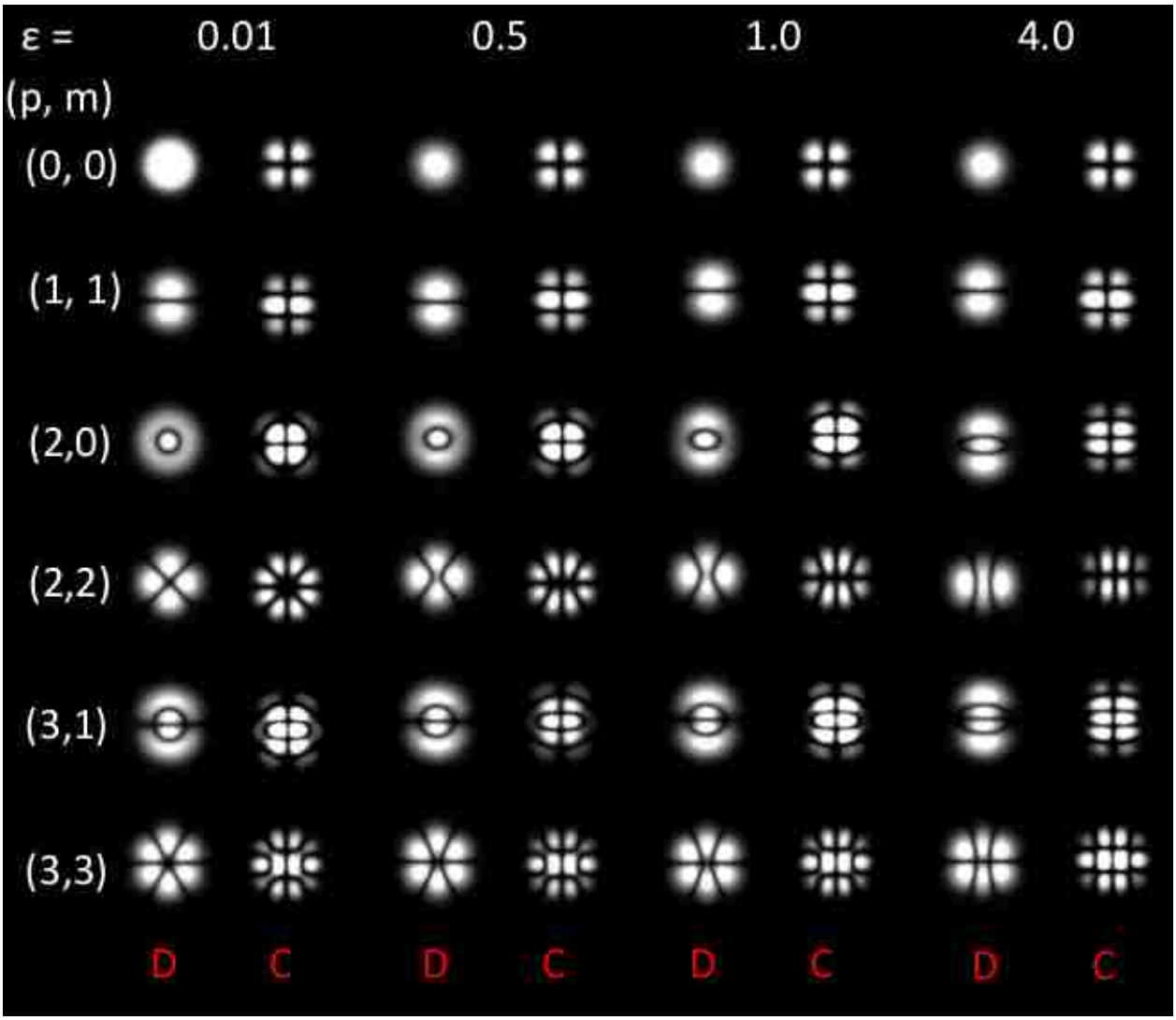

Figure 4.6: Chart of the IG modes studied showing the dominant and corresponding cross components with varying ellipticity. Note that the parity of the series solutions of each mode is the same parity as the indices. For example, an $IG_{2,2,c}$ uses the cosine series while $IG_{3,1,s}$ uses the sine series solution.

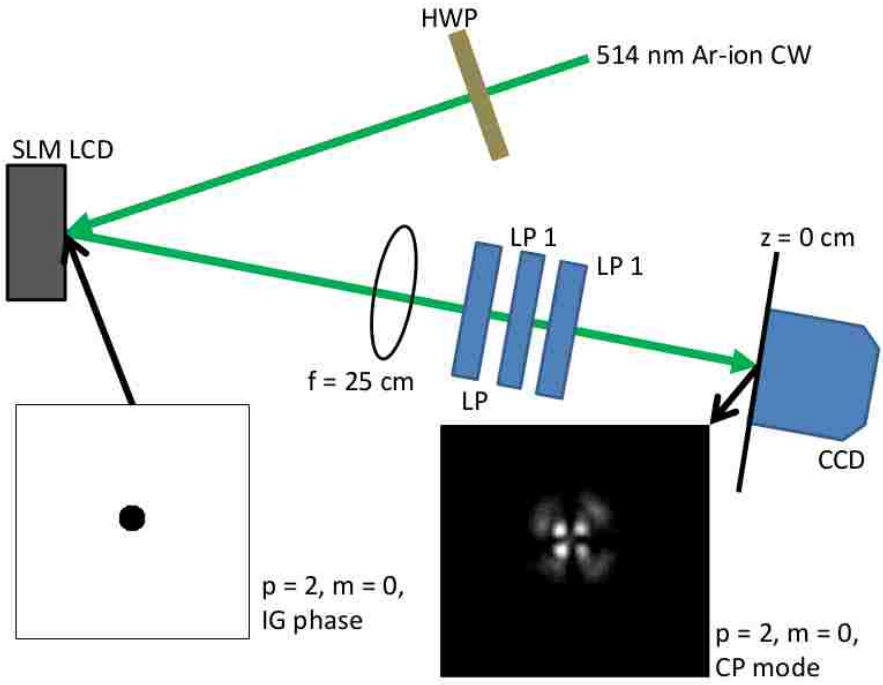

Figure 4.7: The experimental setup for dominant and cross polarization intensity observation.

being m hyperbolic nodal lines. Concerning the central irradiance nodal lines along the axes, the even-even case (polynomials to indices) has a vertical nodal line while the odd-odd case had a definite horizontal case including the odd-even case. The even-odd case, however, does not have any central nodal lines, only off-axis occurrences of elliptic and hyperbolic nodal lines.

4.5 Generation of IG modes

In this section, the experimental procedures for the measurement of the irradiance of the cross polarization profiles of Ince Gaussian beams is discussed. We start with a general overview of the experiment and also introduce the spatial light modulator (SLM) which is the principal device used in these experiments.

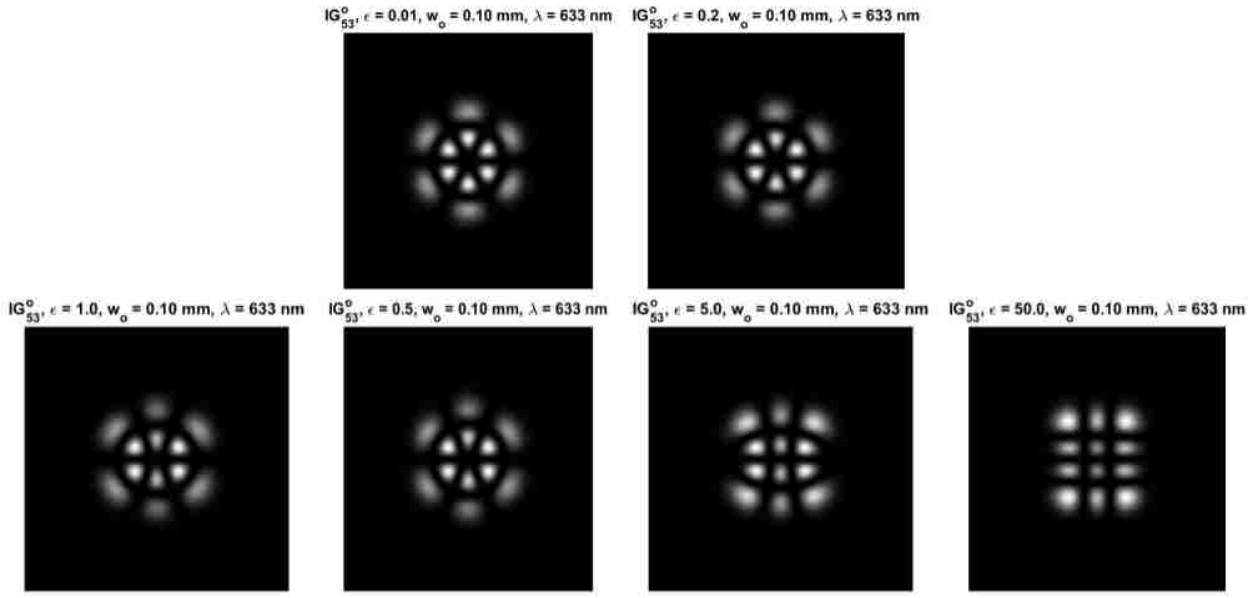

Figure 4.8: From zero ellipticity to an arbitrarily large one, the trend presented above demonstrates the behavior of the symmetry as the ellipticity varies.

4.5.1 IG phase generation of profiles

For the IG modes production, IG phases were calculated using Matlab's angle(A) function, where A is an n by n matrix with real or complex values. The function determines phases for each element as $A_{ij} = \arctan(x_i, y_j)$ where x_i and y_j are vector positions. The array generated by angle(A), call it P for phase, has single real entries for each A_{ij} and so it may be represented by an indexed color or grayscale scheme. Then, indexed image is converted to a 24 bit color image into RGB mode using Matlab's ind2rgb(P) function that produces the RGB windows bitmap format. The final product P_{RGB} is then uploaded to the SLM via the DVI-controller using Matlab_GUI.m. Phase profiles of the IG beams are all shown in Figures (4.4) and (4.5).

To obtain IG beam field amplitudes, a Matlab code written by Bandres et al [21], was used to calculate the IG complex profiles. The code is included in Appendix A.4. In

summary, their program, defined as a function, asks for Gaussian beam parameters k, λ, z propagation, etc. It also requests the user to choose the cosine or sine series and then the orders p and m. From the given inputs, the elliptic cylindrical coordinate system is constructed and the complex amplitude solutions of the IG modes are calculated following the procedure outlined in the current chapter. The resulting 512 by 512 array of complex values as the IG mode calculated is then subjected to the angle(A) function for an array of the same size but with real values with a range of $[0, \pi]$.

4.6 Observation of IG Cross polarization

4.6.1 Procedure

Similar to the Airy beam experiment, the amplitudes and phases were calculated using Matlab and then IG beams were produced using phase modulation with direct incidence on the SLM. The irradiance of the dominant components were observed using the CCD camera. Then, the intensities of the dominant (5.3) and cross polarizations, Equations (4.62) and (4.63), were calculated to see the expected profiles. These were compared to the experimental observations and the agreement was evident between experiment and theory. The next paragraph discusses the set up and procedure for the IG beam cross polarization experiment.

Production of Ince-Gauss (IG) beams first used a $\lambda = 514$ nm wavelength Ar-ion laser with linear polarization. Figure (4.9) shows the experimental setup which uses a configuration of direct incidence on the SLM. The diameter of the incident laser beam was 1 mm and it was incident on the spatial light modulator (SLM MeadowLark Optics Phase

only) LCD array (512 x 512 pixels or 7.68 mm x 7.68 mm). A two dimensional phase pattern from a single IG mode was uploaded to the SLM. The SLM model used for this experiment was different from the experiment in Chapter 3 in operating wavelength and response time of the LCD. Specifications for this model are given in Appendix B.

The incident power of the beam just before the SLM was 30 mW. The reflected beam from the SLM array, now modulated with the IG phase from the LCD was passed through a lens, $f = 25$ cm, at a distance f from the LCD array. Just behind the lens, a LP was placed with the transmission axis perpendicular to the incoming polarization orientation. This polarizer reduced intensity and also ensured that the polarization state of the beam to be analyzed was linearly polarized. At this point the dominant component is observable. Therefore, LP1 was placed behind LP with its transmission axis perpendicular to the first. Still, the dominant mode was present after passing through LP1. LP2 was then added and was allowed to have the transmission axis angle vary between $\alpha = 0°$ and 90° LP1 and LP2 acted as the crossed (transmission axes) pair to output the CP intensity where $\alpha = 90°$ degrees corresponds to the CP configuration and $\alpha = 0°$ degrees for the DP configuration. It was only after LP2 at $\alpha = 90°$ that the dominant mode was extinguished and the cross polarization mode was observable. A CCD was placed within 1 cm $> z > 0$ cm at a distance f behind the lens. For measuring the DP intensity, the transmission angle was changed from $\alpha = 90°$ to 0° degrees and the profile was recorded via CCD. A neutral density filter (ND = 6.0) was used to avoid CCD saturation. For CP intensity, the polarizer angle was set to $\alpha = 90°$ degrees and the profile recorded again via CCD. For DP and CP configurations, IG modes up to order $p = 5$ were recorded for ellipticities, $\epsilon = 0.01, 0.2, 1.0,$ and 2.0. The beam waist at $z = 0$ cm was 0.15 mm for a Rayleigh range, $z_R = 14$ cm.

4.7 Experimental Results and Dissusion

Figures (4.7) through (4.10) show the theoretical and experimental results for mode orders varying from $p = 1$ to $p = 5$. In each figure, the dominant polarization components exhibit the expected trend of the expected eccentricity variation. The exception is Figure (4.7) where the (1,1) mode is not effected at all by the change of eccentricity. Therefore, only a single observation is needed, and furthermore. This $IG_{1,1}$ mode is equivalent to an HG_{10} or HG_{01}. All the other modes in Figures (4.9) and (4.10) show the radially symmetric behavior transforming into rectangular symmetric intensity patterns (LG to HG modes). For Figure (4.9), the cross components obtained also agree with the expected results. However, as seen in the theoretical profile in Figure (4.8), some of the modes have cross components that change little as eccentricity is varied from 0 to 2.0. Though that may be the case, it is evident that the peaks present in the images do match the structures from theory.

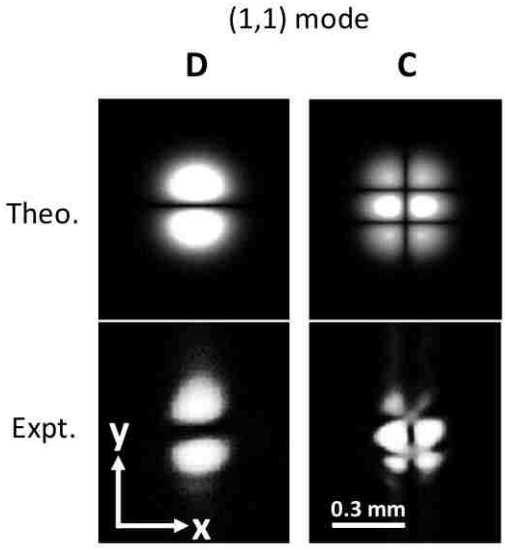

Figure 4.9: $IG_{1,1,s}$ not affected ellipticity variation due to the rectangular structure of the phase.

4.8 Results

The observations of the dominant and cross polarization intensities for the (p, m) IG modes from $p = 1$ to $p = 5$ agree with the expected simulated behavior as the eccentricity is varied from $\epsilon = 0.01$ to 2.0. As seen in simulation, the radial symmetry for ϵ near zero quickly transforms closer to rectangular symmetry just after $\epsilon = 1.0$. And, both polarization components follow the same trend.

Dominant polarization components near the extremes become LG and HG modes for $\epsilon = 0$ and ∞, respectively, as can be seen in Figures (4.9) and (4.10). Near these extremes, these dominant polarization components for HG and LG beams.

Polarization profiles recorded for IG modes by varying eccentricities demonstrate a few points. First, the prediction of the polarization profiles from Equations (1.30)-(1.32) have shown to be accurate. Second, the variation in eccentricity in observation and theory shows IG beams become exactly LG beams for zero ϵ and HG beams for infinite ϵ. Third, this relationship between IG, HG, and LG beams completes the theory of such higher order modes for Maxwell Polarization. The HG modes are different in that they are not superposed, but become the HG_{mn} amplitudes themselves.

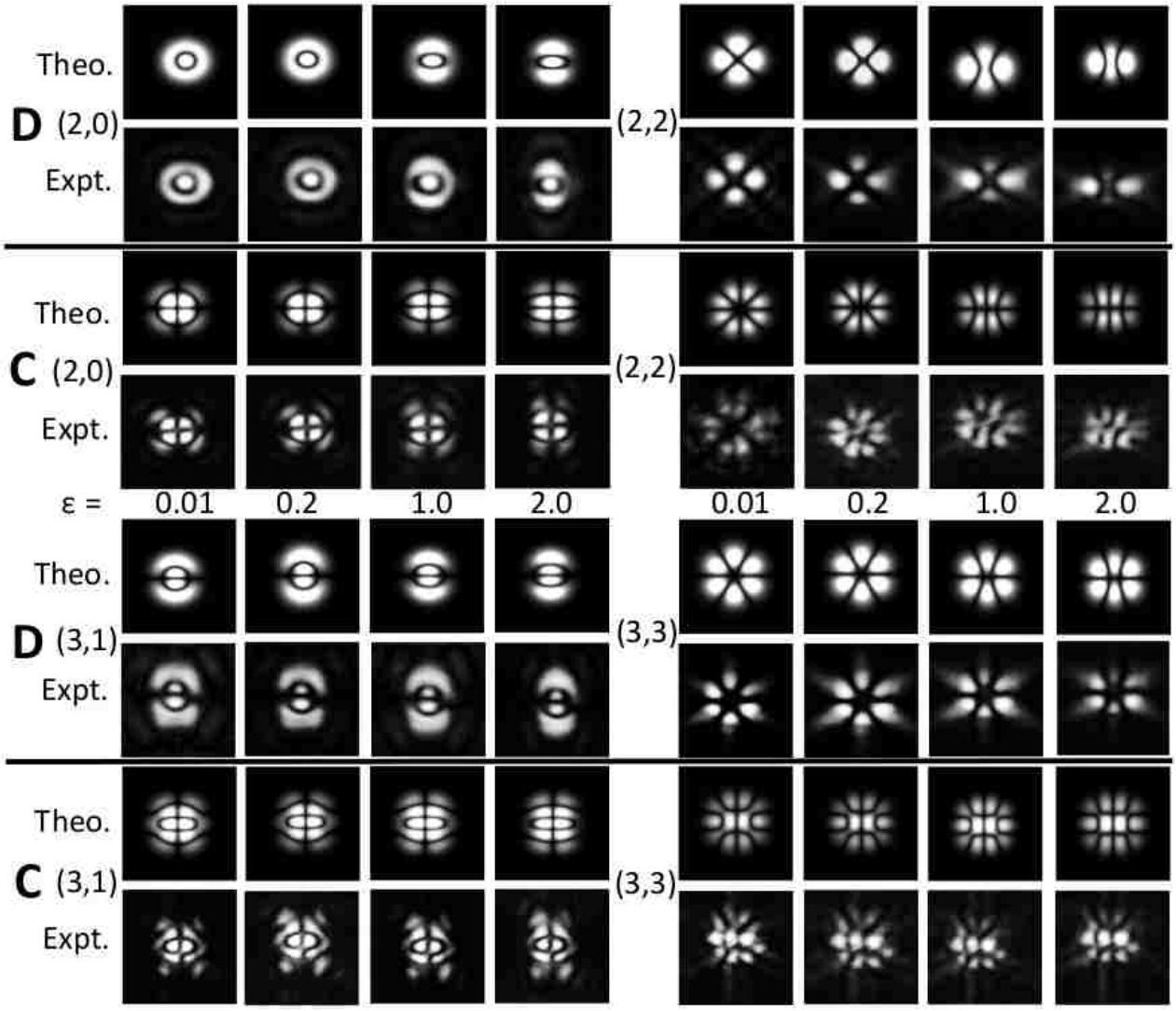

Figure 4.10: Table showing results of dominant and cross polarization profiles compared to theory. The modes studied are, again, those presented in the theoretical table in Figure (4.8).

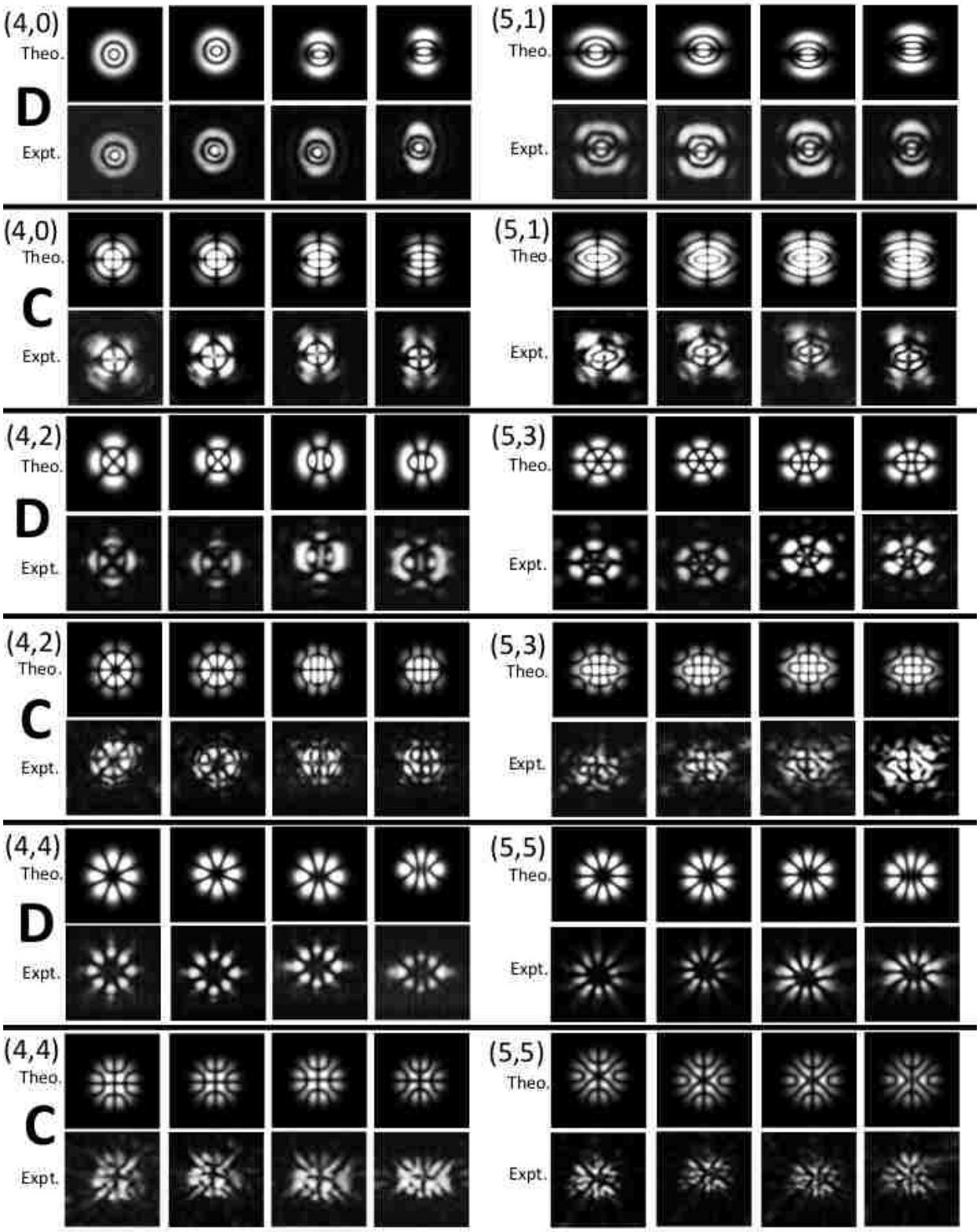

Figure 4.11: An extension of the table in Figure (4.9).

Chapter 5

Summary and Conclusion

5.1 Airy and Ince-Gauss Beam polarization

The polarization of Airy beams generated by diffracting a collimated fundamental Gaussian beam by an appropriately programmed SLM was investigated for values of truncation parameter, $a = 0.1, 0.2, 0.91$, and evolution of its polarization during propagation was studied. It is evident from Figures (3.13)-(3.15) that the experimental results confirm the theoretical predictions for both the dominant and cross polarizations intensities. Not only did those polarization profiles agree with those expected of Airy beams, but their trajectories also confirmed their nature as Airy beams as shown in Figure (3.12).

This experiment verified that the plane wave polarization description for the Airy beam is not adequate to fully characterize their polarization properties. What is needed is its corresponding polarization components that are obtained by Equations (1.30)-(1.32). Having all these components gives a more accurate, complete profile of the Airy beam.

5.2 Ince-Gauss polarization

The polarization of Ince-Guass beams generated by SLM diffraction for several modes was studied for varying values of the ellipticity parameter. Figures (4.9) and (4.10) show that the experiments confirm the theoretical predictions regarding their polarization structure for the intensity profiles of both the dominant and cross polarization components.

This experiment verified, as did the Airy beam experiment, that Equations (1.30)-(1.32) provide a more accurate, detailed description of the polarization of

Ince-Gauss beams. And, moreover, the variation of the ellipticity further confirms the connection between the HG and LG modes with the IG modes connecting the two extremes. This provides a more general and unified view for the well known HG and LG beams. The fact that ϵ may be varied as a continuous parameter means that an infinite number of possible modes that exist between HG and LG modes become accessible to experiments for possible applications.

5.3 Conclusion

In both experiments, it was shown that the plane wave polarization description for beams that are solutions to the PWE is not sufficient to accurately characterize a laser beam's polarization. Field components obtained by Equations (1.30)-(1.32) were demonstrated to exist for Airy beams [11] and Ince-Gauss beams [10]. Regarding the Airy beam, it is interesting to observe that its trajectory is non-linear even though a truncation of its infinite extent is imposed both for propagation and polarization description. As for the IG beams, this work provides support in that field solutions hold for varying ellipticities and even in the extreme cases that connect IG beams to LG and HG beams.

There is future work that can be done to extend this project such as studying self-healing of the cross polarization structures for the Airy and Ince-Gauss beams. Studies for self-healing of the Airy beam dominant component have been carried out as mentioned in Chapter 4. Since the cross polarization structure is a intimately connected to the dominant component by the relations (1.30)-(1.32), behavior similar of reconstructing itself is expected for the beam profile.

The polarization structure and its evolution with propagation of the helical IG beams can be studied. Also, the beams of linear combinations of LG or HG modes for arbitrary IG beams can be included as well as their cross polarization components. That is, the polarization structure of an arbitrary IG mode at the extreme values of the ellipticity can be investigated. This could potentially allow for a more general view of the polarization structure for any linear combinations of HG or LG modes in a laser beam.

In conclusion, this model of polarization should be considered since it is evident that any beam that satisfies the PWE has a Maxwell polarization profile. The lasers we use everyday affect all of our lives from the modern conveniences of internet communication to the discovery of ripples in space, gravity waves. And, as devices become increasingly smaller, as for example, in plasmonics, Maxwell polarization may need to be considered. Although, the paraxial wave approximation is sufficient for many applications, it is important to study the laser and understand its properties to improve its use in applications.

Bibliography

[1] A.L. Schawlow and C.H. Townes. Infrared and Optical Masers. Physical Review, 112(6):1940–1949, (1958).

[2] T.H. Maiman. Stimulated optical radiation in ruby. Nature, 187(4736):493–494, 1960.

[3] A. Einstein. Zur Quantentheorie der Strahlung. Physikalische Zeitschrift, 18:121–128, 1917.

[4] B. P. Abbott, R. Abbott, T. D. Abbott, M. R. Abernathy, F. Acernese, K. Ackley, C. Adams, T. Adams, P. Addesso, R. X. Adhikari, and et al. Observation of Gravitational Waves from a Binary Black Hole Merger. Physical Review Letters, 116(6):061102, February 2016.

[5] James Ira Thorpe. LISA-Laser Interferometer Space Antenna-NASA Home Page, 2018.

[6] A. E. Siegman. Lasers. University Science Books, Mill Valley, CA, 1986.

[7] W. L. Erikson and Surendra Singh. Polarization properties of Maxwell-Gaussian laser beams. Phys. Rev. E, 49:5778–5786, Jun 1994.

[8] Jessica Conry, Reeta Vyas, and Surendra Singh. Cross-polarization of linearly polarized Hermite–Gauss laser beams. J. Opt. Soc. Am. A, 29(4):579–584, Apr 2012.

[9] Jessica Conry, Reeta Vyas, and Surendra Singh. Polarization of orbital angular momentum carrying laser beams. J. Opt. Soc. Am. A, 30(5):821–824, May 2013.

[10] Sean Nomoto, Adam Goldstein, Reeta Vyas, and Surendra Singh. Polarization properties of Ince-Gaussian laser beams. J. Opt. Soc. Am. A, 34(12):2261–2265, Dec 2017.

[11] Sean Nomoto, A. Aadhi, Shashi Prabhakar, R. P. Singh, Reeta Vyas, and Surendra Singh. Polarization properties of the Airy beam. Opt. Lett., 40(19):4516–4519, Oct 2015.

[12] L. Novotny, M. R. Beversluis, K. S. Youngworth, and T. G. Brown. Longitudinal field modes probed by single molecules. Phys. Rev. Lett., 86:5251–5254, Jun 2001.

[13] Yuichi Kozawa and Shunichi Sato. Observation of the longitudinal field of a focused laser beam by second-harmonic generation. J. Opt. Soc. Am. B, 25(2):175–179, Feb 2008.

[14] Léo Turquet, Joona-Pekko Kakko, Lasse Karvonen, Hua Jiang, Esko Kauppinen, Harri Lipsanen, Martti Kauranen, and Godofredo Bautista. Probing the longitudinal electric field of bessel beams using second-harmonic generation from nano-objects. Journal of Optics, 19(8):084011, 2017.

[15] Handbook of Mathematical Functions. United States Department of Commerce, National Institute of Standards and Technology, 1964.

[16] J. Durnin, J. J. Miceli, and J. H. Eberly. Diffraction-free beams. Phys. Rev. Lett., 58:1499–1501, Apr 1987.

[17] C. P. Boyer, E. G. Kalnins, and W. Miller. Lie theory and separation of variables. 7. the harmonic oscillator in elliptic coordinates and ince polynomials. Journal of Mathematical Physics, 16(3):512–517, 1975.

[18] Angelina Müller, Matthias C. Wapler, and Ulrike Wallrabe. Segmented bessel beams. Opt. Express, 25(19):22640–22647, Sep 2017.

[19] Julio C. Gutiérrez-Vega and Miguel A. Bandres. Helmholtz–gauss waves. J. Opt. Soc. Am. A, 22(2):289–298, Feb 2005.

[20] J. C. Gutiérrez-Vega, M. D. Iturbe-Castillo, and S. Chávez-Cerda. Alternative formulation for invariant optical fields: Mathieu beams. Opt. Lett., 25(20):1493–1495, Oct 2000.

[21] Miguel A. Bandres and Julio C. Gutiérrez-Vega. Ince–gaussian beams. Opt. Lett., 29(2):144–146, Jan 2004.

[22] Airy Functions and Applications to Physics. Imperial College Press, 2004.

[23] G. A. Siviloglou, J. Broky, A. Dogariu, and D. N. Christodoulides. Observation of accelerating airy beams. Phys. Rev. Lett., 99:213901, Nov 2007.

[24] Miguel A. Bandres. Accelerating parabolic beams. Opt. Lett., 33(15):1678–1680, Aug 2008.

[25] M. V. Berry and N. L. Balazs. Nonspreading wave packets. American Journal of Physics, 47(3):264–267, 1979.

[26] J. E. Morris, M. Mazilu, J. Baumgartl, T. Čižmár, and K. Dholakia. Propagation characteristics of airy beams: dependence upon spatial coherence and wavelength. Opt. Express, 17(15):13236–13245, Jul 2009.

[27] Miguel A. Bandres and Julio C. Gutiérrez-Vega. Airy-gauss beams and their transformation by paraxial optical systems. Opt. Express, 15(25):16719–16728, Dec 2007.

[28] John Broky, Georgios A. Siviloglou, Aristide Dogariu, and Demetrios N. Christodoulides. Self-healing properties of optical airy beams. Opt. Express, 16(17):12880–12891, Aug 2008.

[29] G. A. Siviloglou, J. Broky, A. Dogariu, and D. N. Christodoulides. Ballistic dynamics

of airy beams. Opt. Lett., 33(3):207–209, Feb 2008.

[30] T. J. Eichelkraut, G. A. Siviloglou, I. M. Besieris, and D. N. Christodoulides. Oblique airy wave packets in bidispersive optical media. Opt. Lett., 35(21):3655–3657, Nov 2010.

[31] Chi-Young Hwang, Dawoon Choi, Kyoung-Youm Kim, and Byoungho Lee. Dual airy beam. Opt. Express, 18(22):23504–23516, Oct 2010.

[32] Yan Kaganovsky and Ehud Heyman. Airy pulsed beams. J. Opt. Soc. Am. A, 28(6):1243–1255, Jun 2011.

[33] Andrey V. Novitsky and Denis V. Novitsky. Nonparaxial airy beams: role of evanescent waves. Opt. Lett., 34(21):3430–3432, Nov 2009.

[34] D. G. Papazoglou, S. Suntsov, D. Abdollahpour, and S. Tzortzakis. Tunable intense airy beams and tailored femtosecond laser filaments. Phys. Rev. A, 81:061807, Jun 2010.

[35] Ido Dolev, Tal Ellenbogen, Noa Voloch-Bloch, and Ady Arie. Control of free space propagation of airy beams generated by quadratic nonlinear photonic crystals. Applied Physics Letters, 95(20):201112, 2009.

[36] Stefano Longhi. Airy beams from a microchip laser. Opt. Lett., 36(5):716–718, Mar 2011.

[37] Gil Porat, Ido Dolev, Omri Barlev, and Ady Arie. Airy beam laser. Opt. Lett., 36(20):4119–4121, Oct 2011.

[38] Zhuoyi Ye, Sheng Liu, Cibo Lou, Peng Zhang, Yi Hu, Daohong Song, Jianlin Zhao, and Zhigang Chen. Acceleration control of airy beams with optically induced refractive-index gradient. Opt. Lett., 36(16):3230–3232, Aug 2011.

[39] C.T. Rueden. Imagej2: Imagej for the next generation of scientific image data. `http://gts.sourceforge.net/`, 2017.

[40] Felix Arscott. Periodic Differential Equations. Permagon Press, 1964.

[41] Adam Goldstein. Transverse Profile and Polarization Properties of Lasers in Ince-Gaussian Modes(Unpublished bachelor's thesis). University of Arkansas, Fayetteville, AR, 2007.

Appendices

Appendix A: Computer Programs

A.1 SLM Interface

Matlab program “DVI_Matlab_GUI.m" written by BNS Non-linear Systems for interfacing with the SLM.

10pt

```
function varargout = DVI_Matlab_GUI(varargin)
% DVI_Matlab_GUI M-file for DVI_Matlab_GUI.fig
%      DVI_Matlab_GUI, by itself, creates a new DVI_Matlab_GUI or raises the existing
%      singleton*.
%
%      H = DVI_Matlab_GUI returns the handle to a new DVI_Matlab_GUI or the handle to
%      the existing singleton*.
%
%      DVI_Matlab_GUI('CALLBACK',hObject,eventData,handles,...) calls the local
%      function named CALLBACK in DVI_Matlab_GUI.M with the given input arguments.
%
%      DVI_Matlab_GUI('Property','Value',...) creates a new
```

```
   DVI_Matlab_GUI or raises the
%      existing singleton*.  Starting from the left, property
   value pairs are
%      applied to the GUI before DVI_Matlab_GUI_OpeningFunction
   gets called.  An
%      unrecognized property name or invalid value makes property
   application
%      stop.  All inputs are passed to DVI_Matlab_GUI_OpeningFcn
   via varargin.
%
%      *See GUI Options on GUIDE's Tools menu.  Choose "GUI allows
    only one
%      instance to run (singleton)".
%
% See also: GUIDE, GUIDATA, GUIHANDLES

% Edit the above text to modify the response to help
   DVI_Matlab_GUI

% Last Modified by GUIDE v2.5 16-Apr-2013 15:27:49

% Begin initialization code - DO NOT EDIT
```

```
gui_Singleton = 1;
gui_State = struct('gui_Name',       mfilename, ...
                   'gui_Singleton',  gui_Singleton, ...
                   'gui_OpeningFcn', @DVI_Matlab_GUI_OpeningFcn,
                      ...
                   'gui_OutputFcn',  @DVI_Matlab_GUI_OutputFcn,
                      ...
                   'gui_LayoutFcn',  [] , ...
                   'gui_Callback',   []);
if nargin && ischar(varargin{1})
    gui_State.gui_Callback = str2func(varargin{1});
end

if nargout
    [varargout{1:nargout}] = gui_mainfcn(gui_State, varargin{:});
else
    gui_mainfcn(gui_State, varargin{:});
end
% End initialization code - DO NOT EDIT

% --- Executes during object creation, after setting all
   properties.
```

```
function figure1_CreateFcn(hObject, eventdata, handles)
% hObject    handle to density (see GCBO)
% eventdata  reserved - to be defined in a future version of
   MATLAB
% handles    empty - handles not created until after all
   CreateFcns called

% Hint: edit controls usually have a white background, change
%       'usewhitebg' to 0 to use default.  See ISPC and COMPUTER.

% --- Executes just before DVI_Matlab_GUI is made visible.
function DVI_Matlab_GUI_OpeningFcn(hObject, eventdata, handles,
   varargin)
% This function has no output args, see OutputFcn.
% hObject    handle to fig ure
% eventdata  reserved - to be defined in a future version of
   MATLAB
% handles    structure with handles and user data (see GUIDATA)
% varargin   command line arguments to DVI_Matlab_GUI (see
   VARARGIN)

% Choose default command line output for DVI_Matlab_GUI
```

```
handles.output = hObject;
handles.inloop = false;
BNS_ReadLUT('C:\DVI_Matlab\LUT_Files\slm753_635.lut');

% Update handles structure
guidata(hObject, handles);

% --- Outputs from this function are returned to the command line.
function varargout = DVI_Matlab_GUI_OutputFcn(hObject, eventdata,
    handles)
% varargout  cell array for returning output args (see VARARGOUT);
% hObject    handle to figure
% eventdata  reserved - to be defined in a future version of
    MATLAB
% handles    structure with handles and user data (see GUIDATA)

% Get default command line output from handles structure
varargout{1} = handles.output;

%figure out where to put the image
handles.fig = figure(1);
a = get(0, 'MonitorPosition');
```

```
if(size(a,1) == 2)
    height = a(1,4);
else
    height = a(4);
end
rect = [0-85, height - 512 - 83, 512+147, 512+147];
set(handles.fig , 'MenuBar', 'none',...
                  'Toolbar', 'none',...
                  'Renderer', 'opengl',...
                  'Position', rect);
%read int he image, and load it to the proper window
Data = zeros(512,512,3);
image(Data);
axis off;
axis image;

% Update handles structure
guidata(hObject, handles);

% --- Executes when user attempts to close figure1.
function figure1_CloseRequestFcn(hObject, eventdata, handles)
% hObject    handle to figure1 (see GCBO)
```

```
% eventdata  reserved - to be defined in a future version of
   MATLAB
% handles    structure with handles and user data (see GUIDATA)

if (handles.inloop == false)
    %delete the figure that holds the SLM data
    delete(handles.fig)
    % Hint: delete(hObject) closes the figure
    delete(hObject);
end

% --- Executes on clicking DisplayOnSLM checkbox
function DisplayOnSLM_Callback(hObject, eventdata, handles)

%calculate where the image should be
a = get(0, 'MonitorPosition');
if(size(a,1) == 2)
    width = a(1,3);
    height = a(1,4);
else
    width = a(3);
    height = a(4);
```

```
end

OnSLM = get(hObject,'Value');

if(OnSLM)
    rect = [width-85, height - 512 - 83, 512+147, 512+147];
    set(handles.fig , 'MenuBar', 'none',...
     'Toolbar', 'none',...
     'Renderer', 'opengl',...
     'Position', rect);
else
    rect = [0-85, height - 512 - 83, 512+147, 512+147];
    set(handles.fig , 'MenuBar', 'none',...
     'Toolbar', 'none',...
     'Renderer', 'opengl',...
     'Position', rect);
end

% ---- Executes on selection change in ImageListbox.
function ImageListbox_Callback(hObject, eventdata, handles)
% hObject    handle to ImageListbox (see GCBO)
% eventdata  reserved - to be defined in a future version of
```

MATLAB

```
% handles    structure with handles and user data (see GUIDATA)


% Hints: contents = get(hObject,'String') returns ImageListbox
    contents as cell array
%        contents{get(hObject,'Value')} returns selected item from
     ImageListbox


% figure out which image is selected int he listbox, and send that
     image
% data to the figure window
SelectedImage = get(hObject,'String');
Selection = get(hObject,'Value');


%figure out where to put the image
% handles.fig = figure(1);
a = get(0, 'MonitorPosition');
if(size(a,1) == 2)
     width = a(1,3);
     height = a(1,4);
else
     width = a(3);
```

```
    height = a(4);
end
OnSLM = get(handles.DisplayOnSLM,'Value');
if(OnSLM)
    rect = [width-85, height - 512 - 83, 512+147, 512+147];
    set(handles.fig , 'MenuBar', 'none',...
        'Toolbar', 'none',...
        'Renderer', 'opengl',...
        'Position', rect);
else
    rect = [0-85, height - 512 - 83, 512+147, 512+147];
    set(handles.fig , 'MenuBar', 'none',...
        'Toolbar', 'none',...
        'Renderer', 'opengl',...
        'Position', rect);
end

%read int he image, and load it to the proper window
Data = imread(char(SelectedImage(Selection)) ,'bmp');
Data = BNS_ProcessLUT(handles, Data);
image(Data);
axis off;
```

```
axis image;


% Update handles structure
guidata(hObject, handles);


% --- Executes during object creation, after setting all
    properties.
function ImageListbox_CreateFcn(hObject, eventdata, handles)
%function figure1_CreateFcn(hObject, eventdata, handles)
% hObject    handle to ImageListbox (see GCBO)
% eventdata  reserved - to be defined in a future version of
    MATLAB
% handles    empty - handles not created until after all
    CreateFcns called


% Hint: listbox controls usually have a white background on
    Windows.
%       See ISPC and COMPUTER.
if ispc && isequal(get(hObject,'BackgroundColor'), get(0,'
    defaultUicontrolBackgroundColor'))
     set(hObject,'BackgroundColor','white');
end
```

```
% ---- Executes on button press in StartStopButton.
function StartStopButton_Callback(hObject, eventdata, handles)
% hObject    handle to StartStopButton (see GCBO)
% eventdata  reserved - to be defined in a future version of
   MATLAB
% handles    structure with handles and user data (see GUIDATA)

%pre-read in the images
SelectedImage = get(handles.ImageListbox,'String');
Path = char(SelectedImage(1));
Data1 = imread(Path,'bmp');
Data1 = BNS_ProcessLUT(handles, Data1);
Path = char(SelectedImage(2));
Data2 = imread(Path,'bmp');
Data2 = BNS_ProcessLUT(handles, Data2);

%loop through the images 5 times
% handles.fig = figure(1);
handles.inloop = true;
guidata(hObject,handles);
for loop = 1:40
```

```
    for index = 1:2
            if(index == 1)
                image(Data1);
                axis off;
                axis image;
            else
                image(Data2);
                axis off;
                axis image;
            end
            pause(0.05);
    end
end
handles.inloop = false;
guidata(hObject,handles);

function BNS_ReadLUT(LUTPath)
global LUT;

LUT = dlmread(LUTPath, ' ');

function Image = BNS_ProcessLUT(handles, Image)
```

```
global LUT;

d = size(Image);

for i = 1:d(1) %First dimension of image
    for j = 1:d(2) %Second dimension of image
        pixel = bitshift(uint16(Image(i, j, 2)), 8) + uint16(Image
            (i, j, 1));
        pixel = LUT(pixel + 1, 2);
        t = typecast(uint16(pixel), 'uint8');
        Image(i, j, 1) = t(1);
        Image(i, j, 2) = t(2);
    end
end

% ---- If Enable == 'on', executes on mouse press in 5 pixel border
    .
% ---- Otherwise, executes on mouse press in 5 pixel border or over
    ImageListbox.

% hObject    handle to ImageListbox (see GCBO)
% eventdata  reserved - to be defined in a future version of
```

```
    MATLAB
% handles    structure with handles and user data (see GUIDATA)


% --- If Enable == 'on', executes on mouse press in 5 pixel border
    .
% --- Otherwise, executes on mouse press in 5 pixel border or over
     ImageListbox.
function ImageListbox_ButtonDownFcn(hObject, eventdata, handles)
% hObject    handle to ImageListbox (see GCBO)
% eventdata  reserved - to be defined in a future version of
    MATLAB
% handles    structure with handles and user data (see GUIDATA)


% --- Executes during object deletion, before destroying
    properties.
function ImageListbox_DeleteFcn(hObject, eventdata, handles)
% hObject    handle to ImageListbox (see GCBO)
% eventdata  reserved - to be defined in a future version of
    MATLAB
% handles    structure with handles and user data (see GUIDATA)


% --- Executes on key press with focus on ImageListbox and none of
```

```
    its controls.
function ImageListbox_KeyPressFcn(hObject, eventdata, handles)
% hObject    handle to ImageListbox (see GCBO)
% eventdata  structure with the following fields (see UICONTROL)
%       Key: name of the key that was pressed, in lower case
%       Character: character interpretation of the key(s) that was
    pressed
%       Modifier: name(s) of the modifier key(s) (i.e., control,
   shift) pressed
% handles    structure with handles and user data (see GUIDATA)
```

A.2 Airy beam mask

Matlab program “Airymask.m" written by the author for production of Airy beam phase masks for use on the SLM device.

```
   10pt
%Airymask.m produces the sinusoidal blazed diffraction grating to
   produce
%  Airy beams.  Equation for phase based on formula from
%               Gil Porat, Ido Dolev, Omri Barlev, and Ady Arie.
%               Airy beam laser. Opt. Lett., 36(20):4119-4121,
   Oct 2011.
%  Period spacing grating controlled with lambda
```

```
%  xp and yp control the amount of cubic curvature in the phase
   and hence
%  they control the truncation parameter 'a'

% spatial parameters
N = 512;  %  SLM LCD array dimension for BNS model 512
x = linspace(-2.5,2.5,N);  %1mm for ~7 mm side length
y = linspace(-2.5,2.5,N);
[X Y] = meshgrid(x,y);  % coordinate grid for LCD array pixels

% polar coords
RHO = sqrt(X.^2+Y.^2);
PHI = atan2(Y,X);

% function parameters
xp = 0.5;
yp = 0.5;
lambda = 50;

theta = (X./xp).^3 + (Y./yp).^3 ;   % compute the cubic phase
phase = mod(cos(theta + lambda.*X),pi);  % compute the entire
   phase grating
```

```
imwrite(phase,'Airymask.bmp','bmp'); %write the grating to a bmp
    file

figure();   % open image of the phase in new figure
imshow(phase);  % display the computed phase
```

A.3 Airy beam Intensity

Excerpt from a Mathematica program "AiryCalRVnew.nb" written by Reeta Vyas to simulate Airy beam intensity and its evolution with propagation. Edits by the author have been made to include a values for the experiment in Chapter 3.

```
   10pt
z = 3;
(*For[i = 1,i<7,i++;*)\[Lambda] = 632.8*10^-9; k = (
 2 \[Pi]) /\[Lambda];
delx = 0;(*-0.0015;*)
dely = 0;(*  -0.0015;*)\
x0 = 0.00022; y0 = x0;(*0.00021 for R0005 a = .1246works at 3m*)
a = 0.16; cont = 200;(*R0008 x0=0.00017; a=0.2919; at 1.5m not
    from \
center*)
(*R0008 a = .2919 x0 0.000145 at .75m*)
```

```
(*z=0;*)


xm = 3.62*10^-3; ym = xm;
EF = Exp[(a (x - delx)/x0 - a/2 (z/(k*x0^2))^2 - I/12 (z/(k*x0^2))
    ^3 +
         I (a^2  z)/(2 k*x0^2) + I ((x - delx)* z)/(2 x0^3 k) )]*
    Exp[(a (y - dely)/y0 - a/2 (z/(k*y0^2))^2 - I/12 (z/(k*y0^2))^3
        +
        I (a^2  z)/(2 k*y0^2) + I ((y - dely)* z)/(2 y0^3 k)) ] *
    AiryAi[((x - delx)/x0 - (z/(2*k*x0^2))^2 + I *(a*z)/(k*x0^2))]*
    AiryAi[((y - dely)/y0 - (z/(2*k*y0^2))^2 + I *(a*z)/(k*y0^2))];
f1 = EF; f2 = D[EF, x, y]; (*f3=D[EF,x];*)
i1 = Conjugate[f1]*f1; i2 = Conjugate[f2]*f2;(*i3=Conjugate[f3]*f3
    ;*)


a0 = ContourPlot[i1,  {x, -xm, xm}, {y, -ym, ym},
    ContourLines -> False, Contours -> cont,
    PlotRange -> All,(*PlotRangeClipping\[Rule] True,*)
    ImageSize -> Large, Frame -> False, Axes -> False,
    ColorFunction -> "GrayTones"];
b0 = ContourPlot[i2,  {x, -xm, xm}, {y, -ym, ym},
    ContourLines -> False, Contours -> cont, PlotRange -> All,
```

```
    ImageSize -> Large, Frame -> False, Axes -> False,
    ColorFunction -> "GrayTones"];
(*GraphicsGrid[{{a0,b0}},Spacings\[Rule](*Scaled[-0.05]*)]*)
Print[a0];
Print[b0];(*z = z +0.1;]*)
```

A.4 IG mode amplitudes and phases

Matlab program "Ince_Gaussian.m" written by M. Bandres for computing IG mode amplitudes and phases. Output from this program was plotted using "iggyplotter.m" written by the author. Plots from this program produce phase plots as bitmap files for SLM phase modulation.

```
   10pt
function [IGB,X,Y]=Ince_Gaussian(L,N,parity,p,m,e,w0,k,z)
%{
Calculate an Ince-Gaussian Beam at a given z plane

INPUTS:
    L = transverse physical size of the X-Y space [-L,L,-L,L]
    N = number of sampling points (must be ODD)
    parity = parity of the beam, 0 = EVEN  C;  1 = ODD  S
    p, m = order and degree of the Ince Gaussian beam
           p=0,1,2,3,... for parity=0 and p=1,2,3,.. for parity=1
```

```
        0<=m<=p

        (p,m) must have the same parity, i.e., (-1)^(p-m)=1

    e = ellipticity parameter

    w0 = beam width(waist) at z=0

    k = 2*pi/lambda, wavenumber, lambda=wavelength

    z = propagation distance
```

OUTPUTS:

```
    IGB = Ince Gaussian Beam (Intensity is analytically normalized
        to 1, i.e., Integral(|IGB|^2)=1)

    X and Y = space matrices
```

EXAMPLE:

```
        [IGB,X,Y]=Ince_Gaussian(15e-3,501,0,6,2,2,3e-3,(2*pi/632.8
            e-9),0); figure;

        surf(X,Y,abs(IGB)); shading interp; lighting phong; view
            (2); axis tight; axis equal; xlabel('x','Fontsize',12);
             ylabel('y','Fontsize',12); title('Ince Gausssian Beam'
            ,'Fontsize',12)

        dx=abs(X(2,2)-X(2,1));

        Normalization=sum(sum(IGB.*conj(IGB))).*dx^2;
```

For more information about Ince Gaussian Beams:

"Ince-Gaussian beams," Miguel A. Bandres and J. C. Gutierrez-Vega
Optics Letters, 29(2), 144-146 (2004) (http://goo.gl/U18mol)

"Ince-Gaussian modes of the paraxial wave equation and stable resonators," Miguel A. Bandres and Julio C. Gutierez-Vega
Journal of the Optical Society of America A, 21(5), 873-880 (2004) (http://goo.gl/rqq7nQ)

"Observation of Ince-Gaussian modes in stable resonators," Ulrich T. Schwarz, Miguel A. Bandres and Julio C. Gutierrez-Vega
Optics Letters, 29(16), 1870-1872 (2004) (http://goo.gl/7lkSb4)

AUTHOR: Miguel A. Bandres
URL: www.mabandres.com
%}

%% CHECK INPUT

```
if mod(N,2)==0;        error('ERROR: N must be ODD'); end;
if parity==0
    if (m<0)||(m>p); error('ERROR: Wrong range for "m", 0<=m<=p');
        end;
else
    if (m<1)||(m>p); error('ERROR: Wrong range for "m", 1<=m<=p');
        end;
end;
if (-1)^(m-p)~=1;      error('ERROR: (p,m) must have the same parity
    , i.e., (-1)^(m-p)=1');  end;

%% PARAMETERS
f0 = sqrt(e/2)*w0; % Focal distance of elliptic coordinates at z=0

%% INCE GAUSSIAN BEAM
if z==0 % At the z=0
    [xhi,etha,X,Y]=mesh_elliptic(f0,L,N); % Calculate elliptic
        coordinates (xhi,etha), (X,Y)= Cartesian Coordinates
    R = sqrt(X.^2 + Y.^2);                % Radial coordinate
    if parity==0
        IGB=CInceIGB(p,m,e,etha).*CInceIGB(p,m,e,1i*xhi).*exp(-(R/w0
            ).^2);  % Even IGB
```

```
    else
        IGB=SInceIGB(p,m,e,etha).*SInceIGB(p,m,e,1i*xhi).*exp(-(R/w0
            ).^2);  % Odd IGB
    end
else % At z~=0
    zr=1/2*k*w0^2;              % Rayleigh range
    wz=w0*sqrt(1+(z/zr).^2);    % Beam width(waist) at z=0
    Rz=z*(1+(zr./z).^2);        % Radius of curvature of the phase
        front
    f = f0*wz/w0;               % Focal distance of elliptic
        coordinates at z
    [xhi,etha,X,Y]=mesh_elliptic(f,L,N); % Calculate elliptic
        coordinates (xhi,etha), (X,Y)= Cartesian Coordinates
    R = sqrt(X.^2 + Y.^2);      % Radial coordinate
    if parity==0
        IGB=(w0/wz)*(CInceIGB(p,m,e,etha).*CInceIGB(p,m,e,1i*xhi)).*
            exp(-(R/wz).^2).* ...
            exp(1i*(k*z + k*R.^2/(2*Rz)-(p+1)*atan(z/zr)));     % Even
                IGB
    else
        IGB=(w0/wz)*(SInceIGB(p,m,e,etha).*SInceIGB(p,m,e,1i*xhi)).*
            exp(-(R/wz).^2).* ...
```

```
        exp(1i*(k*z + k*R.^2/(2*Rz)-(p+1)*atan(z/zr)));      % Odd
            IGB
    end
end

%% COMPUTE THE NORMALIZATION CONSTANTS
if parity == 0;
    if mod(p,2)==0;
        [C0,~,coef]=CInceIGB(p,m,e,0);
        [Cp,~,~]=CInceIGB(p,m,e,pi/2);
        Norm = (-1)^(m/2)*sqrt(2)*gamma(p/2+1)*coef(1) *sqrt(2/pi)/
            w0/C0/Cp;  % Calculate normalization constant
    else
        [C0,~,coef]=CInceIGB(p,m,e,0);
        [~,~,~,DCp]=CInceIGB(p,m,e,pi/2);
        Norm = (-1)^((m+1)/2) * gamma((p+1)/2+1) * sqrt(4*e/pi) *
            coef(1) / w0 / C0 / DCp; % Calculate normalization
            constant
    end
else
    if mod(p,2)==0;
        [~,~,coef,dS0]=SInceIGB(p,m,e,0);
```

```
        [~,~,~,dSp]=SInceIGB(p,m,e,pi/2);
        Norm = (-1)^(m/2)*sqrt(2)*e*gamma((p+2)/2+1)*coef(1) *sqrt
            (2/pi)/w0/ dS0 / dSp;  % Calculate normalization constant
    else
        [Sp,~,coef,~]=SInceIGB(p,m,e,pi/2);
        [~,~,~,dS0]=SInceIGB(p,m,e,0);
        Norm = (-1)^((m-1)/2) * gamma((p+1)/2+1) * sqrt(4*e/pi) *
            coef(1) / w0 / Sp / dS0;  % Calculate normalization
            constant
    end
end

IGB = IGB*Norm; % Normalized the IGB to Integral(|IGB|^2)=1

return



%% SUBFUNCTIONS

%% Elliptic Coordinates
function [xi,eta,X,Y]=mesh_elliptic(f,L,N)
%{
```

```
Creates an elliptic coordinate mesh of size 2Lx2L with N points

INPUT:

    f = focal distance of elliptical coordinates

    L = spatial size of the mesh, i.e., [-L,L]x[-L,L]

    N = ODD number of discrete points in the mesh. Must be ODD.

OUPUT:

    xi  = elliptic coordinate mesh

    eta = eta elliptic coordinate mesh

    X   = x-Cartesian coordinate mesh

    Y   = y-Cartesian coordinate mesh
%}

%% Cartesian Coordinates
[X,Y]=meshgrid(linspace(-L,L,N));

%% Elliptic Coordinates
xi=zeros(N); eta=zeros(N);  % Initialization

% Calculate First Quadrant
en = acosh((X(1:(N+1)/2,(N+1)/2:N)+1i*Y(1:(N+1)/2,(N+1)/2:N))/f);
```

```
ee = real(en);
nn = imag(en);
nn = nn + (nn<0)*2*pi;
xi(1:(N+1)/2,(N+1)/2:N)=ee;
eta(1:(N+1)/2,(N+1)/2:N)=nn;

% Calculate other quadrants by symmetry
xi(1:(N+1)/2 , 1:(N-1)/2)=fliplr(xi(1:(N+1)/2,(N+3)/2:N));
xi((N+3)/2:N,1:N)=flipud(xi(1:(N-1)/2,1:N));
eta(1:(N+1)/2,1:(N-1)/2)=pi-fliplr(eta(1:(N+1)/2,(N+3)/2:N));
eta((N+3)/2:N,1:N)=pi+rot90((eta(1:(N-1)/2,1:N)),2);

return

%% EVEN Ince Polynomial
function [IP,eta,coef,dIP]=CInceIGB(p,m,q,z)
%{
This function calculates the EVEN Ince polynomials which are
   solutions of the Ince equation.
The Ince equation is a periodic linear second-order differential
   equation that has two families of independent solutions,
namely, the even C^{m}_p(z,q) and odd S^{m}_p(z,q) Ince
```

```
   polynomials of order p and degree m.
Physical considerations are such that Ince polynomials are
   periodic with period 2p. The values of \etha that satisfy this
   condition
are the eigenvalues of the Ince equation which is given by


d^2F/dz^2 + q*sin(2z)dF/dz+(\eta-p*q*cos(2z))*F=0


where
0<=z<2pi
p=0,1,2,3,...
q=complex parameter
\etha = eigenvalue of the Ince equation.


INPUTS:
     p=0,1,2,3... Order of Ince polynomial
     0<=m<=p      m is the degree of the Ince polynomial
     (p,m) must have the same parity, i.e., (-1)^(p-m)=1
     q = complex parameter
     0<=z<2pi     independent variable (Vector or Matrix)


OUTPUTS:
```

```
    IP=C^{m}_p(z,q) EVEN Ince Polynomial
    eta  = eigenvalue of the Ince Polynomial
    coef = coefficients of the Ince Polynomial
    dIP  = derivative of the Ince Polynomial

For more information about Ince Polynomial:

    Miguel A. Bandres and Julio C. Gutiérrez-Vega, "Ince-Gaussian
       modes of the paraxial wave equation and stable resonators"
    Journal of the Optical Society of America A, 21(5), 873-880
       (2004) ( http://goo.gl/rqq7nQ )

AUTHOR: Miguel A. Bandres
URL:    www.mabandres.com
%}

%% Check Input
if (m<0)||(m>p); error('ERROR: Wrong range for "m", 0<=m<=p'); end
   ;
if (-1)^(m-p)~=1;   error('ERROR: (p,m) must have the same parity,
    i.e., (-1)^(m-p)=1');  end;
[largo,ancho]=size(z); % change input to vector format
```

```
z=transpose(z(:));
normalization=1;

%% Calculate the Coefficients
if mod(p,2)==0
    %%%% p Even %%%%
    j=p/2;   N=j+1;   n=m/2+1;

    % Matrix
    M=diag(q*(j+(1:N-1)),1) + diag([2*q*j,q*(j-(1:N-2))],-1) +
        diag([0,4*((0:N-2)+1).^2]);
    if p==0; M=0; end;

    % Eigenvalues and Eigenvectors
    [A,ets]=eig(M);
    ets=diag(ets);
    [ets,index]=sort(ets);
    A=A(:,index);

    % Normalization
    if normalization==0;
        N2=2*A(1,n).^2+sum(A(2:N,n).^2);
```

```
        NS=sign(sum(A(:,n)));
        A=A/sqrt(N2)*NS;
    else
        mv=(2:2:p).';
        N2=sqrt(A(1,n)^2*2*gamma(p/2+1)^2+sum((sqrt(gamma((p+mv)
            /2+1).*gamma((p-mv)/2+1)  ).*A(2:p/2+1,n)).^2  ));
        NS=sign(sum(A(:,n)));
        A=A/N2*NS;
    end

    % Ince Polynomial
    r=0:N-1;
    [R,X]=meshgrid(r,z);
    IP=cos(2*X.*R)*A(:,n);
    dIP=-2*R.*sin(2*X.*R)*A(:,n);
    eta=ets(n);

else
    %%%% p ODD %%%
    j=(p-1)/2;   N=j+1;   n=(m+1)/2;

    % Matrix
```

```
M=diag(q/2*(p+(2*(0:N-2)+3)),1)+diag(q/2*(p-(2*(1:N-1)-1)),-1)
    + diag([q/2+p*q/2+1,(2*(1:N-1)+1).^2]);

% Eigenvalues and Eigenvectors
[A,ets]=eig(M);
ets=diag(ets);
[ets,index]=sort(ets);
A=A(:,index);

% Normalization
if normalization==0;
   N2=sum(A(:,n).^2);
   NS=sign(sum(A(:,n)));
   A=A/sqrt(N2)*NS;
else
    mv=(1:2:p).';
    N2=sqrt(sum( ( sqrt(gamma((p+mv)/2+1).*gamma((p-mv)/2+1) )
        .*A(:,n)).^2 ));
    NS=sign(sum(A(:,n)));
    A=A/N2*NS;
end
```

```
    % Ince Polynomial
    r=2*(0:N-1)+1;
    [R,X]=meshgrid(r,z);
    IP=cos(X.*R)*A(:,n);
    dIP=-R.*sin(X.*R)*A(:,n);
    eta=ets(n);
end

coef=A(:,n);
IP=reshape(IP,[largo,ancho]); % reshape output to original format
dIP=reshape(dIP,[largo,ancho]);

return

%% ODD Ince Polynomial
function [IP,eta,coef,dIP]=SInceIGB(p,m,q,z)
%{
This function calculates the ODD Ince polynomials which are
   solutions of the Ince equation.
The Ince equation is a periodic linear second-order differential
   equation that has two families of independent solutions,
namely, the even C^{m}_p(z,q) and odd S^{m}_p(z,q) Ince
```

```
   polynomials of order p and degree m.
Physical considerations are such that Ince polynomials are
   periodic with period 2p. The values of \etha that satisfy this
   condition
are the eigenvalues of the Ince equation which is given by


d^2F/dz^2 + q*sin(2z)dF/dz+(\eta-p*q*cos(2z))*F=0


where
0<=z<2pi
p=0,1,2,3,...
q=complex parameter
\etha = eigenvalue of the Ince equation.


INPUTS:
     p=0,1,2,3... Order of Ince polynomial
     0<=m<=p      m is the degree of the Ince polynomial
     (p,m) must have the same parity, i.e., (-1)^(p-m)=1
     q = complex parameter
     0<=z<2pi     independent variable (Vector or Matrix)


OUTPUTS:
```

```
    IP=S^{m}_p(z,q) ODD Ince Polynomial
    eta  = eigenvalue of the Ince Polynomial
    coef = coefficients of the Ince Polynomial
    dIP  = derivative of the Ince Polynomial

For more information about Ince Polynomial:

    Miguel A. Bandres and Julio C. Gutiérrez-Vega, "Ince-Gaussian
       modes of the paraxial wave equation and stable resonators"
    Journal of the Optical Society of America A, 21(5), 873-880
       (2004) ( http://goo.gl/rqq7nQ )

AUTHOR: Miguel A. Bandres
URL:    www.mabandres.com
%}

%% Check Input
if (m<1)||(m>p); error('ERROR: Wrong range for "m", 1<=m<=p');
   end;
if (-1)^(m-p)~=1;   error('ERROR: (p,m) must have the same parity,
    i.e., (-1)^(m-p)=1'); end;
[largo,ancho]=size(z); % change input to vector format
```

```
z=transpose(z(:));
normalization=1;

%% Calculate the Coefficients
if mod(p,2)==0
    %%%% p Even %%%%
    j=p/2;   N=j+1; n=m/2;

    % Matrix
    M=diag(q*(j+(2:N-1)),1)+diag(q*(j-(1:N-2)),-1) + diag(4*((0:N
        -2)+1).^2);

    % Eigenvalues and Eigenvectors
    [A,ets]=eig(M);
    ets=diag(ets);
    [ets,index]=sort(ets);
    A=A(:,index);

    % Normalization
    r=1:N-1;
    if normalization==0;
        N2=sum(A(:,n).^2);
```

```
        NS=sign(sum(r.*transpose(A(:,n))));
        A=A/sqrt(N2)*NS;
    else
        mv=(2:2:p).';
        N2=sqrt(sum((sqrt(gamma((p+mv)/2+1).*gamma((p-mv)/2+1)).*
            A(:,n)).^2));
        NS=sign(sum(r.*A(:,n)'));
        A=A/N2*NS;
    end

    % Ince Polynomial
    [R,X]=meshgrid(r,z);
    IP=sin(2*X.*R)*A(:,n);
    dIP=2*R.*cos(2*X.*R)*A(:,n);
    eta=ets(n);

else
    %%% p ODD %%%
    j=(p-1)/2; N=j+1; n=(m+1)/2;

    % Matrix
    M=diag(q/2*(p+(2*(0:N-2)+3)),1)+diag(q/2*(p-(2*(1:N-1)-1)),-1)
```

```
    + diag([-q/2-p*q/2+1,(2*(1:N-1)+1).^2]);

% Eigenvalues and Eigenvectors
[A,ets]=eig(M);
ets=diag(ets);
[ets,index]=sort(ets);
A=A(:,index);

% Normalization
r=2*(0:N-1)+1;
if normalization==0;
    N2=sum(A(:,n).^2);
    NS=sign(sum(r.*transpose(A(:,n))));
    A=A/sqrt(N2)*NS;
else
    mv=(1:2:p).';
    N2=sqrt(sum(  ( sqrt(gamma((p+mv)/2+1).*gamma((p-mv)/2+1) )
        .*A(:,n)).^2 ));
    NS=sign(sum(r.*A(:,n)'));
    A=A/N2*NS;
end
```

```
    % Ince Polynomial
    [R,X]=meshgrid(r,z);
    IP=sin(X.*R)*A(:,n);
    dIP=R.*cos(X.*R)*A(:,n);
    eta=ets(n);

end

coef=A(:,n);
IP=reshape(IP,[largo,ancho]);  % reshape output to original format
dIP=reshape(dIP,[largo,ancho]);

return

   10pt
% IG Plotting
tf = 0;  % Set initial while loop parameter tf
% while tf == 0;
%%%%%%%%%%%%    Input IGB order

% parity = input('parity?  (0 or 1)');
% p = input('order p?  (+integer)');
% m = input('m value?   (0<=m<=p)');
```

```
parity = 1;

p = 5;

m = 3;

% L = input('L scale');

% K = input('K size: Gaussian Factor');


%   Plotting in ellipticCoords

%f=5e-10;L = 5;

% for L =1:1:20;%original loop is 1:1:20

for L = 5

% L = 20;

 for ecc = 0.2:0.2:3.0;% 0.01% eccentricity

%       for ecc = 0.01;

f = 1*10^0;  N =511; w0=3*10^-1;%  3e-2 is default

[xi,eta,X,Y]=mesh_elliptic(f,L,N);        %  elliptic and gauss

   coords

[kxi,keta,kX,kY]=mesh_elliptic(f,L,N);  %  conjugate coords

R = sqrt(kX.^2 + kY.^2);  % radial coordinate


%%%%%%%%%Ince Gauss Beam


%[IGB,X,Y]=Ince_Gaussian(L,N,parity,p,m,e,w0,k,z)
```

```
%[IGB,X,Y]=Ince_Gaussian(60e-3,501,0,2,2,2,3e-3,(2*pi/632.8e-9),0)
    ;
  [IGB,X,Y]=Ince_Gaussian(L,N,parity,p,m,ecc,w0,(2*pi/632.8e-9),0);
%%%%%%%%%%%%%%%%%%%%%%%%    Example from Ince_Gaussian.m
%           figure;
%           surf(X,Y,abs(IGB)); shading interp; lighting phong; view
    (2);
%           axis tight; axis equal; xlabel('x','Fontsize',12);
%           ylabel('y','Fontsize',12);
%           title('Ince Gausssian Beam','Fontsize',12)
%           dx=abs(X(2,2)-X(2,1));
%           Normalization=sum(sum(IGB.*conj(IGB))).*dx^2;

%       Setting the filename according to orders p, m, and
    eccentricity, e
formatspec = 'P%dM%dE%.1fL%f';%numbering for related image files
    written
filenameparameters = sprintf(formatspec,p,m,ecc,L);
% nameparity = 'EVEN';
mkdir(filenameparameters);  %new directory made for each order

%                   IGB amplitude and phase
```

```
%%%%%%%%%%

filename = strcat(filenameparameters,...
    '\IGB',filenameparameters,'.bmp');  % filename
imwrite(abs(IGB),filename,'bmp'); %writing file to new directory


% figure();colormap gray;
% imageIGB = imagesc(angle(IGB));
% figure();colormap gray;
% image = imagesc(abs(IGB));
phase = angle(IGB);  % must change 511 ---> 512 x 512 matrix
Minphase = min(min(phase));
Maxphase =max(max(phase));
phase = (phase)./(max(max(phase)));  % normalize [0,1] for all
   elements
% phase = ((2/pi)-1).*phase;
%% Gaussian Modding
% if (X.^2 + Y.^2) >= 100
% phase = phase.*exp(-K*(X.^2+Y.^2));
% end
%  511 ---> 512 dim
% phase = phase + (-K*(X.^2+Y.^2));
```

```
phase = horzcat(zeros(511,1),phase);

phase = vertcat(zeros(1,512),phase);

% phase = 1-phase;



filename = strcat(filenameparameters,...

    '\IGBphase',filenameparameters,'.bmp'); % filename

imwrite(phase,filename,'bmp'); %writing file to new directory



IGBC = diff(diff(IGB,1,2),1,1); %X,Y order of diff(diff())

% IGBC = diff(diff(IGB,1,1),1,2); %Y,X order of diff(diff())

IGBC = abs(IGBC)./(max(max(abs(IGBC))));

% imshow(IGBC);

filename = strcat(filenameparameters,...

    '\IGBDiff',filenameparameters,'.bmp'); % filename

imwrite(IGBC,filename,'bmp'); %writing file to new directory



end

end
```

```
disp('Good bye! ');
```

Appendix B: SLM Specifications

The follow Table B displays Specifications for the BNS 512 Phase only SLM for models P512-0532 and P512-0635. More specific information may be obtained from BNS Non-linear systems.

Table B

Model	0532	0635
Array Size	7.68^2mm^2	7.68^2mm^2
0 order Diffraction Efficiency (Percent)	61.5	61.5
Format (Number of active pixels)	512^2	512^2
Mode	Reflective	Reflective
Pixel Size	$15^2\mu$m^2	$15^2\mu$m^2
Phase Pitch	2π	2π
Wavefront Distortion	$\lambda/3$@$532nm$	$\lambda/4$@$635nm$
LCD Response/Frequency	33.3ms/30Hz	33.3ms/30Hz